Cell

Article

TBL1XR1 Mutations Drive Extranodal Lymphoma by Inducing a Pro-tumorigenic Memory Fate

Graphical Abstract

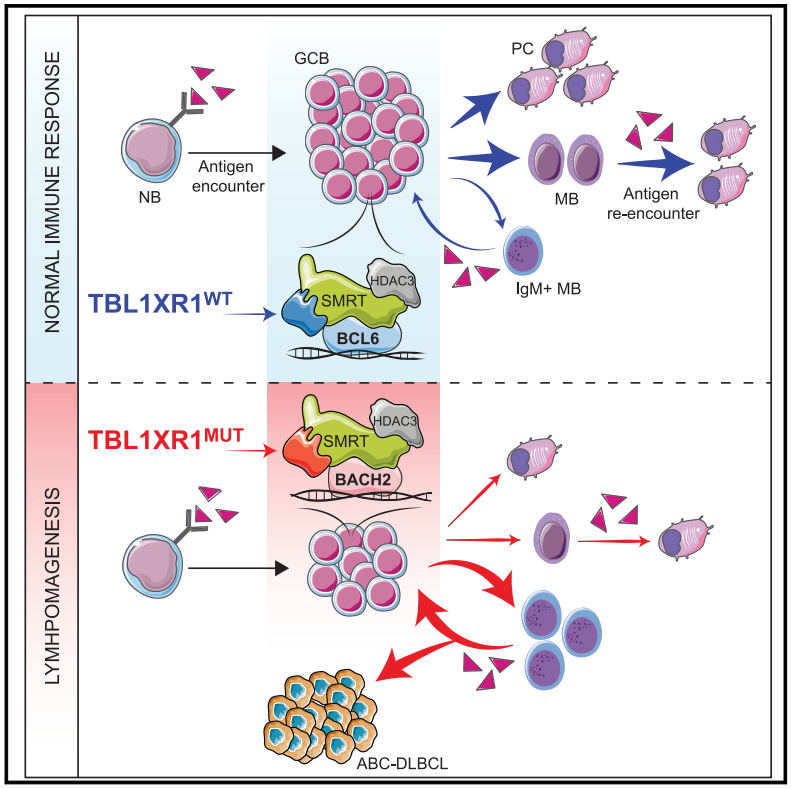

Highlights

- *TBL1XR1* mutation skews the humoral immune response toward producing memory B cells
- TBL1XR1 mutant memory cells feature aberrant cyclic reentry to new germinal centers
- Mutant TBL1XR1 acts by triggering aberrant targeting of SMRT complex to BACH2
- *TBL1XR1* mutation gives rise to extranodal ABC-DLBCLs derived from memory B cells

Authors

Leandro Venturutti, Matt Teater, Andrew Zhai, ..., David W. Scott, Gilbert G. Privé, Ari M. Melnick

Correspondence

amm2014@med.cornell.edu

In Brief

A subset of B cell lymphomas is driven by mutations that impair plasma cell differentiation and instead bias cell fate toward immature memory B cells, which preferentially re-enter germinal center reactions to drive lymphomagenesis.

Venturutti et al., 2020, Cell *182*, 1–20
July 23, 2020
https://doi.org/10.1016/j.cell.2020.05.049

CellPress

Please cite this article in press as: Venturutti et al., TBL1XR1 Mutations Drive Extranodal Lymphoma by Inducing a Pro-tumorigenic Memory Fate, Cell (2020), https://doi.org/10.1016/j.cell.2020.05.049

Cell

CellPress

Article

TBL1XR1 Mutations Drive Extranodal Lymphoma by Inducing a Pro-tumorigenic Memory Fate

Leandro Venturutti,[1] Matt Teater,[1] Andrew Zhai,[2] Amy Chadburn,[3] Leena Babiker,[1] Daleum Kim,[1] Wendy Béguelin,[1] Tak C. Lee,[1] Youngjun Kim,[4] Christopher R. Chin,[1,5] William T. Yewdell,[6] Brian Raught,[7] Jude M. Phillip,[1] Yanwen Jiang,[1] Louis M. Staudt,[8] Michael R. Green,[9,10] Jayanta Chaudhuri,[4,6,11] Olivier Elemento,[12] Pedro Farinha,[13] Andrew P. Weng,[14,15] Michael D. Nissen,[14] Christian Steidl,[13] Ryan D. Morin,[13] David W. Scott,[13] Gilbert G. Privé,[7,16] and Ari M. Melnick[1,17,*]

[1]Division of Hematology/Oncology, Department of Medicine, Weill Cornell Medicine, Cornell University, New York, NY 10021, USA
[2]Department of Biochemistry, University of Toronto, Toronto, ON M5S 1A8, Canada
[3]Department of Pathology and Laboratory Medicine, Weill Cornell Medicine, New York, NY 10065, USA
[4]Immunology and Microbial Pathogenesis Program, Weill Cornell Graduate School of Medical Sciences, New York, NY 10065, USA
[5]Tri-Institutional Program in Computational Biology and Medicine, New York, NY 10065, USA
[6]Immunology Program, Memorial Sloan Kettering Cancer Center, New York, NY 10065, USA
[7]Princess Margaret Cancer Centre, University of Toronto, Toronto, ON M5G 1L7, Canada
[8]Center for Cancer Genomics, National Cancer Institute, Bethesda, MD 20892, USA
[9]Department of Lymphoma and Myeloma, University of Texas MD Anderson Cancer Center, Houston, TX 77030, USA
[10]Department of Genomic Medicine, University of Texas MD Anderson Cancer Center, Houston, TX 77030, USA
[11]Gerstner Sloan Kettering Graduate School of Biomedical Sciences, New York, NY 10065, USA
[12]Caryl and Israel Englander Institute for Precision Medicine, Weill Cornell Medicine, New York, NY 10021, USA
[13]Centre for Lymphoid Cancer, BC Cancer Agency, Vancouver, BC V5Z1L3, Canada
[14]Terry Fox Laboratory, BC Cancer Agency, Vancouver, BC V5Z1L3, Canada
[15]Department of Pathology and Lab Medicine, BC Cancer Agency, Vancouver, BC V5Z1L3, Canada
[16]Department of Medical Biophysics, University of Toronto, and Princess Margaret Cancer Centre, Toronto, ON M5S 1A8, Canada
[17]Lead Contact
*Correspondence: amm2014@med.cornell.edu
https://doi.org/10.1016/j.cell.2020.05.049

SUMMARY

The most aggressive B cell lymphomas frequently manifest extranodal distribution and carry somatic mutations in the poorly characterized gene *TBL1XR1*. Here, we show that *TBL1XR1* mutations skew the humoral immune response toward generating abnormal immature memory B cells (MB), while impairing plasma cell differentiation. At the molecular level, TBL1XR1 mutants co-opt SMRT/HDAC3 repressor complexes toward binding the MB cell transcription factor (TF) BACH2 at the expense of the germinal center (GC) TF BCL6, leading to pre-memory transcriptional reprogramming and cell-fate bias. Upon antigen recall, TBL1XR1 mutant MB cells fail to differentiate into plasma cells and instead preferentially reenter new GC reactions, providing evidence for a cyclic reentry lymphomagenesis mechanism. Ultimately, *TBL1XR1* alterations lead to a striking extranodal immunoblastic lymphoma phenotype that mimics the human disease. Both human and murine lymphomas feature expanded MB-like cell populations, consistent with a MB-cell origin and delineating an unforeseen pathway for malignant transformation of the immune system.

INTRODUCTION

Diffuse large B cell lymphomas (DLBCLs) are the most common class of lymphomas (Beham-Schmid, 2017) and likely represent a heterogeneous group of diseases arising from different immune system processes. Gene expression profiling studies classified DLBCLs into two major subtypes: germinal center B cell (GCB) and activated B cell (ABC)-DLBCLs. GCB-DLBCLs reflect the transcriptional signature of B cells that are transiting through the germinal center (GC) reaction (Wright et al., 2003). GCs form transiently in response to T cell-dependent antigens and are composed of rapidly proliferating B cells that simultaneously undergo immunoglobulin somatic hypermutation (SHM). After transiting to a T cell-rich GC "light zone," GCB expressing the highest affinity immunoglobulins undergo plasma cell (PC) differentiation, while others transition to forming memory B cells (reviewed in Cyster and Allen, 2019). ABC-DLCBLs are described as manifesting a "post-GC" transcriptional signature, and evidence of chronic active B cell receptor (BCR) signaling and nuclear factor κB (NF-κB) activation is linked to somatic mutations in the BCR and toll-like receptor (TLR) signaling pathways (Phelan et al., 2018; Wright et al., 2003). However, the cell of origin (COO) and mechanisms of malignant transformation of ABC-DLBCLs remain poorly understood. From a clinical perspective,

Please cite this article in press as: Venturutti et al., TBL1XR1 Mutations Drive Extranodal Lymphoma by Inducing a Pro-tumorigenic Memory Fate, Cell (2020), https://doi.org/10.1016/j.cell.2020.05.049

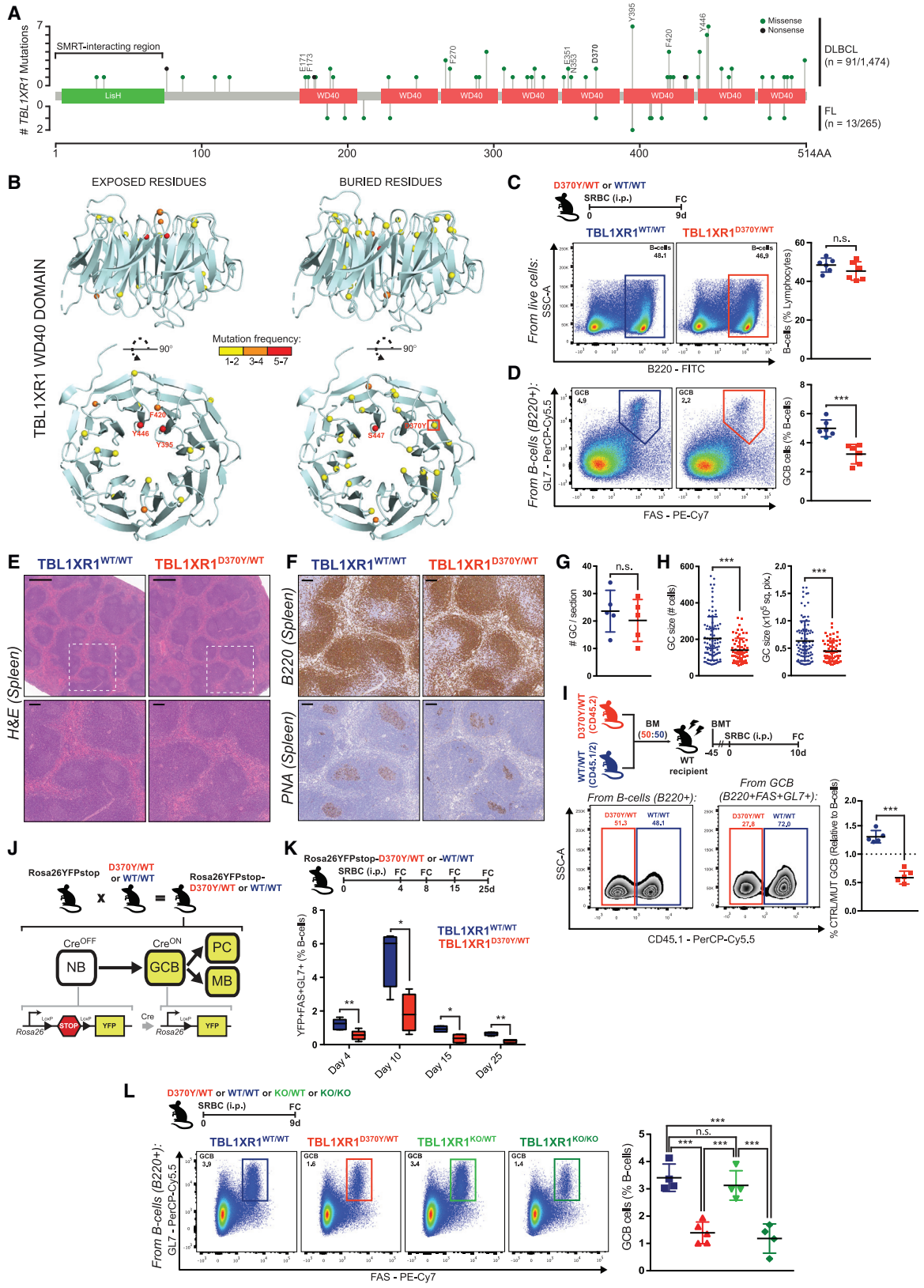

(legend on next page)

this is problematic, because these are among the most incurable and aggressive lymphomas (Beham-Schmid, 2017).

DLBCLs were more recently classified into putative distinct entities based on constellations of genetic lesions (Chapuy et al., 2018; Reddy et al., 2017; Schmitz et al., 2018). Two independent studies identified a novel genetically defined ABC-DLBCL subtype ("MCD" or "Cluster 5 [C5]" lymphomas) associated with unfavorable clinical outcomes, somatic activating mutations of *MYD88*, *CD79B*, and recurrent mutation of the poorly characterized gene *TBL1XR1* (Chapuy et al., 2018; Schmitz et al., 2018). *TBL1XR*1 mutations are likely founder events, based on variant allele frequency (Chapuy et al., 2018). From the clinical and biological perspective, a striking feature of these lymphomas is their unusual extranodal distribution (Chapuy et al., 2018; Schmitz et al., 2018), invading sites like the CNS and testes (Chapuy et al., 2016; Gonzalez-Aguilar et al., 2012). Neither GCB nor PC normally home to these tissues, raising questions about the pathogenesis and origin of these tumors within the complex milieu of the immune system.

Congenital missense mutations in *TBL1XR1* similar to those in lymphoma have also been linked to early-childhood developmental disorders, such as Pierpont syndrome (Heinen et al., 2016; Laskowski et al., 2016), suggestive of TBL1XR1's broad biological relevance. From the biochemical standpoint, TBL1XR1 is a core component of the SMRT/NCOR1 transcriptional repressor complexes (Yoon et al., 2003). These complexes also contain HDAC3, which enables the complex to repress transcription (Hatzi et al., 2013). Little is known about the exact role of TBL1XR1, which has been alternatively described as (1) enhancing the functionality (Tomita et al., 2004), or (2) driving the disassembly (Perissi et al., 2004) of these complexes. Whichever the case, it is notable that in GCB the majority of SMRT/NCOR1 complexes are bound and recruited by the transcriptional repressor BCL6 (Hatzi et al., 2013), which is essential for GC formation. Indeed, most recurrent mutations in DLBCL directly or indirectly enhance BCL6 functionality (reviewed in Hatzi and Melnick, 2014), a driving force on which most of these tumors rely for their survival (Cardenas et al., 2016; Cerchietti et al., 2010). *TBL1XR1* mutations are thus highly intriguing, given their potential to affect SMRT/NCOR1 complexes, as well as BCL6, and the complete lack of information on how this might play out from the molecular and biological perspectives. Herein, we explore the mechanism of action of *TBL1XR1* mutations, their impact on the humoral immune response, and whether they provide critical insight into the origin and immunological nature of aggressive extranodal MCD/C5 DLBCLs.

RESULTS

Tbl1xr1 Mutation Impairs Germinal Center Development

TBL1XR1 somatic mutations occur in ~5%–10% of DLBCL and follicular lymphoma (FL) cases, mainly as heterozygous missense alleles (Figure 1A). In line with recent studies (Chapuy et al., 2018; Schmitz et al., 2018), our analysis of three independent DLBCL cohorts confirmed that mutations occur more frequently in ABC-DLBCL (Table S1; Data S1A), are highly enriched in the MCD subtype (Data S1B), and often co-occur with *MYD88* mutations (Data S1C). *TBL1XR1* mutations largely occur within its WD40 domain (Figures 1A and 1B) and affect aromatic residues exposed on the same surface of the barrel structure (Figure 1B) that are predicted to mediate protein-protein interactions (PPI) (Wang et al., 2015).

Faced with the lack of a clear hotspot, we decided to model the D370Y allele in mice given it occurs both in lymphomas and congenital developmental disorders (Laskowski et al., 2016), suggestive of its biological relevance. The *Tbl1xr1* locus was engineered for conditional expression of D370Y (Figures S1A and S1B). Because $TBL1XR1^{MUT}$ lymphomas are derived from GC or post-GC B cells (Chapuy et al., 2018), we crossed $Tbl1xr1^{D370Y}$ mice to the *Cγ1Cre* strain (Casola et al., 2006) to restrict D370Y expression to (pre)GCB and GC-derived cells. Sorted GCB manifested the correct *Tbl1xr1* genotype (Figure S1C) and showed no difference in overall *Tbl1xr1* mRNA or protein abundance (Figures S1D and S1E).

Given a previous report suggesting that TBL1XR1 might limit SMRT functionality (Perissi et al., 2004), we hypothesized that $TBL1XR1^{MUT}$ would further enhance the activity of BCL6-SMRT complexes. We immunized $Tbl1xr1^{D370Y/WT}$ (D370Y/WT) or $Tbl1xr1^{WT/WT}$ (wild-type [WT]) mice with the T cell-dependent antigen sheep red blood cells (SRBC) and sacrificed them at the peak of the GC reaction. Unexpectedly, although B cell abundance remained unaltered in D370Y/WT mice (Figure 1C; Data S1D and S1E), these animals showed significant decrease in the absolute number (p value = 0.0008; Data S1E) and proportion

Figure 1. *Tbl1xr1* Mutation Impairs GC Development

(A) *TBL1XR1* mutations in DLBCL (Arthur et al., 2018; Ma et al., 2019; Reddy et al., 2017) and FL (Krysiak et al., 2017; Ma et al., 2019; Ortega-Molina et al., 2015). TBL1XR1-SMRT interacting region (Zhang et al., 2002) and PPI mutated positions are indicated. See also Data S1A–S1C and Table S1.

(B) Exposed (>25% accessible surface) or buried residues affected by missense DLBCL mutations in TBL1XR1 WD40 domain (4LG9; https://doi.org/10.2210/pdb4lg9/pdb).

(C and D) FC analysis of splenic (C) total B cells or (D) GCB. See also Data S1D–S1F.

(E) Spleen sections H&E from animals treated as in (C). Insets show zoom of outlined areas. Scale, 500 μm (top), 100 μm (bottom).

(F) B220 or PNA IHC in consecutive spleen sections from (E). Scale, 100 μm.

(G and H) Number of GC per spleen section (G) or GC size (H) as (left) number of cells or (right) area, based on PNA staining. Dots represent individual (G) animals or (H) GCs. Results for 5 animals per genotype.

(I) FC analysis of D370Y/WT and WT/WT relative contribution to total B cells and GCB, based on CD45 allelic frequencies. See also Data S1H–S1J.

(J) Use of the *Rosa26YFPstop* reporter.

(K) FC analysis of splenic GCB. Left to right: n = 4, 5, 5, 4 per genotype. See also Data S1K–S1L.

(L) FC analysis of splenic GCB.

Values represent mean ± SEM. Data reproducible with three repeats. NS, not significant; *$p < 0.05$; **$p < 0.01$; ***$p < 0.001$, using unpaired (C, D, and K) or paired (I) two-tailed Student's t test, or Mann-Whitney U-test (G and H) or one-way ANOVA with Tukey's post-test (L).

(p value = 0.0006; Figure 1D) of FAS$^+$GL7$^+$ GCB. Similar results were observed gating GCB as FAS$^+$CD38$^-$ (Data S1F). Animals showed no disruption of splenic architecture (Figure 1E). Immunohistochemistry (IHC) staining for B cells (B220) and GCB (peanut agglutinin, PNA) revealed normal follicular structures with smaller GCs in D370Y/WT mice, but conserved GC numbers per spleen (Figures 1F–1H). Dark zone (DZ) centroblasts (CB) and light zone (LZ) centrocytes (CC) ratios were similar to WT (Data S1G).

Although D370Y/WT GC were smaller, it is possible that these GCB could be fitter when in direct competition. We performed mixed chimera experiments where equal numbers of *Cd45.2;Tbl1xr1*$^{D370Y/WT}$ or *Cd45.1/2;Tbl1xr1*$^{WT/WT}$ bone marrow (BM) cells were transplanted into lethally irradiated syngeneic recipients. Following immunization, the relative proportions of *Cd45.1* and *Cd45.1/2* B220$^+$ cells were roughly equal, but D370Y/WT GCB manifested significant disadvantage compared to WT (Figure 1I), regardless of the initial ratio of transferred cells (Data S1H). Immunization with hapten-protein conjugates yielded similar results (Data S1I). Observations were also not dependent on the *Cd45* allelic variant, because identical results were obtained with *Cd45.1;Tbl1xr1*$^{D370Y/WT}$ (Data S1J).

To study the possibility of a premature/delayed GC burst as explanation for the reduced GC size, we crossed D370Y/WT mice to include a *Rosa26lox-stop-loxYFP* (*Rosa26YFP*) allele, which reports on Cre activity (Figure 1J; Data S1K). D370Y/WT mice presented reduced GCB abundance at all time points (Figure 1K; Data S1L), and GCs completely resolved by day 25. Collectively, these data indicate that *Tbl1xr1* mutation impairs, rather than enhances, the GC reaction (perhaps by hindering BCL6 function), while maintaining normal kinetics.

Tbl1xr1 Mutations Phenocopy TBL1XR1 Complete Loss

The absence of a clear hotspot suggests that *TBL1XR1* mutations behave as loss-of-function (LOF). Along these lines, focal *TBL1XR1* deletions are also detected in DLBCL patients (Data S1M) (Schmitz et al., 2018), albeit at lower frequency than missense mutations. We then generated a *Cγ1Cre*-inducible *Tbl1xr1* knockout (KO) mouse (Figures S1F–S1I) and again observed that although total B cell abundance was unchanged (Figures S1J and S1L), there was significant GCB reduction in immunized *Tbl1xr1*$^{KO/KO}$ (KO/KO) mice (Figures S1K and S1L; Data S1N). There was no disruption of splenic architecture or lymphoid follicles (Figure S1M), although there was significant reduction in GC size, but not GC number (Figures S1N–S1P). Mixed chimera experiments confirmed that KO/KO GCB are at disadvantage against WT (Figure S1Q). The kinetics of the GC reaction in KO/KO mice were similar to WT, but were again consistently hypoplastic (Figure S1R). Finally, KO/KO GCs showed normal ratios of LZ-DZ GCB (Data S1O).

The fact that KO/KO phenocopies D370Y/WT supports the idea that *Tbl1xr1* mutations confer LOF and suggests mutations may have a dominant negative (DN) character. Along these lines, GC formation appeared normal in heterozygous *Tbl1xr1*$^{KO/WT}$ mice (Figure 1L) and did not recapitulate the phenotype induced by D370Y/WT, which instead was virtually identical to KO/KO. This strongly suggests that *TBL1XR1* mutants function as DN LOF alleles.

Tbl1xr1 Mutation Impairs GC Proliferation

Apoptosis is prevalent in the GC, with up to half GCBs dying every 6 h (Mayer et al., 2017). D370Y/WT manifested similar frequency of apoptotic/dead cells to WT GCB, by AnnexinV/DAPI FC (Figure 2A; Data S1P) or TUNEL staining (Figure 2B). Similar findings were observed for KO/KO (Figure S2A). On the other hand, there was significant reduction in D370Y/WT GCB positive for the proliferation marker PCNA (Figure 2C). Abundance of T follicular helper cells (T_{FH}), which express CD40 ligand and induce GCB proliferation, was comparable in mutant and WT mice (Figure S2B). To assess for intrinsic defects in response to CD40 stimulation, we performed *ex vivo* activation of mixed D370Y/WT and WT naive B (NB) cells in organoid cultures (Béguelin et al., 2017) (Figure S2C). D370Y/WT and WT B cells acquired GC surface markers to approximately the same extent (Figure S2D), without significant differences in proliferation rate (Figure S2E). Hence, proliferation of D370Y/WT B cells is not impaired when given unrestricted CD40 stimulation.

To assess cell-cycle kinetics, we tested ethynyldeoxyuridine (EdU) incorporation in immunized D370Y/WT or WT mice. In line with PCNA staining, EdU$^+$ GCB were significantly depleted in D370Y/WT (Figure 2D), with a significant increase in GCB at the G0-1 stage, and reciprocal reduction in S and G2/M (Figure 2E). Similar results were observed for KO/KO (Figures S2F and S2G). As an orthogonal approach, D370Y/WT animals were crossed with *R26-Fucci2aR* reporter mice (Figure 2F; Data S1Q). In line with previous studies (Stewart et al., 2018), most CC in WT mice were at G0-1, and D370Y/WT had no significant impact on cell-cycle distribution (Figure 2G). As expected, WT CB showed high abundance of G2/M cells and fewer cells in G0-1 (Figure 2H). In contrast, D370Y/WT CB manifested significant reduction in the proportion of G2/M and late M cells, as well as increase in G0-1 (Figure 2H). BCL6 represses cell-cycle checkpoint genes in GCB (Hatzi and Melnick, 2014), but D370Y/WT or KO/KO CC showed no induction of these genes (Figure S2H), suggesting that proliferation effects are driven by a different mechanism. Impairment in proliferation largely explains the reduced abundance of GCB in *Tbl1xr1* mutant and KO/KO mice.

Tbl1xr1 Mutation Induces ABC-DLBCL-like Signatures Suggestive of Antagonism with BCL6

Although most DLBCL mutations engineered in mice induce GC hyperplasia (Béguelin et al., 2013; Dominguez et al., 2018; Hashwah et al., 2017; Hatzi et al., 2019), the *Tbl1xr1* phenotype was opposite and counter-intuitive as a lymphoma lesion. To gain mechanistic insight, we performed RNA sequencing (RNA-seq) in sorted D370Y/WT GCB. Unsupervised analysis revealed that D370Y/WT induces a distinct transcriptome (Figures S3A and S3B). Supervised analysis identified a D370Y/WT specific signature ($|\log_2 FC| > 1.5$; false discovery rate [FDR] <0.05), skewed toward gene de-repression (Figure 3A; Table S2). Pathway analysis revealed enrichment for ABC-DLBCL associated signatures (Figure 3B; Table S2), as well as pathways involved in chemotaxis, immune cytokine, and NF-κB signaling, all of which are repressed in GCB by BCL6-SMRT (Figure 3B). Accordingly, we observed significant enrichment for genes repressed through BCL6-SMRT enhancer binding, genes induced by BCL6 small

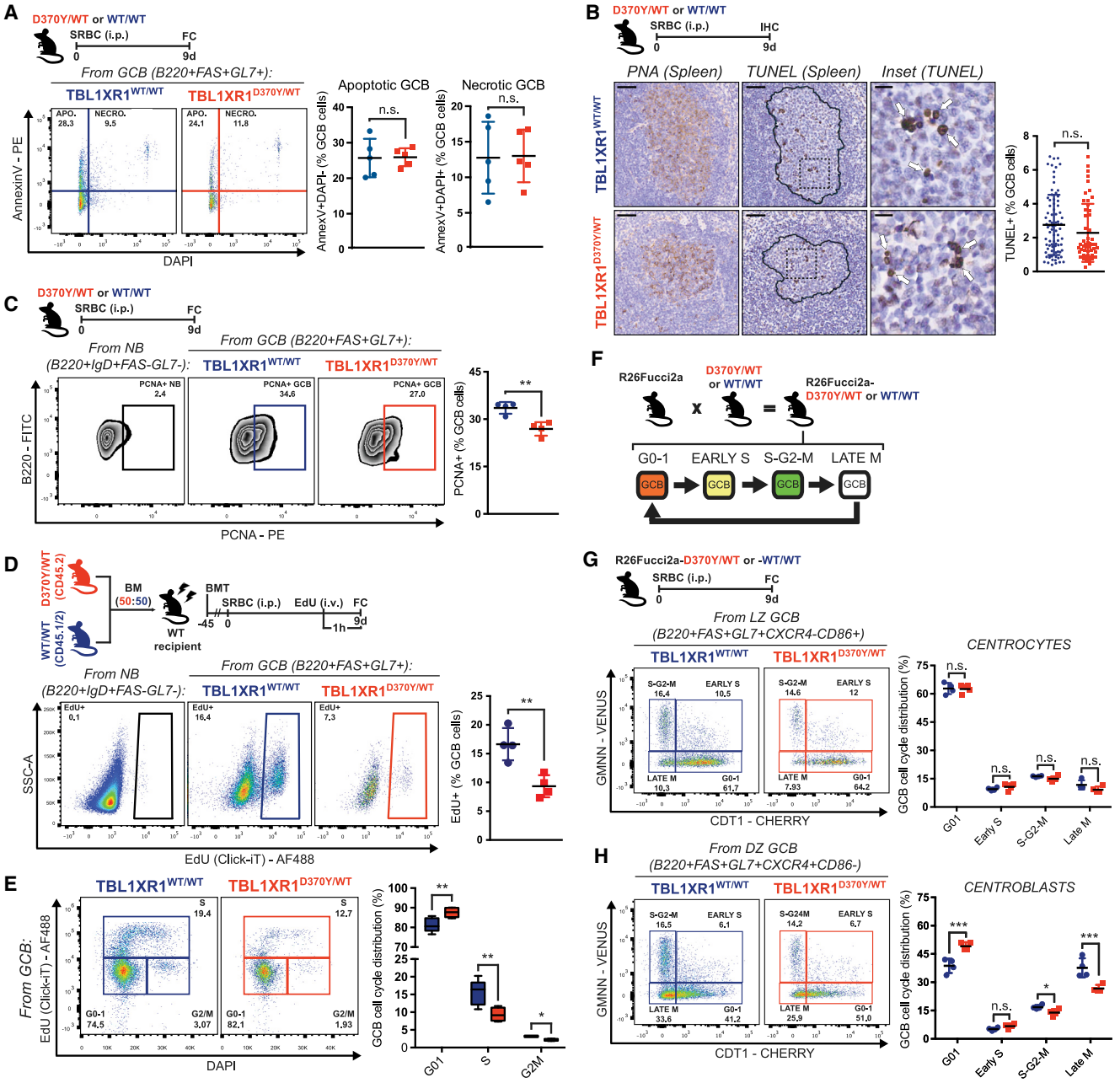

Figure 2. *Tbl1xr1* Mutation Impairs GCB Proliferation

(A) FC analysis of AnnexinV/DAPI staining of splenic GCB. See also Data S1P.

(B) IHC staining in consecutive spleen sections. Contour delineates GC area based on PNA stain. Insets show zoom of outlined areas. Arrows point representative TUNEL$^+$ GCB. Graph shows frequency of TUNEL$^+$ GCB per GC, where each dot is a GC. Results for 5 animals per genotype. Scale, 50 μm (left and center), 10 μm (right).

(C) FC analysis of splenic PCNA$^+$ GCB. NB from a WT mouse illustrates non-proliferating cells.

(D) FC analysis of EdU incorporation by splenic GCB. NB from a WT mouse illustrates non-proliferating cells.

(E) FC analysis of splenic GCB cell cycle in (D), based on EdU/DAPI staining. Data for n = 5 per genotype.

(F) Use of the *R26-Fucci2aR* reporter.

(G and H) FC analysis of cell-cycle distribution of (G) CC or (H) CB. See also Data S1Q.

Values represent mean ± SEM. Data reproducible with two repeats. p values calculated using unpaired (A, C, D, G, and H) or paired (D and E) two-tailed Student's t test, or Mann-Whitney U-test (B).

Please cite this article in press as: Venturutti et al., TBL1XR1 Mutations Drive Extranodal Lymphoma by Inducing a Pro-tumorigenic Memory Fate, Cell (2020), https://doi.org/10.1016/j.cell.2020.05.049

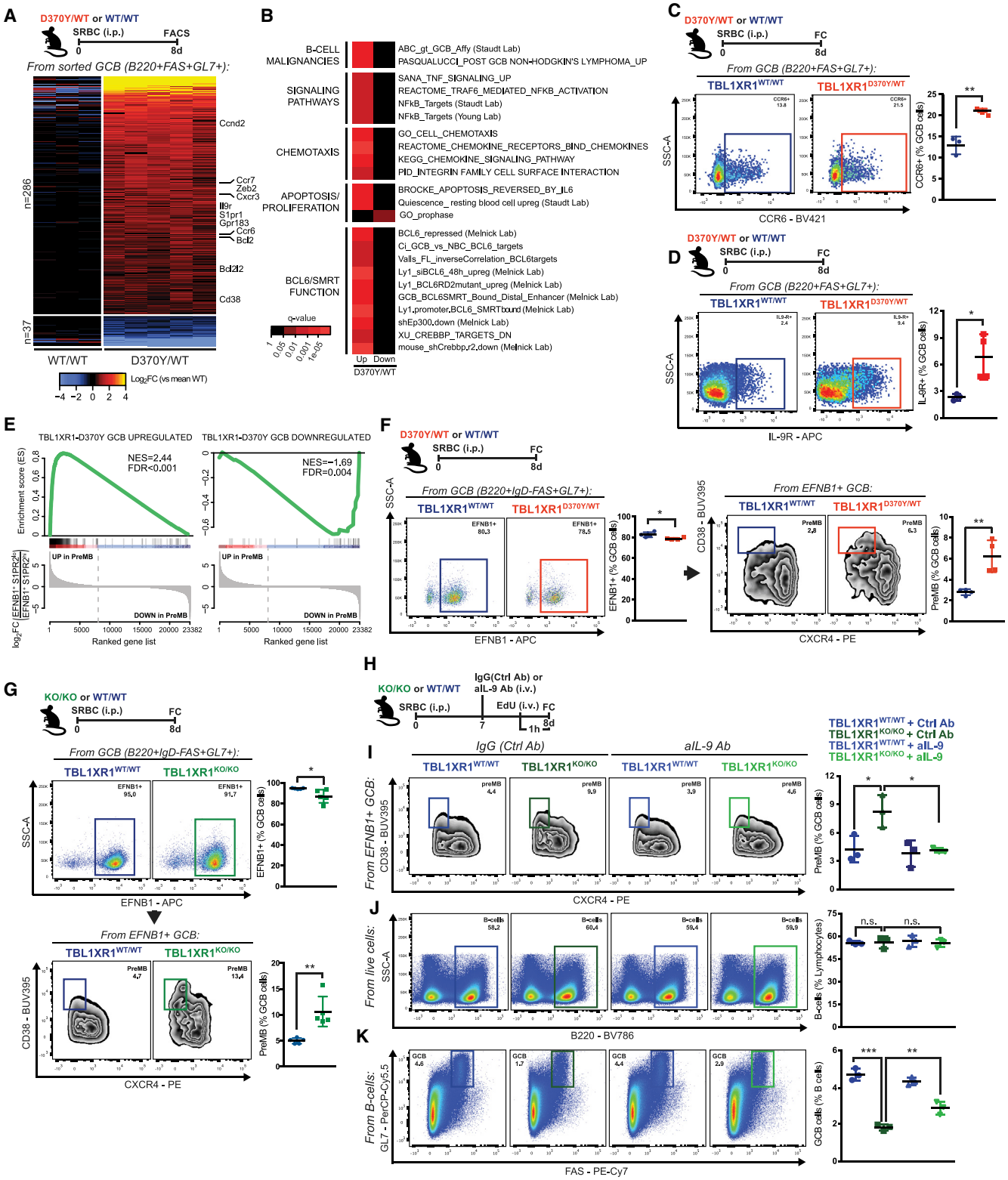

Figure 3. *Tbl1xr1* Mutation Induces PreMB Expansion

(A) Differentially expressed genes in splenic D370Y/WT GCB. Genes of interest are highlighted. See also Figures S3A–S3C and Table S2.

(B) Pathway enrichment for genes in (A). See also Table S2.

(C and D) FC analysis of (C) CCR6^{+} or (D) IL-9R^{+} splenic GCB.

(legend continued on next page)

interfering RNA (siRNA) and CREBBP target genes (CREBBP normally reverses BCL6-SMRT effects in the LZ) (Jiang et al., 2017) (Figure 3B). This suggests that TBL1XR1 plays a critical role in supporting the function of the BCL6-SMRT complex. Repression of EBI2 (*GPR183*) and S1PR1 by BCL6 is largely responsible for GCB confinement to lymphoid follicles (Arnon et al., 2013; Pereira et al., 2009), whereas they reactivate in cells exiting the GC. D370Y/WT GCB upregulated *Gpr183* and *S1pr1* (Figures 3A, S3C, and S3D), raising the possibility that TBL1XR1^{MUT} drive GCB to manifest post-GC phenotypes.

Tbl1xr1 Mutation Induces Expansion of the PreMB Compartment

D370Y/WT GCB showed upregulation of *Cd38* (Figures 3A and S3C), a gene that in mice is upregulated in MB, but not in PC (Oliver et al., 1997; Ridderstad and Tarlinton, 1998). Upregulation of CD38 is also a feature of precursor MBs (preMB) in the GC (Laidlaw et al., 2017). PreMB were alternatively defined as LZ GCB with augmented expression of CCR6 (Suan et al., 2017), a receptor upregulated in D370Y/WT and KO/KO GCB (Figures 3A, 3C, S3C, and S3E). A third study defined preMB as cell-cycle arrested interleukin (IL)-9R$^+$ GCB (Wang et al., 2017b), traits present in D370Y/WT and KO/KO mice (Figures 3A, 3D, S2G, S3C, and S3F). Accordingly, we observed enrichment of the D370Y/WT signature among transcriptional profiles of preMB cells in these reports (Figures 3E, S3G, and S3H).

Immunophenotypic analysis of D370Y/WT GCs revealed marked and significant increase in preMB at all studied time points (p value = 0.0045) (Figures 3F and S3I), and also with independent antigens (Figure S3J). PreMB expansion was also seen for KO/KO (Figure 3G; Data S1R), but not for *Tbl1xr1*$^{KO/WT}$ (Data S1S), supporting that *TBL1XR1* mutations act as DN LOF. Given that D370Y/WT and KO/KO GCB showed significant *Il9r* upregulation, which plays a role in MB formation (Wang et al., 2017b), we tested whether IL-9 blockade would rescue the observed phenotype (Figure 3H). Strikingly, blockade of IL-9R function reverted the KO/KO-driven preMB expansion (Figure 3I). Although total B cells were not affected by IL-9 blockage (Figure 3J), there was partial rescue of GC impairment in KO/KO mice (Figure 3K), concomitant with increased GCB proliferation (Data S1T). Hence, preMB expansion downstream of TBL1XR1 deficiency remains dependent on key MB signaling pathways.

Tbl1xr1 Deficiency Biases GC Fate toward MB Cells and away from the PC Lineage

We next explored whether preMB expansion translated into bias toward MB. D370Y/WT GCB transcriptome showed strong enrichment for MB gene signatures, but no enrichment for PC genes (Figures 4A and 4B) (Luckey et al., 2006). In agreement, GCB expression of the master PC TF BLIMP1 was not affected by *Tbl1x1* mutation or loss (Figures S4A and S4B). To confirm these findings, we used a mixed chimera approach with *Rosa26YFP;Tbl1xr1*$^{D370Y/WT}$ versus *Rosa26YFP;Tbl1xr1*$^{WT/WT}$ cells to track GC and post-GC cells (Figure 4C; additional mice were administered CD40-blocking antibodies). D370Y/WT splenocytes revealed a lower percentage of YFP$^+$ cells (Figure 4D). As expected, most YFP$^+$ cells corresponded to GCB (B220$^+$CD138$^-$GL7$^+$FAS$^+$), which were reduced in the D370Y/WT compartment (Figures 4E and S4C; Data S1U). On the other hand, D370Y/WT cells showed significant increase in MB (B220$^+$CD138$^-$FAS$^{-/lo}$GL7$^-$CD38$^+$IgD$^-$), and a concomitant reduction in plasmablasts (PB) (B220$^+$CD138$^+$) and PC (B220$^-$CD138$^+$) (Figures 4E and S4C). Experiments with *Rosa26YFP;Tbl1xr1*$^{KO/KO}$ mice yielded the same phenotype (Figures S4D and S4E).

GCB with intermediate affinity BCRs tend to become MB cells after T cell help, whereas high-affinity GCBs receive strong T cell help, causing GCBs to differentiate into PCs or recycle to the DZ (Shinnakasu et al., 2016). CD40-blocking antibodies in mixed chimeras (Figure 4C) led to profound reduction in GCBs, as expected (Baumjohann et al., 2013), to the point where differences in YFP$^+$ cell abundance among D370Y/WT and WT were lost (Figures 4F and 4G). Reduction of CD40 input drove the majority of the remaining D370Y/WT GC-derived B cells to the MB compartment. In contrast, the majority of residual WT cells were IgD$^+$ activated B cells ("aB") that presumably had not yet entered the GC reaction. No PCs were identified in this setting from D370Y/WT, suggesting that the MB cell fate is hardwired into the mutant B cells (Figure 4G).

Because PC formation is a rather late event in the GC (Weisel et al., 2016), we evaluated whether commitment bias was also detectable at later time points. To this end, used an adoptive transfer system to quantify antigen-specific MB and PC 24 days after immunization (Figure 4H; Data S1V). Assessment of NP-specific populations again showed that D370Y/WT biased cell fate toward MB, at the expense of PC (Figure 4H). Finally, assessment of long-lived PC (LLPC) in the BM, 70 days after immunization of *Rosa26YFP;Tbl1xr1*$^{D370Y/WT}$ mice, revealed that although the abundance of total LLPC was unaltered, D370Y/WT had less GC-derived LLPC than WT mice (Figure 4I).

TBL1XR1 Mutations Cause a BCL6-to-BACH2 Molecular Switch

TBL1XR1 is a core component of the SMRT/NCOR1 complex, which in GCB is recruited to chromatin by BCL6 (Hatzi et al., 2013). We found that TBL1XR1 is also present in chromatin-bound BCL6 complexes, by RIME- liquid chromatography-tandem mass spectrometry (LC-MS/MS) (Figure S5A; Table S3).

(E) GSEA of D370Y/WT GCB against preMB (EFNB1$^+$S1PR2^{lo}) GCB (GSE89897). See also Figures S3G and S3H.
(F and G) FC analysis of EFNB1$^+$ and preMB populations in splenic GCB in (F) D370Y/WT.or (G) KO/KO mice, as compared to WT/WT controls. See also Figures S3I–S3K and Data S1R.
(H) Experimental scheme and timeline for (I)–(K).
(I) FC analysis of preMB in splenic GCB.
(J and K) FC analysis of splenic (J) total B cells or (K) GCB.
Values represent mean ± SEM. Data reproducible with two repeats. P values calculated using unpaired two-tailed Student's t test (C, D, F, and G), or one-way ANOVA with Tukey's post-test (I)–(K).

Please cite this article in press as: Venturutti et al., TBL1XR1 Mutations Drive Extranodal Lymphoma by Inducing a Pro-tumorigenic Memory Fate, Cell (2020), https://doi.org/10.1016/j.cell.2020.05.049

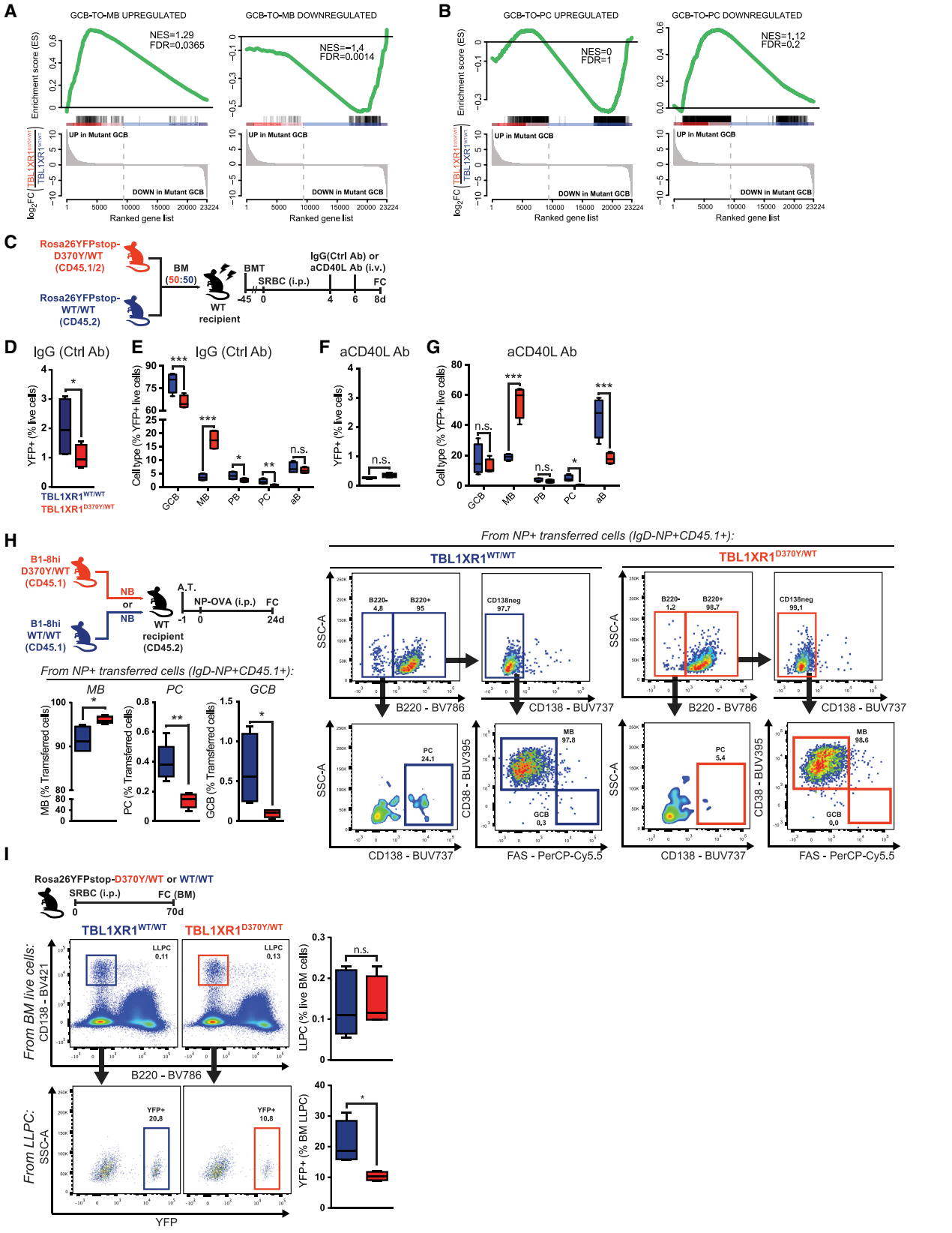

(legend on next page)

Interaction of endogenous TBL1XR1 with the SMRT/HDAC3 complex and BCL6 was confirmed by coimmunoprecipitation (coIP) (Figure S5B). In other systems, TBL1XR1 can have SMRT-independent functions (Li and Wang, 2008). We therefore performed proximity ligation-mass spectrometry (BioID) for TBL1XR1^{WT} interacting partners in GC-derived cell lines (Figure S5C). The majority of significantly interacting proteins for TBL1XR1^{WT} were restricted to components of the SMRT complex (Figure 5A; Table S3). In addition to these, only BCL6 and another BTB-domain containing TF (BACH2), appeared as significant hits (Figure 5A), largely ruling out alternative functions for TBL1XR1^{WT} in GC-derived B cells.

To assess whether *TBL1XR1* mutations alter its interactome, we conducted additional assays modeling one of the most recurrent DLBCL mutations (TBL1XR1^{Y446S}) (Figure 1A). Surprisingly, although the interaction with SMRT/HDAC3 complex was preserved, the only significant change in the TBL1XR1^{MUT} interactome was ~6-fold gain of interaction with BACH2, at the expense of BCL6 (Figure 5B). Similar results were obtained in an ABC-DLBCL cell line (Figures 5C and S5C; Table S3) and in HEK293 cells (not shown). Assessment of three independent TBL1XR1 mutants by coIP confirmed gain of interaction with BACH2 (Figure 5D) and loss of interaction with BCL6 (Figure S5D) without alteration of total protein levels (Figures S5D and S5E).

In accordance with these data, genes de-repressed in D370Y/WT GCB *in vivo*, matched those repressed by BCL6 (Figure 5E). Because *Tbl1xr1* mutation did not affect BCL6 expression levels (Figure S5F), this suggested interference at the functional level. To test this, we crossed D370Y/WT mice to the *IμBcl6* strain, which constitutively expresses BCL6 in GCB and manifests GC hyperplasia (Cattoretti et al., 2005). Indeed, *IμBcl6* mice manifested GC hyperplasia after immunization (Figures 5F and 5G; Data S1W), which, in the presence of the *Tbl1xr1*^{D370Y}, was rescued back to the levels of the WT control (Figures 5F and 5G). As reported above in a WT background, *IμBcl6-Tbl1xr1*$^{D370Y/WT}$ GCB manifested a preMB-like transcriptome (Table S4; Data S1X) and actual preMB expansion (Data S1Y). In agreement with our biochemical data, we observed enrichment for a BACH2-driven signature in *IμBcl6-Tbl1xr1*$^{D370Y/WT}$ GCB (Figure 5H) and significant depletion of the BCL6 program (Figure 5I). BACH2 is reported to be a key TF in MB formation (Shinnakasu et al., 2016), and our data suggest that TBL1XR1 mutations mistarget the SMRT complex to BACH2, thus inducing preferential transcriptional rewiring toward MB, while preventing PC formation by maintaining BACH2 repression of BLIMP1 (Data S1Z) (Huang et al., 2014; Ochiai et al., 2006).

Transcriptional profiling of KO/KO GCB likewise enriched both preMB and *IμBcl6-Tbl1xr1*$^{D370Y/WT}$ signatures (Figures S5G and S5H; Table S4). More importantly, it recapitulated the upregulation of BCL6 targets (Figure 5J), and engagement of BACH2-driven program (Figure 5K). KO/KO did not affect BCL6 expression in GCB (Figure S5I) but was able to rescue BCL6-induced hyperplasia in *IμBcl6* GCs (Figure 5L). To assess SMRT/HDAC3 shuttling at the biochemical level, we developed TBL1XR1-KO variants of a GC-derived lymphoma cell line using CRISPR.Cas9 (Figure S5J). Similar to primary GCB, these clones showed impaired proliferation (Figure S5K). Notably, TBLXR1-KO resulted in loss of BCL6-SMRT/HDAC3 interaction and gain in BACH2-SMRT/HDAC3 Co-IP (Figure S5L). TBL1XR1 is thus critical for the preferential association of SMRT with BCL6 in GCBs, and its LOF induces preferential interaction with BACH2 (Data S1AA), thus explaining the GC impairment and MB cell fate bias.

Tbl1xr1 Mutant MB Cells Manifest Traits Associated with Preferential Reentry to the GC Reaction

MB reentry into the GC has been proposed as a putative mechanism of GC-derived lymphomagenesis (Sungalee et al., 2014). Given our findings, we postulated that *Tbl1xr1* mutation might generate aberrant MBs with capacity for preferential reentry into new GCs. To explore whether D370Y/WT MBs persisted over time, we immunized mice with NP-CGG and sacrificed long after GC resolution, which revealed long-lasting expansion of NP-specific MB in spleen and BM (Figures 6A and 6B; Data S1BB–S1CC). A subset of non-class switched MB cells in humans is proposed to re-seed GCs upon recall, while switched MB differentiate into Ig-secreting cells (Dogan et al., 2009). D370Y/WT and KO/KO GCB showed significant restriction in class-switch recombination (CSR), with a relative increase in IgM$^+$ and reduction in IgG1$^+$ cells (Figures 6C and S6A). This was not due to delayed kinetics, because later time points showed similar isotype representation (Figure S6B), nor was it due to an impairment in *Aicda* induction (Figures S6C–S6E). The CSR restriction was also evident in GC-derived MB, tracked with the *Rosa26YFP* reporter (Figures 6D and S6F; Data S1EE). In accordance with surface Ig profiles, NP-OVA immunized D370Y/WT and KO/KO mice showed impaired IgG1 antibody responses (Figures S6G and S6H). Still, affinity maturation was not significantly affected (Figures S6I and S6J), nor were there differences in Ig SHM burden between D370Y/WT and WT GCB (Figure S6K), further suggesting that AID activity was not compromised.

In mice, CD80$^-$PDL2$^-$ MBs, which are mostly IgM$^+$, show a higher capacity for GC reentry, while CD80$^+$PDL2$^+$ MB are generally class-switched, and tend to differentiate into PC (Zuccarino-Catania et al., 2014). Profiling of donor-derived antigen-

Figure 4. *Tbl1xr1* Mutations Bias Cell Fate toward MB Cells

(A and B) GSEA of antigen-specific (A) MB or (B) PC, relative to GCB (GSE4142), against D370Y/WT GCB.

(C) Experimental scheme and timeline for (D)–(G).

(D and E) FC analysis of (D) total YFP$^+$ splenocytes in IgG(Ctrl Ab)-treated mice, and (E) the relative cell type composition of this population. Results for 4 animals. See also Figure S4C and Data S1U.

(F and G) FC analysis of (F) total YFP$^+$ splenocytes in anti-CD40L-treated mice, and (G) the relative cell type composition of this population. Results for 4 animals.

(H) FC analysis of cell type composition of antigen-specific splenocytes. Results for 5 animals. See also Data S1V.

(I) FC analysis of (top) total or (bottom) GC-derived BM LLPC.

Values represent mean ± SEM. Data reproducible with two repeats. p values calculated using unpaired (H and I) or paired (D)–(G) two-tailed Student's t test.

Please cite this article in press as: Venturutti et al., TBL1XR1 Mutations Drive Extranodal Lymphoma by Inducing a Pro-tumorigenic Memory Fate, Cell (2020), https://doi.org/10.1016/j.cell.2020.05.049

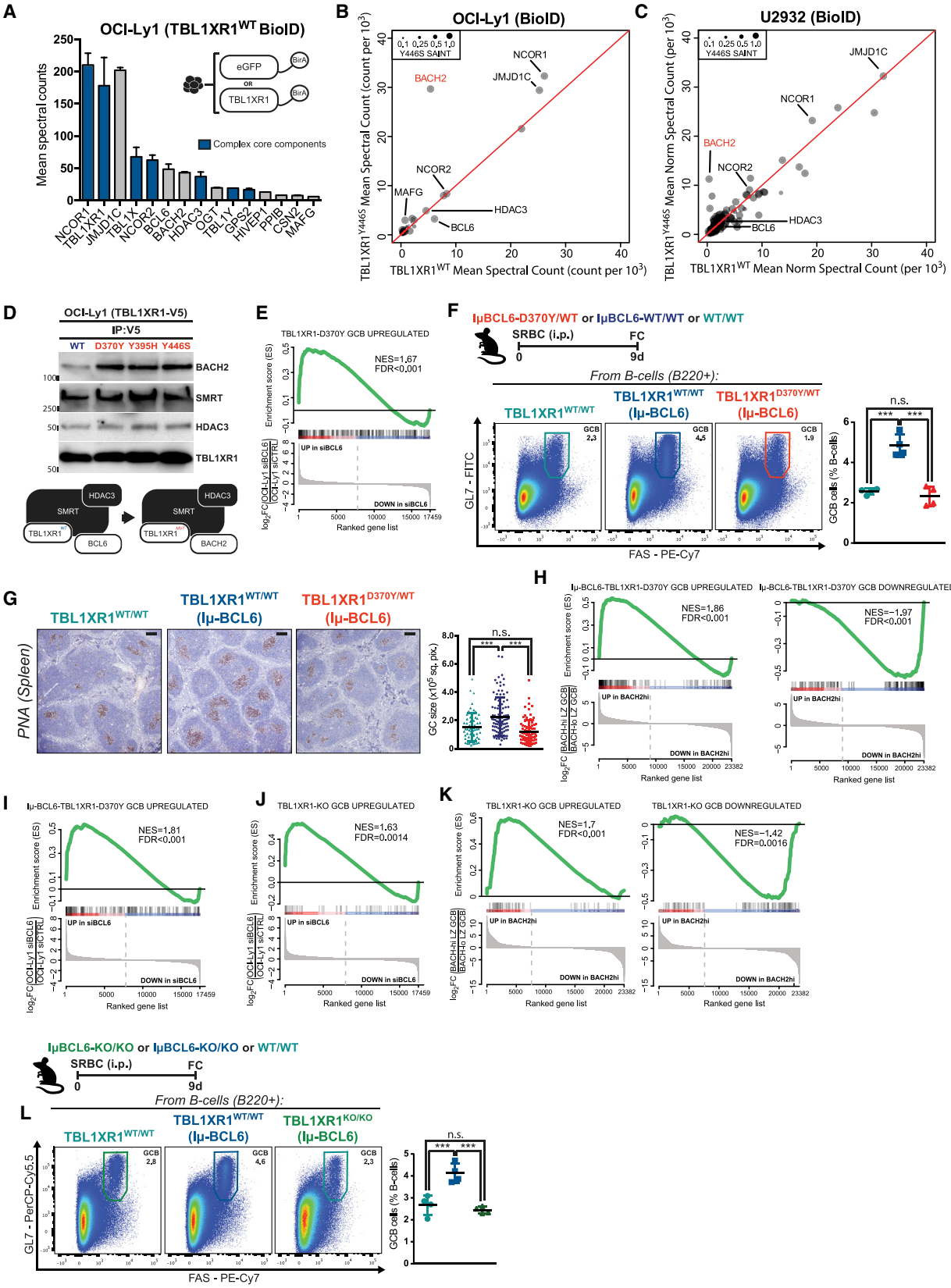

(legend on next page)

specific MB cells (CD45.1$^+$CD138$^-$B220$^+$IgD$^-$NP$^+$) from an adoptive transfer system revealed that D370Y/WT MB were significantly over-represented in the CD80$^-$PDL2$^-$ population (Figure 6E). Most D370Y/WT MB were also IgM$^+$, further confirming a CSR restriction (Figure S6L).

Tbl1xr1 Mutant MB Cells Preferentially Become GCB-Cells upon Antigen Recall

Results above suggest that TBL1XR1^{MUT} might predispose MB for GC reentry upon recall. To test this, we conducted secondary adoptive transfer experiments (Figure 6F), where sorted D370Y/WT or WT antigen-specific MB were transferred in equal numbers into μMT recipient mice, along with OT-II memory T cells to boost MB recall (Zuccarino-Catania et al., 2014). μMT mice lack mature B cells and antigen-specific antibodies (Kitamura et al., 1991), allowing specific detection of those coming from transferred cells. Recall was assessed 3.5 days after immunization of recipients, to exclude confounding factors such as differences in GC expansion that might occur later on. D370Y/WT transferred cells (NP$^+$CD45.1$^+$) (Figure S6M) persisted largely as B220$^+$ (Figure 6G) and over 70% of these were FAS$^+$GL7$^+$ (Figure 6H). The relative total abundance of GCB was almost 2-fold higher in animals transferred with mutant MB than those receiving WT MB (Figure 6H), indicating that D370Y/WT favors MB reentry into new GC reactions. In contrast, ~50% of the WT cells downregulated B220 (Figure 6G), consistent with PC differentiation, as evidenced by CD138 upregulation in some of these (Figure 6I). Terminal differentiation of D370Y/WT MB into PC was practically null at the assessed time point (Figure 6I). In agreement, only WT MB led to a detectable secretory recall response in the form of high-affinity IgG1/Lambda Ig (Figure 6J). These data suggest that TBL1XR1^{MUT} causes aberrant expansion of persisting MB and provides the first evidence that a lymphoma mutation can drive preferential reentry of putative clonal precursor cells into subsequent immune reactions.

Tbl1xr1 Alterations Lead to Extranodal Immunoblastic-like Lymphomas

Because TBL1XR1-driven transformation may require GC reentry over an extended period of time, incompatible with mice lifespan (Sungalee et al., 2014), we used *CD19cre* to increase the frequency of mature B cells carrying *Tbl1xr1* alterations. This did not affect B cell development (Data S1EE–S1GG) and recapitulated the *Cγ1Cre* phenotype (Figures S7A–S7D). Because C5/MCD carry near-uniform *18q* gain and high BCL2 levels (Chapuy et al., 2018; Wright et al., 2020), we further crossed our animals with *VavP-Bcl2* mice (Ogilvy et al., 1999) to phenocopy this effect. We generated cohorts of *VavP-Bcl2;CD19Cre;Tbl1xr1$^{KO/KO}$* and *VavP-Bcl2;CD19Cre;Tbl1xr1$^{WT/WT}$* mice and immunized them periodically to make sure they generated GCs (Figure 7A). Mice were sacrificed at a time point when *VavP-Bcl2* animals show pre-tumoral lymphoproliferation (Egle et al., 2004). Although all KO/KO animals had developed macroscopic tumors at necropsy, most with extranodal localization such as kidney, lung, liver, and intestines (Figure 7B), no masses were found in controls. Splenic hyperplasia was evident in all animals but was exacerbated in KO/KO (Figure 7C). Splenocytes in the control group had the expected representation of T cells (CD3$^+$) and B cells (B220$^+$) (Figure 7D) but a massive over-representation of GCB (Figure 7E). In contrast, KO/KO manifested an expansion of B220$^-$ cells (Figure 7D). The few remaining B220$^+$ KO/KO cells lacked GCB markers for the most part but showed relative expansion of (pre)MB populations (Figures 7F and 7G; Data S1HH–S1II). B220$^-$ KO/KO cells, in turn, expressed higher, albeit variable, levels of CD138 than the controls (Figure 7H). Both groups showed comparable levels of mature B cells in their BM, suggesting the phenotype was not linked to an early-stage developmental impairment (Data S1JJ–S1KK).

Histological analysis of lymphoid and other tissues in KO/KO mice revealed predominantly large and highly atypical immunoblasts, often with large and irregularly shaped nuclei and a moderate amount of cytoplasm, mimicking the appearance of human extranodal ABC-DLBCLs (Figure S7E). In the spleen, these cells were seen predominantly outside the follicles in the red pulp, disrupting the splenic architecture (Figure 7I). These cells also extensively infiltrated and distorted many tissues including liver (Figure 7J) and kidneys (Figure 7K). Consistent with this extranodal scenario, lymph nodes (LN) were only focally involved. Immunoblastic cells in KO/KO specimens were virtually all Ki67$^+$ and many stained for CD138 (Figures S7F and S7G), consistent with the notion that TBL1XR1 loss results in a post-GC lymphoma phenotype. In comparison, the overall architecture of the liver, spleen, kidneys, and lung was relatively intact for *Tbl1xr1$^{WT/WT}$* (Figures 7I–7K), although LNs showed variable sinusoidal expansion by smaller infiltrating lymphocytes. Analysis of tissues yielded sporadic, small, focal lymphocytic infiltrates linked to blood vessels (Figures 7J and 7K) in the LN, spleen,

Figure 5. *TBL1XR1* Mutations Introduce a BCL6-to-BACH2 Switch

(A) TBL1XR1^{WT} interacting proteins. Shown are hits with SAINT >0.75 and 2-fold spectral counts (averaged between biological duplicates) over eGFP-BirA. See also Figure S5C and Table S3.

(B and C) Comparison between TBL1XR1 WT and Y446S BioID in (B) OCI-Ly1 or (C) U2932 cells. Results as average of biological duplicates for each condition.

(D) CoIP results for V5 pulldown in cells inducibly expressing WT or mutant TBL1XR1-V5 fusion proteins. See also Figures S5D and S5E.

(E) GSEA of D370Y/WT GCB against siBCL6-treated OCI-Ly1 (GSE29282).

(F) FC analysis of splenic GCB. See also Data S1W.

(G) IHC staining of spleen sections from (F). Graph shows GC area based on PNA staining. Dots are individual GCs. Results for 4 animals per genotype. Scale, 100 μm.

(H and I) GSEA of *IμBcl6-Tbl1xr1$^{D370Y/WT}$* GCB against (H) BACH2^{hi} GCB (GSE77319) or (I) siBCL6-treated OCI-Ly1.

(J and K) GSEA of KO/KO GCB against (J) siBCL6-treated OCI-Ly1 or (K) BACH2^{hi} GCB.

(L) FC analysis of splenic GCB.

Values represent mean ± SEM. Data reproducible with two repeats. p values calculated using one-way ANOVA with Tukey's post-test (F and L), or Kruskal-Wallis H test with Dunn's post-test (G).

Please cite this article in press as: Venturutti et al., TBL1XR1 Mutations Drive Extranodal Lymphoma by Inducing a Pro-tumorigenic Memory Fate, Cell (2020), https://doi.org/10.1016/j.cell.2020.05.049

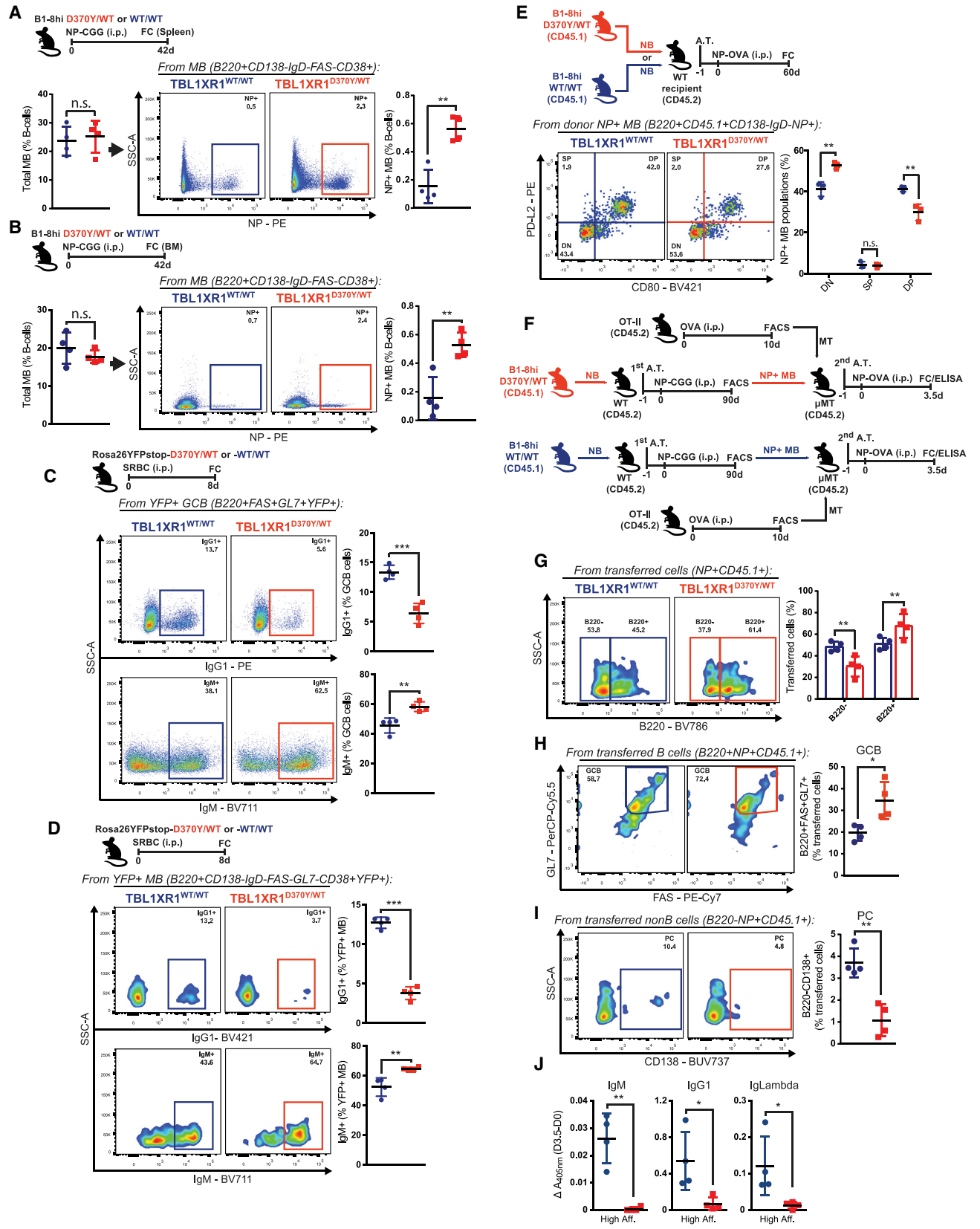

(legend on next page)

and BM that rarely affected tissue architecture (Figure 7I and not shown). IHC revealed infiltrates were composed of T and B cells, as well as PC (Figures S7F and S7G). Ki67 stain was low for small plasmacytoid cells/plasma cells and lymphoid cells and higher in the few larger cells (Figures S7F and S7G). To assess whether the disease translated into accelerated lethality, we conducted a survival study in an additional cohort of mice, immunized to induce GC formation (Figure 7L). The study revealed that KO/KO mice died of their disease significantly sooner than WT (Figure 7M).

Human C5/MCD DLBCLs show the highest AID footprint (Chapuy et al., 2018), suggesting they originate from GC-transitioned cells. We examined Ig SHM in our KO/KO mouse lymphomas, to exclude that these derived from extrafollicular responses. Sequencing of intron J_H4 revealed significant SHM burden in tumors that was absent in *Acida*$^{KO/KO}$ GCB used as controls (Figure 7N). We then performed targeted sequencing of a region in the *Pim1* locus frequently impacted by off-target AID activity (Liu et al., 2008), because *PIM1* mutations are a hallmark of C5/MCD tumors and frequently co-occur with *TBL1XR1* mutations (Data S1C). Notably, KO/KO tumors accumulated more mutations than *VavP-Bcl2* controls (Figure 7O). Strikingly, the highest rate of off-target mutations was detected in extranodal tumors from KO/KO mice (Figure 7O). To further confirm that these lymphomas could arise from GCB, we generated *Cγ1Cre; VavP-Bcl2;Tbl1xr1*$^{KO/KO}$ mice. These mice again showed extensive extranodal infiltrates, composed of a heterogeneous mixture of lymphocytic and immunoblastic populations (Figure S7H), with a higher percentage of B220$^+$ cells than the *CD19Cre* variant (Figure S7I). Hence, the more homogeneous plasmacytic-like presentation in *CD19Cre* mice is not required for transformation or extranodal dissemination of malignant B cells but might instead represent a later or alternative stage in disease progression. These data are consistent with TBL1XR1 driving MCD/C5 pathogenesis by inducing MB cell reentry into successive GC reactions.

Human MCD/C5 Tumors Show Evidence of MB Origin

If MB served as COO for C5/MCD lymphomas, we would expect to find phenotypic evidence in clinical specimens. In humans, CD38 is expressed in GCB and PC, but lost in MB (Arpin et al., 1995). Performing IHC in a DLBCL patient's cohort (Arthur et al., 2018), we observed that although ~40% of all *TBL1XR1*^{WT} DLBCLs were CD38$^+$, only ~10% of *TBL1XR1*^{MUT} cases were CD38$^+$ ($p = 0.03$) (Figure S7J). We further subclassified (Wright et al., 2020) tumors in this cohort and observed significant and striking differences between MCD cases (0% CD38$^+$) and non-MCD ABC-DLBCL cases (~30% CD38$^+$) ($p = 0.01$) (Figure 7P).

To further support the notion that C5/MCD reflects a MB COO, we conducted CyTOF on patients from an independent DLBCL cohort (Table S6) (Nissen et al., 2019). Cells from reactive LN specimens were used to define B cell subpopulations. In these samples, GCB were identified as CD10^{hi}CD38^{hi}, whereas MB showed lower levels of these markers and distinctive CD27 upregulation (Figure 7Q) (Agematsu et al., 2000). GCB-DLBCL cases, included as controls, mapped to GCB reference populations (not shown). In contrast, ABC-DLBCL tumors carrying *TBL1XR1* and MCD/C5 canonical mutations narrowly recapitulate the surface marker profile of MB cells (Figure 7R). The MB profile was also observed in MCD DLBCLs without *TBL1XR1* mutations (Figure 7S), consistent with the notion that MCD tumors arise from MB, albeit through distinct mutational trajectories. Collectively, we find that TBL1XR1 LOF drives expansion of aberrant MB cells with enhanced tendency to reenter GC reactions, ultimately resulting in canonical post-GC extranodal ABC-DLBCL with MB-like features and revealing the manner in which these tumors arise naturally from the humoral immune response.

DISCUSSION

Here, we show how *TBL1XR1* mutations result in transcriptional re-wiring of GCB cells to drive lymphomagenesis. A previous report noted TBL1XR1 interaction with BCL6 in a lymphoma cell line, using mass spectrometry (Miles et al., 2005). We observed that TBL1XR1 forms complexes with BCL6 at the chromatin level, and its interactome is largely confined to the SMRT complex and the TFs BCL6 and BACH2. In GCB, BCL6-SMRT complexes transiently poise enhancers controlling terminal differentiation, immune synapse signaling, and cell-cycle checkpoint genes, thus enabling proliferative bursts (Hatzi et al., 2013; Jiang et al., 2017). Accordingly, the GC reaction in *Tbl1xr1* LOF mice was significantly impaired, and GCB showed upregulation of BCL6 targets. Whereas *Bcl6*-KO completely abrogates GC formation (Hatzi and Melnick, 2014), *Tbl1xr1* LOF effects are reminiscent of the milder effects observed in mice carrying NCOR/SMRT LOF mutations that disrupt interaction with HDAC3 (Jiang et al., 2017) or *Hdac3* conditional deletion (Stengel et al., 2019). The difference in severity between BCL6 versus TBL1XR1/SMRT complex deficiency phenotype is likely due to SMRT/HDAC3-independent BCL6 functions such as interaction with BCOR and LSD1 (Hatzi et al., 2019).

TBL1XR1's lack of enzymatic activity has largely hindered efforts to elucidate its function. Still, one study proposed that TBL1XR1 acts as a repressor/coactivator exchange factor for hormone receptors (Perissi et al., 2004). In this model, TBL1XR1 recruited UbcH5 and the 19S proteasome, leading to SMRT degradation. This finding was not reproduced by later studies (Huang et al., 2009; Yoon et al., 2005; Zhang et al., 2006), and

Figure 6. *Tbl1xr1* Mutant MB Cells Preferentially Become GCB upon Recall

(A and B) FC analysis of total or antigen-specific MB population in (A) spleen or (B) BM. See also Data S1BB–S1CC.

(C and D) FC analysis of IgG1$^+$ or IgM$^+$ splenic (C) GCB or (D) MB. See also Figure S6B and Data S1DD.

(E) FC profiling of donor-derived antigen-specific splenic MB. See also Figure S6L.

(F) Experimental scheme and timeline for (G)–(J).

(G–I) FC analysis of (G) total B220$^+$, (H) GCB, or (I) PC donor-derived antigen-specific cells, in the spleens of MB-recipient animals. See also Figure S6M.

(J) ELISA for NP-specific serum Ig in MB-recipients in (F). Graphs show difference between 0 and 3.5 days post-immunization.

Values represent mean ± SEM. Data reproducible with two repeats. p values calculated using unpaired two-tailed Student's t test.

Please cite this article in press as: Venturutti et al., TBL1XR1 Mutations Drive Extranodal Lymphoma by Inducing a Pro-tumorigenic Memory Fate, Cell (2020), https://doi.org/10.1016/j.cell.2020.05.049

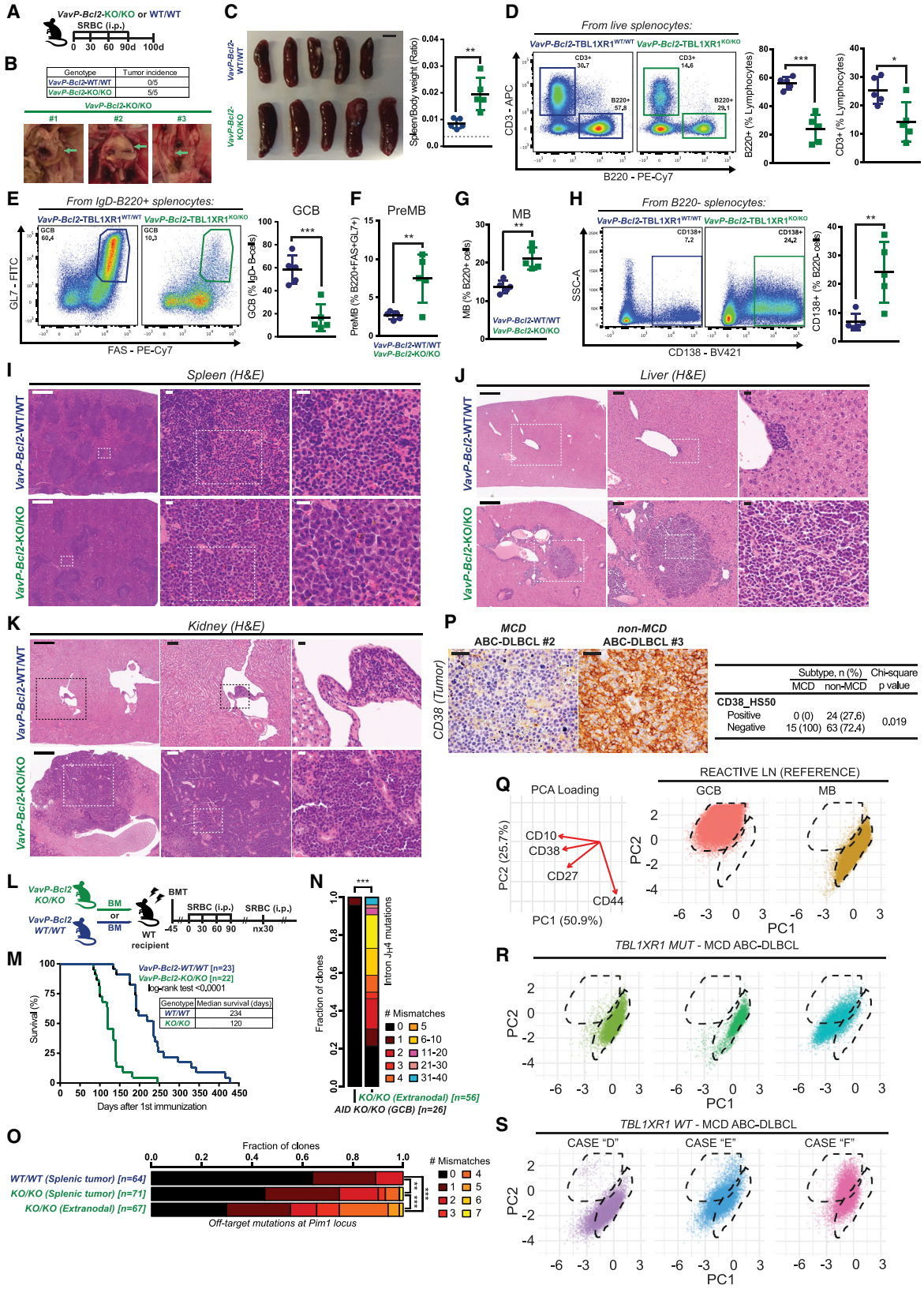

(legend on next page)

our own data show that in B cells, TBL1XR1^{MUT} had no effect on SMRT protein levels. Furthermore, our analysis of TBL1XR1 interactome failed to identify ubiquitin or proteasome machinery. In agreement with this, acute CD40L signaling (a differentiation cue for GCB) evicts SMRT from chromatin, without affecting its stability (Polo et al., 2008). Rather than altering SMRT turnover, *TBL1XR1* mutation or KO instead shift SMRT complex from BCL6 to BACH2, resulting in transcriptional reprogramming.

WD40 domains function as PPI or protein-DNA interaction motifs, mainly through aromatic residues on the surface of the β-propeller (reviewed in Jain and Pandey, 2018). Notably, these TBL1XR1 residues are the most frequently mutated in DLBCL. Structural studies show that TBL1XR1 forms tetramers and binds SMRT through its N-terminal domain (Oberoi et al., 2011; Zhang et al., 2002), which is largely spared by mutations. Hence, WD40 mutations would not be predicted to disrupt TBL1XR1-SMRT interaction. Accordingly, a study on Pierpont syndrome found that the interaction between TBL1XR1^{Y446C} (a mutant also found in DLBCL) and SMRT/HDAC3, was maintained *in vitro* (Heinen et al., 2016). The fact that TBL1XR1^{MUT} remains within the SMRT complex suggests that the WD40 plays a critical role in facilitating preferential association with BCL6, because TBL1XR1 KO yields a similar effect, both from the biological and biochemical standpoints. Importantly, the overall structure of the SMRT complex has not been resolved, but it will be necessary to understand how the holo-complex associates with BCL6 in the chromatin context and why TBL1XR1 LOF switches the conformation of the complex to favor binding to BACH2.

During the humoral immune response, B cells can transition to MB and PC phenotypes, with implications for formation of clonal precursor cells. Previous studies suggested a role for IL-9R signaling (Wang et al., 2017b), or the relative level of BCR affinity for antigen (Shinnakasu et al., 2016), as factors driving GCB into the (pre)MB compartment. In the case of TBL1XR1 LOF, preMB expansion is caused by switching the SMRT complex to BACH2 and away from BCL6. This situation is different from simple derepression of BCL6 target genes, which can enable differentiation to either PC or MB cell fate (Diehl et al., 2008; Ise et al., 2018; Kuo et al., 2007; Laidlaw et al., 2017). The reason for this is explained by the critical role of BACH2 in driving B cells toward the MB lineage (Shinnakasu et al., 2016), and the fact that PC master TF BLIMP1 is repressed both by BCL6 and BACH2 (Ochiai et al., 2006; Tunyaplin et al., 2004). Thus, in the TBL1XR1 LOF setting, BLIMP1 and the PC fate remain suppressed through the actions of BACH2-SMRT complexes. Notably, *Il9r* is a direct target gene of BLIMP1, and BLIMP1 LOF results in upregulation of *Il9r* transcripts (Minnich et al., 2016). Furthermore, transcriptional profiling of T cells from *Bach2*-KO mice revealed reduced levels of *Il9r* and increased levels of *Prdm1* (Geng et al., 2019). Accordingly, we found that *Il9r* plays an important role in mediating TBL1XR1 LOF-induced acquisition of preMB phenotypes. Beyond IL-9R, our findings provide a mechanistic explanation for how a switch to BACH2-driven programs might normally take place during the GC. In this view, somatic mutations of *TBL1XR1* simply exaggerate this effect, locking GC cell fate into the preMB pathway and expanding the population of pre-malignant MB cells, setting the stage for post-GC extranodal DLBCL lymphomagenesis.

Mutations affecting *TBL1XR1* associate with activating mutations in the BCR and TLR pathways (Chapuy et al., 2018; Schmitz et al., 2018), to define a group of aggressive extranodal post-GC lymphomas. Our finding that *Tbl1xr1* mutations disrupt canonical BCL6 transcriptional programs to drive GCB toward a post-GC/preMB stage is consistent with a MB COO for MCD/C5 DLBCLs. In agreement with this, lymphomas in KO/KO animals recapitulated canonical histological features of the human tumors, such as immunoblastic morphology, diffuse infiltration of extranodal tissues, and sparing of lymphoid follicles (Kashyap et al., 2011). The extrafollicular pattern may be linked to expression of MB-associated migratory chemokines induced by TBL1XR1^{MUT}, as part of the MB cell program. Indeed, the transcriptional profile of D370Y/WT GCB showed enrichment for post-GC-derived lymphoma transcriptomes and associated features, such as NF-κB/CD40 activation. An additional canonical MCD/C5 trait observed in our models was restriction in CSR (Lenz et al., 2007), with *Tbl1xr1* mutant and KO/KO cells

Figure 7. *Tbl1xr1* Alterations Lead to Extranodal Immunoblastic-like Lymphomas

(A) Experimental scheme and timeline for (B)–(K), (N), and (O).

(B) Incidence and representative images of macroscopic tumors found in *VavP-Bcl2-CD19Cre-Tbl1xr1$^{KO/KO}$* mice. Left to right: tumors associated to intestine, lungs, and para-aortic tissues. Numbers represent different animals.

(C) Spleens at time of necropsy. Scale, 500 mm. Graph shows spleen to body weight ratios. Dashed line represents average for non-*VavP-Bcl2* age-matched controls (n = 10).

(D–H) FC analysis of splenic (D) B/T cell populations, (E) GCB, (F) preMB, or (G) MB (B220$^+$CD138$^-$IgD$^-$FAS$^{-/lo}$GL7$^-$CD38$^+$), or (H) CD138$^+$ cells. See also Data S1HH–S1II.

(I) H&E of spleen sections from animals in (A). Scale, 500 μm (left) or 15 μm (center and right). See also Figure S7M.

(J and K) H&E of (J) liver or (K) kidney sections from animals in (A). Scale, 500 μm (left), 100 μm (center), and 15 μm (right).

(L) Experimental scheme and timeline for (M).

(M) Survival curve for *VavP-Bcl2;CD19Cre-Tbl1xr1$^{KO/KO}$* and *VavP-Bcl2;CD19Cre-Tbl1xr1$^{WT/WT}$* mice.

(N) SHM burden at Ig intron J_H4 in extranodal tumors from (A). Numbers in square brackets are total numbers of clones, pooled for 3 animals. *Aicda*$^{KO/KO}$ GCB were used as control.

(O) Mutation burden at *Pim1* locus in tumors from (A). Numbers in square brackets represent total clones, pooled for n = 5 per genotype.

(P) Representative images and quantification of CD38 IHC for MCD/C5 and non-MCD/C5 ABC-DLBCL human specimens. Scale, 20 μm.

(Q) Left: surface marker contribution to PCA loading. Right: PCA plots for MB and GCB from reactive LN, used as reference in CyTOF experiments.

(R and S) PCA for CyTOF profiling of human DLBCL specimens carrying canonical MCD/C5 lesions and (R) *TBL1XR1* mutations or (S) *TBL1XR1* WT alleles. See also Table S5.

Values represent mean ± SEM. Data reproducible with two repeats. p values calculated using unpaired two-tailed Student's t test (D)–(H), log-rank test (M), Wilcoxon rank-sum test with (O) or without (N) BH correction, or two-sided Chi-square test (P).

remaining largely as IgM$^+$. The selective preference for IgM expression could reflect possible benefits for the growth of post-GC lymphomas. We hypothesize that the increase in IgM$^+$ GC-derived populations is due to the strong bias introduced by *TBL1XR1* alterations toward the generation/expansion of immature MB with a high capacity to reenter the GC reaction. Most strikingly, both our *Tbl1xr1*-deficient murine lymphomas and primary human ABC-DLBCLs manifest an increased fraction of malignant cells with MB phenotype and a heavy burden of AID-induced on-target and off-target SHM. Importantly, this MB phenotype is observed in ABC-DLBCLs beyond those with *TBL1XR1* mutations, suggesting that there are additional mutational trajectories that favor this novel MB-cell associated malignant transformation pathway.

Tbl1xr1 mutations not only skew GC output toward MB, but also suppressed formation of Ab-secreting cells upon recall. Along these lines, it is notable that extinction of the BACH2 program is normally required for PC differentiation of MB (Kometani et al., 2013). Persistent BACH2-driven transcriptional programming in TBL1XR1^{MUT} MB could then explain the impairment in forming PC. Most strikingly, TBL1XR1^{MUT} MB cells showed an increased tendency to reenter new GC reactions. Cyclic reentry of BCL2-overexpressing MB into the GC reaction has been proposed to originate FLs (Sungalee et al., 2014). Presumably, these BCL2-overexpressing cells self-sustain and persist for long periods of time. However, we find that TBL1XR1^{MUT} expressly skew GC cell fate to produce the class of MB cells that are most prone to reenter the GC reaction, thus serving as clonal precursor cells to aggressive C5/MCD DLBCLs. The fact that *TBL1XR1* mutations in these lymphomas appear as early clonal events (Chapuy et al., 2018) further supports a model where TBL1XR1^{MUT} MB engage in successive rounds of GC reactions, eventually acquiring further hits in other genes (as shown here for *Pim1*) that further accelerate malignant transformation. This would likely explain the canonical complex phenotype of these tumors where they manifest an aberrant and heterogeneous composite of features reflecting aspects of MB, PB, and GCB. These results point to the need for surveillance studies in humans to identify precursor clonal cells at risk for transformation to these aggressive and incurable forms of DLBCL, much in the way current studies are attempting to predict which patients with clonal hematopoiesis of indeterminate prognosis are at risk for development of acute leukemia. The fact that this process is dependent on the SMRT/HDAC3 complex points to the potential for newly reported selective HDAC3 inhibitors (Mondello et al., 2020) as therapeutic agents for these clonal disorders. Perhaps combining such compounds with blockade of IL-9R signaling could further potentiate their activity. The recent discovery that auto-immune disorders like Sjogren's disease are driven by MB cells harboring canonical MCD mutations (Singh et al., 2020; Wang et al., 2017a) point to the further potential medical impact of such therapeutic interventions.

STAR★METHODS

Detailed methods are provided in the online version of this paper and include the following:

SUPPLEMENTAL INFORMATION

Supplemental Information can be found online at https://doi.org/10.1016/j.cell.2020.05.049.

ACKNOWLEDGMENTS

We thank all members of the Melnick Lab for thoughtful discussions and suggestions, and Hao Shen for his support with mice colonies. We acknowledge the Epigenomics, Genomics, and Flow Cytometry cores (WCM); the Molecular Cytology core (MSKCC); and the Center of Comparative Medicine and Pathology (WCM/MSKCC). L.V. is a Career Development Program Fellow from the Leukemia and Lymphoma Society (5469-18). A.M.M. is supported by the National Cancer Institute (NCI-R35-CA220499), the Leukemia and Lymphoma Society (LLS-TRP-6572-19, LLS-SCOR-7012-16), the Chemotherapy Foundation, and the Follicular Lymphoma Consortium.

AUTHOR CONTRIBUTIONS

Conceptualization, L.V. and A.M.M.; Methodology, L.V., A.M.M., W.B., and Y.J.; Formal Analysis, L.V., M.T., A.Z., A.C., C.R.C., P.F., A.P.W., Y.K., O.E., and G.G.P.; Investigation, L.V., A.Z., D.K., J.M.P., L.B., T.C.L., W.B., Y.K., W.T.Y., M.D.N., and B.R.; Resources, L.M.S., J.C., C.S., D.W.S., R.D.M., and M.R.G.; Writing, L.V. and A.M.M.

DECLARATION OF INTERESTS

A.M.M. receives research funding for Janssen, is on the scientific board of KDAC Pharmaceuticals, and has consulted for Constellation and Epizyme. M.R.G. consults for Verastem Oncology.

Received: October 28, 2019
Revised: March 24, 2020
Accepted: May 27, 2020
Published: July 2, 2020

REFERENCES

Agematsu, K., Hokibara, S., Nagumo, H., and Komiyama, A. (2000). CD27: a memory B-cell marker. Immunol. Today *21*, 204–206.

Anderson, S.M., Tomayko, M.M., Ahuja, A., Haberman, A.M., and Shlomchik, M.J. (2007). New markers for murine memory B cells that define mutated and unmutated subsets. J. Exp. Med. *204*, 2103–2114.

Arnon, T.I., Horton, R.M., Grigorova, I.L., and Cyster, J.G. (2013). Visualization of splenic marginal zone B-cell shuttling and follicular B-cell egress. Nature *493*, 684–688.

Arpin, C., Déchanet, J., Van Kooten, C., Merville, P., Grouard, G., Brière, F., Banchereau, J., and Liu, Y.J. (1995). Generation of memory B cells and plasma cells in vitro. Science *268*, 720–722.

Arthur, S.E., Jiang, A., Grande, B.M., Alcaide, M., Cojocaru, R., Rushton, C.K., Mottok, A., Hilton, L.K., Lat, P.K., Zhao, E.Y., et al. (2018). Genome-wide discovery of somatic regulatory variants in diffuse large B-cell lymphoma. Nat. Commun. *9*, 4001.

Barnden, M.J., Allison, J., Heath, W.R., and Carbone, F.R. (1998). Defective TCR expression in transgenic mice constructed using cDNA-based alpha- and beta-chain genes under the control of heterologous regulatory elements. Immunol. Cell Biol. *76*, 34–40.

Baumjohann, D., Preite, S., Reboldi, A., Ronchi, F., Ansel, K.M., Lanzavecchia, A., and Sallusto, F. (2013). Persistent antigen and germinal center B cells sustain T follicular helper cell responses and phenotype. Immunity *38*, 596–605.

Béguelin, W., Popovic, R., Teater, M., Jiang, Y., Bunting, K.L., Rosen, M., Shen, H., Yang, S.N., Wang, L., Ezponda, T., et al. (2013). EZH2 is required for germinal center formation and somatic EZH2 mutations promote lymphoid transformation. Cancer Cell *23*, 677–692.

Béguelin, W., Rivas, M.A., Calvo Fernández, M.T., Teater, M., Purwada, A., Redmond, D., Shen, H., Challman, M.F., Elemento, O., Singh, A., and Melnick, A.M. (2017). EZH2 enables germinal centre formation through epigenetic silencing of CDKN1A and an Rb-E2F1 feedback loop. Nat. Commun. *8*, 877.

Beham-Schmid, C. (2017). Aggressive lymphoma 2016: revision of the WHO classification. Memo *10*, 248–254.

Cardenas, M.G., Yu, W., Beguelin, W., Teater, M.R., Geng, H., Goldstein, R.L., Oswald, E., Hatzi, K., Yang, S.N., Cohen, J., et al. (2016). Rationally designed BCL6 inhibitors target activated B cell diffuse large B cell lymphoma. J. Clin. Invest. *126*, 3351–3362.

Casola, S., Cattoretti, G., Uyttersprot, N., Koralov, S.B., Seagal, J., Hao, Z., Waisman, A., Egert, A., Ghitza, D., and Rajewsky, K. (2006). Tracking germinal center B cells expressing germ-line immunoglobulin gamma1 transcripts by conditional gene targeting. Proc. Natl. Acad. Sci. USA *103*, 7396–7401.

Cattoretti, G., Pasqualucci, L., Ballon, G., Tam, W., Nandula, S.V., Shen, Q., Mo, T., Murty, V.V., and Dalla-Favera, R. (2005). Deregulated BCL6 expression recapitulates the pathogenesis of human diffuse large B cell lymphomas in mice. Cancer Cell *7*, 445–455.

Cerchietti, L.C., Ghetu, A.F., Zhu, X., Da Silva, G.F., Zhong, S., Matthews, M., Bunting, K.L., Polo, J.M., Farès, C., Arrowsmith, C.H., et al. (2010). A small-molecule inhibitor of BCL6 kills DLBCL cells in vitro and in vivo. Cancer Cell *17*, 400–411.

Chapuy, B., Roemer, M.G., Stewart, C., Tan, Y., Abo, R.P., Zhang, L., Dunford, A.J., Meredith, D.M., Thorner, A.R., Jordanova, E.S., et al. (2016). Targetable genetic features of primary testicular and primary central nervous system lymphomas. Blood *127*, 869–881.

Chapuy, B., Stewart, C., Dunford, A.J., Kim, J., Kamburov, A., Redd, R.A., Lawrence, M.S., Roemer, M.G.M., Li, A.J., Ziepert, M., et al. (2018). Molecular subtypes of diffuse large B cell lymphoma are associated with distinct pathogenic mechanisms and outcomes. Nat. Med. *24*, 679–690.

Choi, H., Larsen, B., Lin, Z.Y., Breitkreutz, A., Mellacheruvu, D., Fermin, D., Qin, Z.S., Tyers, M., Gingras, A.C., and Nesvizhskii, A.I. (2011). SAINT: probabilistic scoring of affinity purification-mass spectrometry data. Nat. Methods *8*, 70–73.

Cibulskis, K., Lawrence, M.S., Carter, S.L., Sivachenko, A., Jaffe, D., Sougnez, C., Gabriel, S., Meyerson, M., Lander, E.S., and Getz, G. (2013). Sensitive detection of somatic point mutations in impure and heterogeneous cancer samples. Nat. Biotechnol. *31*, 213–219.

Cingolani, P., Platts, A., Wang, L., Coon, M., Nguyen, T., Wang, L., Land, S.J., Lu, X., and Ruden, D.M. (2012). A program for annotating and predicting the effects of single nucleotide polymorphisms, SnpEff: SNPs in the genome of Drosophila melanogaster strain w1118; iso-2; iso-3. Fly (Austin) *6*, 80–92.

Cock, P.J., Antao, T., Chang, J.T., Chapman, B.A., Cox, C.J., Dalke, A., Friedberg, I., Hamelryck, T., Kauff, F., Wilczynski, B., and de Hoon, M.J. (2009). Biopython: freely available Python tools for computational molecular biology and bioinformatics. Bioinformatics *25*, 1422–1423.

Craig, R., and Beavis, R.C. (2004). TANDEM: matching proteins with tandem mass spectra. Bioinformatics *20*, 1466–1467.

Cyster, J.G., and Allen, C.D.C. (2019). B Cell Responses: Cell Interaction Dynamics and Decisions. Cell *177*, 524–540.

Diehl, S.A., Schmidlin, H., Nagasawa, M., van Haren, S.D., Kwakkenbos, M.J., Yasuda, E., Beaumont, T., Scheeren, F.A., and Spits, H. (2008). STAT3-mediated up-regulation of BLIMP1 Is coordinated with BCL6 down-regulation to control human plasma cell differentiation. J. Immunol. *180*, 4805–4815.

Dobin, A., Davis, C.A., Schlesinger, F., Drenkow, J., Zaleski, C., Jha, S., Batut, P., Chaisson, M., and Gingeras, T.R. (2013). STAR: ultrafast universal RNA-seq aligner. Bioinformatics *29*, 15–21.

Dogan, I., Bertocci, B., Vilmont, V., Delbos, F., Mégret, J., Storck, S., Reynaud, C.A., and Weill, J.C. (2009). Multiple layers of B cell memory with different effector functions. Nat. Immunol. *10*, 1292–1299.

Dominguez, P.M., Ghamlouch, H., Rosikiewicz, W., Kumar, P., Béguelin, W., Fontán, L., Rivas, M.A., Pawlikowska, P., Armand, M., Mouly, E., et al. (2018). TET2 Deficiency Causes Germinal Center Hyperplasia, Impairs Plasma Cell Differentiation, and Promotes B-cell Lymphomagenesis. Cancer Discov. *8*, 1632–1653.

Egle, A., Harris, A.W., Bath, M.L., O'Reilly, L., and Cory, S. (2004). VavP-Bcl2 transgenic mice develop follicular lymphoma preceded by germinal center hyperplasia. Blood *103*, 2276–2283.

Ennishi, D., Mottok, A., Ben-Neriah, S., Shulha, H.P., Farinha, P., Chan, F.C., Meissner, B., Boyle, M., Hother, C., Kridel, R., et al. (2017). Genetic profiling of *MYC* and *BCL2* in diffuse large B-cell lymphoma determines cell-of-origin-specific clinical impact. Blood *129*, 2760–2770.

Gavrieli, Y., Sherman, Y., and Ben-Sasson, S.A. (1992). Identification of programmed cell death in situ via specific labeling of nuclear DNA fragmentation. J. Cell Biol. *119*, 493–501.

Geng, J., Wei, H., Shi, B., Wang, Y.H., Greer, B.D., Pittman, M., Smith, E., Thomas, P.G., Kutsch, O., and Hu, H. (2019). Bach2 Negatively Regulates T Follicular Helper Cell Differentiation and Is Critical for $CD4^+$ T Cell Memory. J. Immunol. *202*, 2991–2998.

Gonzalez-Aguilar, A., Idbaih, A., Boisselier, B., Habbita, N., Rossetto, M., Laurenge, A., Bruno, A., Jouvet, A., Polivka, M., Adam, C., et al. (2012). Recurrent mutations of MYD88 and TBL1XR1 in primary central nervous system lymphomas. Clin. Cancer Res. *18*, 5203–5211.

Goodarzi, H., Elemento, O., and Tavazoie, S. (2009). Revealing global regulatory perturbations across human cancers. Mol. Cell *36*, 900–911.

Hashwah, H., Schmid, C.A., Kasser, S., Bertram, K., Stelling, A., Manz, M.G., and Müller, A. (2017). Inactivation of CREBBP expands the germinal center B

cell compartment, down-regulates MHCII expression and promotes DLBCL growth. Proc. Natl. Acad. Sci. USA *114*, 9701–9706.

Hatzi, K., and Melnick, A. (2014). Breaking bad in the germinal center: how deregulation of BCL6 contributes to lymphomagenesis. Trends Mol. Med. *20*, 343–352.

Hatzi, K., Jiang, Y., Huang, C., Garrett-Bakelman, F., Gearhart, M.D., Giannopoulou, E.G., Zumbo, P., Kirouac, K., Bhaskara, S., Polo, J.M., et al. (2013). A hybrid mechanism of action for BCL6 in B cells defined by formation of functionally distinct complexes at enhancers and promoters. Cell Rep. *4*, 578–588.

Hatzi, K., Geng, H., Doane, A.S., Meydan, C., LaRiviere, R., Cardenas, M., Duy, C., Shen, H., Vidal, M.N.C., Baslan, T., et al. (2019). Histone demethylase LSD1 is required for germinal center formation and BCL6-driven lymphomagenesis. Nat. Immunol. *20*, 86–96.

Heinen, C.A., Jongejan, A., Watson, P.J., Redeker, B., Boelen, A., Boudzovitch-Surovtseva, O., Forzano, F., Hordijk, R., Kelley, R., Olney, A.H., et al. (2016). A specific mutation in TBL1XR1 causes Pierpont syndrome. J. Med. Genet. *53*, 330–337.

Hill, J.T., Demarest, B.L., Bisgrove, B.W., Su, Y.C., Smith, M., and Yost, H.J. (2014). Poly peak parser: Method and software for identification of unknown indels using sanger sequencing of polymerase chain reaction products. Dev. Dyn. *243*, 1632–1636.

Huang, W., Ghisletti, S., Perissi, V., Rosenfeld, M.G., and Glass, C.K. (2009). Transcriptional integration of TLR2 and TLR4 signaling at the NCoR derepression checkpoint. Mol. Cell *35*, 48–57.

Huang, C., Geng, H., Boss, I., Wang, L., and Melnick, A. (2014). Cooperative transcriptional repression by BCL6 and BACH2 in germinal center B-cell differentiation. Blood *123*, 1012–1020.

Ise, W., Fujii, K., Shiroguchi, K., Ito, A., Kometani, K., Takeda, K., Kawakami, E., Yamashita, K., Suzuki, K., Okada, T., et al. (2018). T Follicular Helper Cell-Germinal Center B Cell Interaction Strength Regulates Entry into Plasma Cell or Recycling Germinal Center Cell Fate. Immunity *48*, 702–715.

Jain, B.P., and Pandey, S. (2018). WD40 Repeat Proteins: Signalling Scaffold with Diverse Functions. Protein J. *37*, 391–406.

Jiang, Y., Ortega-Molina, A., Geng, H., Ying, H.Y., Hatzi, K., Parsa, S., McNally, D., Wang, L., Doane, A.S., Agirre, X., et al. (2017). CREBBP Inactivation Promotes the Development of HDAC3-Dependent Lymphomas. Cancer Discov. *7*, 38–53.

Jolly, C.J., Klix, N., and Neuberger, M.S. (1997). Rapid methods for the analysis of immunoglobulin gene hypermutation: application to transgenic and gene targeted mice. Nucleic Acids Res. *25*, 1913–1919.

Kashyap, R., Rai Mittal, B., Manohar, K., Balasubramanian Harisankar, C.N., Bhattacharya, A., Singh, B., Malhotra, P., and Varma, S. (2011). Extranodal manifestations of lymphoma on [^{18}F]FDG-PET/CT: a pictorial essay. Cancer Imaging *11*, 166–174.

Kessner, D., Chambers, M., Burke, R., Agus, D., and Mallick, P. (2008). ProteoWizard: open source software for rapid proteomics tools development. Bioinformatics *24*, 2534–2536.

Kitamura, D., Roes, J., Kühn, R., and Rajewsky, K. (1991). A B cell-deficient mouse by targeted disruption of the membrane exon of the immunoglobulin mu chain gene. Nature *350*, 423–426.

Koboldt, D.C., Zhang, Q., Larson, D.E., Shen, D., McLellan, M.D., Lin, L., Miller, C.A., Mardis, E.R., Ding, L., and Wilson, R.K. (2012). VarScan 2: somatic mutation and copy number alteration discovery in cancer by exome sequencing. Genome Res. *22*, 568–576.

Kometani, K., Nakagawa, R., Shinnakasu, R., Kaji, T., Rybouchkin, A., Moriyama, S., Furukawa, K., Koseki, H., Takemori, T., and Kurosaki, T. (2013). Repression of the transcription factor Bach2 contributes to predisposition of IgG1 memory B cells toward plasma cell differentiation. Immunity *39*, 136–147.

Kowarz, E., Löscher, D., and Marschalek, R. (2015). Optimized Sleeping Beauty transposons rapidly generate stable transgenic cell lines. Biotechnol. J. *10*, 647–653.

Krysiak, K., Gomez, F., White, B.S., Matlock, M., Miller, C.A., Trani, L., Fronick, C.C., Fulton, R.S., Kreisel, F., Cashen, A.F., et al. (2017). Recurrent somatic mutations affecting B-cell receptor signaling pathway genes in follicular lymphoma. Blood *129*, 473–483.

Kuo, T.C., Shaffer, A.L., Haddad, J., Jr., Choi, Y.S., Staudt, L.M., and Calame, K. (2007). Repression of BCL-6 is required for the formation of human memory B cells in vitro. J. Exp. Med. *204*, 819–830.

Laidlaw, B.J., Schmidt, T.H., Green, J.A., Allen, C.D., Okada, T., and Cyster, J.G. (2017). The Eph-related tyrosine kinase ligand Ephrin-B1 marks germinal center and memory precursor B cells. J. Exp. Med. *214*, 639–649.

Laskowski, R.A., Tyagi, N., Johnson, D., Joss, S., Kinning, E., McWilliam, C., Splitt, M., Thornton, J.M., Firth, H.V., and Wright, C.F.; DDD Study (2016). Integrating population variation and protein structural analysis to improve clinical interpretation of missense variation: application to the WD40 domain. Hum. Mol. Genet. *25*, 927–935.

Lenz, G., Nagel, I., Siebert, R., Roschke, A.V., Sanger, W., Wright, G.W., Dave, S.S., Tan, B., Zhao, H., Rosenwald, A., et al. (2007). Aberrant immunoglobulin class switch recombination and switch translocations in activated B cell-like diffuse large B cell lymphoma. J. Exp. Med. *204*, 633–643.

Li, J., and Wang, C.Y. (2008). TBL1-TBLR1 and beta-catenin recruit each other to Wnt target-gene promoter for transcription activation and oncogenesis. Nat. Cell Biol. *10*, 160–169.

Liao, Y., Smyth, G.K., and Shi, W. (2014). featureCounts: an efficient general purpose program for assigning sequence reads to genomic features. Bioinformatics *30*, 923–930.

Liu, M., Duke, J.L., Richter, D.J., Vinuesa, C.G., Goodnow, C.C., Kleinstein, S.H., and Schatz, D.G. (2008). Two levels of protection for the B cell genome during somatic hypermutation. Nature *451*, 841–845.

Liu, G., Zhang, J., Larsen, B., Stark, C., Breitkreutz, A., Lin, Z.Y., Breitkreutz, B.J., Ding, Y., Colwill, K., Pasculescu, A., et al. (2010). ProHits: integrated software for mass spectrometry-based interaction proteomics. Nat. Biotechnol. *28*, 1015–1017.

Luckey, C.J., Bhattacharya, D., Goldrath, A.W., Weissman, I.L., Benoist, C., and Mathis, D. (2006). Memory T and memory B cells share a transcriptional program of self-renewal with long-term hematopoietic stem cells. Proc. Natl. Acad. Sci. USA *103*, 3304–3309.

Ma, M.C.J., Tadros, S., Bouska, A., Heavican, T.B., Yang, H., Deng, Q., Moore, D., Akhter, A., Hartert, K., Jain, N., et al. (2019). Pathognomonic and epistatic genetic alterations in B-cell non-Hodgkin lymphoma. bioRxiv. https://doi.org/10.1101/674259.

Mátés, L., Chuah, M.K., Belay, E., Jerchow, B., Manoj, N., Acosta-Sanchez, A., Grzela, D.P., Schmitt, A., Becker, K., Matrai, J., et al. (2009). Molecular evolution of a novel hyperactive Sleeping Beauty transposase enables robust stable gene transfer in vertebrates. Nat. Genet. *41*, 753–761.

Mayer, C.T., Gazumyan, A., Kara, E.E., Gitlin, A.D., Golijanin, J., Viant, C., Pai, J., Oliveira, T.Y., Wang, Q., Escolano, A., et al. (2017). The microanatomic segregation of selection by apoptosis in the germinal center. Science *358*, eaao2602.

Mellacheruvu, D., Wright, Z., Couzens, A.L., Lambert, J.P., St-Denis, N.A., Li, T., Miteva, Y.V., Hauri, S., Sardiu, M.E., Low, T.Y., et al. (2013). The CRAPome: a contaminant repository for affinity purification-mass spectrometry data. Nat. Methods *10*, 730–736.

Miles, R.R., Crockett, D.K., Lim, M.S., and Elenitoba-Johnson, K.S. (2005). Analysis of BCL6-interacting proteins by tandem mass spectrometry. Mol. Cell. Proteomics *4*, 1898–1909.

Minnich, M., Tagoh, H., Bönelt, P., Axelsson, E., Fischer, M., Cebolla, B., Tarakhovsky, A., Nutt, S.L., Jaritz, M., and Busslinger, M. (2016). Multifunctional role of the transcription factor Blimp-1 in coordinating plasma cell differentiation. Nat. Immunol. *17*, 331–343.

Mohammed, H., Taylor, C., Brown, G.D., Papachristou, E.K., Carroll, J.S., and D'Santos, C.S. (2016). Rapid immunoprecipitation mass spectrometry of endogenous proteins (RIME) for analysis of chromatin complexes. Nat. Protoc. *11*, 316–326.

Mondello, P., Tadros, S., Teater, M., Fontan, L., Chang, A.Y., Jain, N., Yang, H., Singh, S., Ying, H.Y., Chu, C.S., et al. (2020). Selective Inhibition of

HDAC3 Targets Synthetic Vulnerabilities and Activates Immune Surveillance in Lymphoma. Cancer Discov. *10*, 440–459.

Mort, R.L., Ford, M.J., Sakaue-Sawano, A., Lindstrom, N.O., Casadio, A., Douglas, A.T., Keighren, M.A., Hohenstein, P., Miyawaki, A., and Jackson, I.J. (2014). Fucci2a: a bicistronic cell cycle reporter that allows Cre mediated tissue specific expression in mice. Cell Cycle *13*, 2681–2696.

Muramatsu, M., Kinoshita, K., Fagarasan, S., Yamada, S., Shinkai, Y., and Honjo, T. (2000). Class switch recombination and hypermutation require activation-induced cytidine deaminase (AID), a potential RNA editing enzyme. Cell *102*, 553–563.

National Research Council (US) Institute for Laboratory Animal Research (1996). Guide for the Care and Use of Laboratory Animals (Washington, DC: National Academies Press (US)). https://www.ncbi.nlm.nih.gov/books/NBK232589/ doi: 10.17226/5140.

Nissen, M.D., Kusakabe, M., Wang, X., Simkin, G., Gracias, D., Tyshchenko, K., Hill, A., Meskas, J., Hung, S., Chavez, E.A., et al. (2019). Single Cell Phenotypic Profiling of 27 DLBCL Cases Reveals Marked Intertumoral and Intratumoral Heterogeneity. Cytometry A. Published online October 22, 2019. https://doi.org/10.1002/cyto.a.23919.

Nojima, T., Haniuda, K., Moutai, T., Matsudaira, M., Mizokawa, S., Shiratori, I., Azuma, T., and Kitamura, D. (2011). In-vitro derived germinal centre B cells differentially generate memory B or plasma cells in vivo. Nat. Commun. *2*, 465.

Oberoi, J., Fairall, L., Watson, P.J., Yang, J.C., Czimmerer, Z., Kampmann, T., Goult, B.T., Greenwood, J.A., Gooch, J.T., Kallenberger, B.C., et al. (2011). Structural basis for the assembly of the SMRT/NCoR core transcriptional repression machinery. Nat. Struct. Mol. Biol. *18*, 177–184.

Ochiai, K., Katoh, Y., Ikura, T., Hoshikawa, Y., Noda, T., Karasuyama, H., Tashiro, S., Muto, A., and Igarashi, K. (2006). Plasmacytic transcription factor Blimp-1 is repressed by Bach2 in B cells. J. Biol. Chem. *281*, 38226–38234.

Ogilvy, S., Metcalf, D., Print, C.G., Bath, M.L., Harris, A.W., and Adams, J.M. (1999). Constitutive Bcl-2 expression throughout the hematopoietic compartment affects multiple lineages and enhances progenitor cell survival. Proc. Natl. Acad. Sci. USA *96*, 14943–14948.

Oliver, A.M., Martin, F., and Kearney, J.F. (1997). Mouse CD38 is down-regulated on germinal center B cells and mature plasma cells. J. Immunol. *158*, 1108–1115.

Ortega-Molina, A., Boss, I.W., Canela, A., Pan, H., Jiang, Y., Zhao, C., Jiang, M., Hu, D., Agirre, X., Niesvizky, I., et al. (2015). The histone lysine methyltransferase KMT2D sustains a gene expression program that represses B cell lymphoma development. Nat. Med. *21*, 1199–1208.

Pagès, H., Aboyoun, P., Gentleman, R., and DebRoy, S. (2019). Biostrings: Efficient manipulation of biological strings. R package version 2.54.0. https://bioconductor.org/packages/release/bioc/html/Biostrings.html.

Pereira, J.P., Kelly, L.M., Xu, Y., and Cyster, J.G. (2009). EBI2 mediates B cell segregation between the outer and centre follicle. Nature *460*, 1122–1126.

Perissi, V., Aggarwal, A., Glass, C.K., Rose, D.W., and Rosenfeld, M.G. (2004). A corepressor/coactivator exchange complex required for transcriptional activation by nuclear receptors and other regulated transcription factors. Cell *116*, 511–526.

Phelan, J.D., Young, R.M., Webster, D.E., Roulland, S., Wright, G.W., Kasbekar, M., Shaffer, A.L., 3rd, Ceribelli, M., Wang, J.Q., Schmitz, R., et al. (2018). A multiprotein supercomplex controlling oncogenic signalling in lymphoma. Nature *560*, 387–391.

Polo, J.M., Ci, W., Licht, J.D., and Melnick, A. (2008). Reversible disruption of BCL6 repression complexes by CD40 signaling in normal and malignant B cells. Blood *112*, 644–651.

Reddy, A., Zhang, J., Davis, N.S., Moffitt, A.B., Love, C.L., Waldrop, A., Leppa, S., Pasanen, A., Meriranta, L., Karjalainen-Lindsberg, M.L., et al. (2017). Genetic and Functional Drivers of Diffuse Large B Cell Lymphoma. Cell *171*, 481–494.

Ridderstad, A., and Tarlinton, D.M. (1998). Kinetics of establishing the memory B cell population as revealed by CD38 expression. J. Immunol. *160*, 4688–4695.

Robinson, M.D., McCarthy, D.J., and Smyth, G.K. (2010). edgeR: a Bioconductor package for differential expression analysis of digital gene expression data. Bioinformatics *26*, 139–140.

Roux, K.J., Kim, D.I., Raida, M., and Burke, B. (2012). A promiscuous biotin ligase fusion protein identifies proximal and interacting proteins in mammalian cells. J. Cell Biol. *196*, 801–810.

Saunders, C.T., Wong, W.S., Swamy, S., Becq, J., Murray, L.J., and Cheetham, R.K. (2012). Strelka: accurate somatic small-variant calling from sequenced tumor-normal sample pairs. Bioinformatics *28*, 1811–1817.

Schindelin, J., Arganda-Carreras, I., Frise, E., Kaynig, V., Longair, M., Pietzsch, T., Preibisch, S., Rueden, C., Saalfeld, S., Schmid, B., et al. (2012). Fiji: an open-source platform for biological-image analysis. Nat. Methods *9*, 676–682.

Schmitz, R., Wright, G.W., Huang, D.W., Johnson, C.A., Phelan, J.D., Wang, J.Q., Roulland, S., Kasbekar, M., Young, R.M., Shaffer, A.L., et al. (2018). Genetics and Pathogenesis of Diffuse Large B-Cell Lymphoma. N. Engl. J. Med. *378*, 1396–1407.

Schneider, C.A., Rasband, W.S., and Eliceiri, K.W. (2012). NIH Image to ImageJ: 25 years of image analysis. Nat. Methods *9*, 671–675.

Scott, D.W., Mottok, A., Ennishi, D., Wright, G.W., Farinha, P., Ben-Neriah, S., Kridel, R., Barry, G.S., Hother, C., Abrisqueta, P., et al. (2015). Prognostic Significance of Diffuse Large B-Cell Lymphoma Cell of Origin Determined by Digital Gene Expression in Formalin-Fixed Paraffin-Embedded Tissue Biopsies. J. Clin. Oncol. *33*, 2848–2856.

Sherry, S.T., Ward, M.H., Kholodov, M., Baker, J., Phan, L., Smigielski, E.M., and Sirotkin, K. (2001). dbSNP: the NCBI database of genetic variation. Nucleic Acids Res. *29*, 308–311.

Shinnakasu, R., Inoue, T., Kometani, K., Moriyama, S., Adachi, Y., Nakayama, M., Takahashi, Y., Fukuyama, H., Okada, T., and Kurosaki, T. (2016). Regulated selection of germinal-center cells into the memory B cell compartment. Nat. Immunol. *17*, 861–869.

Singh, M., Jackson, K.J.L., Wang, J.J., Schofield, P., Field, M.A., Koppstein, D., Peters, T.J., Burnett, D.L., Rizzetto, S., Nevoltris, D., et al. (2020). Lymphoma Driver Mutations in the Pathogenic Evolution of an Iconic Human Autoantibody. Cell *180*, 878–894.

Stengel, K.R., Bhaskara, S., Wang, J., Liu, Q., Ellis, J.D., Sampathi, S., and Hiebert, S.W. (2019). Histone deacetylase 3 controls a transcriptional network required for B cell maturation. Nucleic Acids Res. *47*, 10612–10627.

Stewart, S.A., Dykxhoorn, D.M., Palliser, D., Mizuno, H., Yu, E.Y., An, D.S., Sabatini, D.M., Chen, I.S., Hahn, W.C., Sharp, P.A., et al. (2003). Lentivirus-delivered stable gene silencing by RNAi in primary cells. RNA *9*, 493–501.

Stewart, I., Radtke, D., Phillips, B., McGowan, S.J., and Bannard, O. (2018). Germinal Center B Cells Replace Their Antigen Receptors in Dark Zones and Fail Light Zone Entry when Immunoglobulin Gene Mutations are Damaging. Immunity *49*, 477–489.

Suan, D., Krautler, N.J., Maag, J.L.V., Butt, D., Bourne, K., Hermes, J.R., Avery, D.T., Young, C., Statham, A., Elliott, M., et al. (2017). CCR6 Defines Memory B Cell Precursors in Mouse and Human Germinal Centers, Revealing Light-Zone Location and Predominant Low Antigen Affinity. Immunity *47*, 1142–1153.

Subramanian, A., Tamayo, P., Mootha, V.K., Mukherjee, S., Ebert, B.L., Gillette, M.A., Paulovich, A., Pomeroy, S.L., Golub, T.R., Lander, E.S., and Mesirov, J.P. (2005). Gene set enrichment analysis: a knowledge-based approach for interpreting genome-wide expression profiles. Proc. Natl. Acad. Sci. USA *102*, 15545–15550.

Sungalee, S., Mamessier, E., Morgado, E., Grégoire, E., Brohawn, P.Z., Morehouse, C.A., Jouve, N., Monvoisin, C., Menard, C., Debroas, G., et al. (2014). Germinal center reentries of BCL2-overexpressing B cells drive follicular lymphoma progression. J. Clin. Invest. *124*, 5337–5351.

Tate, J.G., Bamford, S., Jubb, H.C., Sondka, Z., Beare, D.M., Bindal, N., Boutselakis, H., Cole, C.G., Creatore, C., Dawson, E., et al. (2019). COSMIC: the Catalogue Of Somatic Mutations In Cancer. Nucleic Acids Res. *47* (D1), D941–D947.

Tomita, A., Buchholz, D.R., and Shi, Y.B. (2004). Recruitment of N-CoR/SMRT-TBLR1 corepressor complex by unliganded thyroid hormone receptor for gene repression during frog development. Mol. Cell. Biol. *24*, 3337–3346.

Tunyaplin, C., Shaffer, A.L., Angelin-Duclos, C.D., Yu, X., Staudt, L.M., and Calame, K.L. (2004). Direct repression of prdm1 by Bcl-6 inhibits plasmacytic differentiation. J. Immunol. *173*, 1158–1165.

Wang, Y., Hu, X.J., Zou, X.D., Wu, X.H., Ye, Z.Q., and Wu, Y.D. (2015). WDSPdb: a database for WD40-repeat proteins. Nucleic Acids Res. *43*, D339–D344.

Wang, J.Q., Jeelall, Y.S., Humburg, P., Batchelor, E.L., Kaya, S.M., Yoo, H.M., Goodnow, C.C., and Horikawa, K. (2017a). Synergistic cooperation and cross-talk between *MYD88*^{L265P} and mutations that dysregulate CD79B and surface IgM. J. Exp. Med. *214*, 2759–2776.

Wang, Y., Shi, J., Yan, J., Xiao, Z., Hou, X., Lu, P., Hou, S., Mao, T., Liu, W., Ma, Y., et al. (2017b). Germinal-center development of memory B cells driven by IL-9 from follicular helper T cells. Nat. Immunol. *18*, 921–930.

Weisel, F.J., Zuccarino-Catania, G.V., Chikina, M., and Shlomchik, M.J. (2016). A Temporal Switch in the Germinal Center Determines Differential Output of Memory B and Plasma Cells. Immunity *44*, 116–130.

Wright, G., Tan, B., Rosenwald, A., Hurt, E.H., Wiestner, A., and Staudt, L.M. (2003). A gene expression-based method to diagnose clinically distinct subgroups of diffuse large B cell lymphoma. Proc. Natl. Acad. Sci. USA *100*, 9991–9996.

Wright, G.W., Huang, D.W., Phelan, J.D., Coulibaly, Z.A., Roulland, S., Young, R.M., Wang, J.Q., Schmitz, R., Morin, R.D., Tang, J., et al. (2020). A Probabilistic Classification Tool for Genetic Subtypes of Diffuse Large B Cell Lymphoma with Therapeutic Implications. Cancer Cell *37*, 551–568.e14.

Yoon, H.G., Chan, D.W., Huang, Z.Q., Li, J., Fondell, J.D., Qin, J., and Wong, J. (2003). Purification and functional characterization of the human N-CoR complex: the roles of HDAC3, TBL1 and TBLR1. EMBO J. *22*, 1336–1346.

Yoon, H.G., Choi, Y., Cole, P.A., and Wong, J. (2005). Reading and function of a histone code involved in targeting corepressor complexes for repression. Mol. Cell. Biol. *25*, 324–335.

Zhang, J., Kalkum, M., Chait, B.T., and Roeder, R.G. (2002). The N-CoR-HDAC3 nuclear receptor corepressor complex inhibits the JNK pathway through the integral subunit GPS2. Mol. Cell *9*, 611–623.

Zhang, X.M., Chang, Q., Zeng, L., Gu, J., Brown, S., and Basch, R.S. (2006). TBLR1 regulates the expression of nuclear hormone receptor co-repressors. BMC Cell Biol. *7*, 31.

Zuccarino-Catania, G.V., Sadanand, S., Weisel, F.J., Tomayko, M.M., Meng, H., Kleinstein, S.H., Good-Jacobson, K.L., and Shlomchik, M.J. (2014). CD80 and PD-L2 define functionally distinct memory B cell subsets that are independent of antibody isotype. Nat. Immunol. *15*, 631–637.

Please cite this article in press as: Venturutti et al., TBL1XR1 Mutations Drive Extranodal Lymphoma by Inducing a Pro-tumorigenic Memory Fate, Cell (2020), https://doi.org/10.1016/j.cell.2020.05.049

CellPress

STAR★METHODS

KEY RESOURCES TABLE

REAGENT or RESOURCE	SOURCE	IDENTIFIER
Antibodies		
Rat APC anti-CD38	eBioscience ThermoFisher Scientific	Cat# 17-0381; , RRID:AB_469381
Rat PE anti-CXCR4	eBioscience ThermoFisher Scientific	Cat# 12-9991; RRID:AB_891393
Mouse PerCP-Cy5.5 anti-CD45.1	eBioscience ThermoFisher Scientific	Cat# 45-0453; RRID:AB_1107003
Armenian Hamster FITC anti-PD-1	eBioscience ThermoFisher Scientific	Cat# 11-9985; RRID:AB_465473
Rat anti-mouse CD16/CD32 (Fc block)	BD Biosciences	Cat# 553142; RRID:AB_394657
Rat PE-Cy7 anti-CD44	BD Biosciences	Cat# 560569; RRID:AB_1727484
Rat APC anti-B220	BD Biosciences	Cat# 553087; RRID:AB_394617
Rat PE-Cy7 anti B220	BD Biosciences	Cat# 552772; RRID:AB_394458
Rat BV786 anti-B220	BD Biosciences	Cat# 563894; RRID:AB_2738472
Hamster PE-Cy7 anti-FAS	BD Biosciences	Cat# 557653; RRID:AB_396768
Rat BV395 anti-CD38	BD Biosciences	Cat# 740245; RRID:AB_2739992
Rat PE-Cy7 anti-CD86	BD Biosciences	Cat# 560582; RRID:AB_1727518
Rat BV421 anti-CD86	BD Biosciences	Cat# 564198; RRID:AB_2738663
Rat biotin anti-CXCR4	BD Biosciences	Cat# 551968; RRID:AB_394307
Rat biotin anti-CXCR5	BD Biosciences	Cat# 551960; RRID:AB_394301
Rat BV421 anti-IgD	BD Biosciences	Cat# 744291; RRID:AB_2742121
Rat BV510 anti-IgD	BD Biosciences	Cat# 563110; RRID:AB_2737003
Rat PE anti-IgG1	BD Biosciences	Cat# 550083; RRID:AB_393553
Rat BV421 anti-IgG1	BD Biosciences	Cat# 562580; RRID:AB_2737664
Rat BUV737 anti-CD138	BD Biosciences	Cat# 564430; RRID:AB_2738805
Rat FITC anti-IgM	BD Biosciences	Cat# 553437; RRID:AB_394857
Rat BV711 anti-IgM	BD Biosciences	Cat# 743327; RRID:AB_2741428
Rat BV421 anti-CCR6	BD Biosciences	Cat# 564736; RRID:AB_2738926
Rat APC anti-CD117	BD Biosciences	Cat# 561074; RRID:AB_10563203
Rat FITC anti-CD19	BD Biosciences	Cat# 553785; RRID:AB_395049
Rat PE-Cy7 anti-CD25	BD Biosciences	Cat# 561780; RRID:AB_10893596
Rat FITC anti-GL7	BD Biosciences	Cat# 553666; RRID:AB_394981
Rat AF647 anti-GL7	BD Biosciences	Cat# 561529; RRID:AB_10716056
Rat anti-CD138	BD Biosciences	Cat# 553712; RRID:AB_394998
Biotin-conjugated anti-B220	BD Biosciences	Cat# 550286; RRID:AB_393581
Human TruStain FcX (Fc block)	BioLegend	Cat# 422301; RRID:AB_2818986
Rat BV510 anti-CD62L	BioLegend	Cat# 104441; RRID:AB_2561537
Rat PE anti-PCNA	BioLegend	Cat# 307908; RRID:AB_314698
Rat APC-Cy7 anti-CD4	BioLegend	Cat# 100414; RRID:AB_312699
Mouse PerCP-Cy5.5 anti-CD45.2	BioLegend	Cat# 109828; RRID:AB_893350
Armenian Hamster BV421 anti-CD80	BioLegend	Cat# 104725; RRID:AB_10900989
Rat APC anti-CD3	BioLegend	Cat# 100235; RRID:AB_2561455
Mouse PE anti-BCL6	BioLegend	Cat# 648304; RRID:AB_2561375
Rat AF647 anti-BLIMP1	BioLegend	Cat# 150004; RRID:AB_2565618
Rat BV421 anti-B220	BioLegend	Cat# 103240; RRID:AB_11203896
Rat APC-Cy7 anti-B220	BioLegend	Cat# 103224; RRID:AB_313007
Rat PE anti-B220	BioLegend	Cat# 103208; RRID:AB_312993
Rat APC-Cy7 anti-CD38	BioLegend	Cat# 102728; RRID:AB_2616968

(*Continued on next page*)

Continued

REAGENT or RESOURCE	SOURCE	IDENTIFIER
Rat PerCP-Cy5.5 anti-GL7	BioLegend	Cat# 144610; RRID:AB_2562979
Mouse PerCP-Cy5.5 anti-FAS	BioLegend	Cat# 152610; RRID:AB_2632905
Rat PE-Cy7 anti-CD138	BioLegend	Cat# 142514; RRID:AB_2562198
Rat BV421 anti-CD138	BioLegend	Cat# 142508; RRID:AB_11203544
Rat APC anti-IL9	BioLegend	Cat# RM9A4; RRID:AB_11218680
Rat anti-mS1P1	R&D Systems	Cat# MAB7089; RRID:AB_10994183
Goat biotin anti-EFNB1	R&D Systems	Cat# BAF473; RRID:AB_2293418
Goat anti-Chicken IgY (H+L) Secondary Antibody, HRP	ThermoFisher Scientific	Cat# A16054; RRID:AB_2534727
Goat anti-Mouse IgG Alexa Fluor 647	ThermoFisher Scientific	Cat# A21235; RRID:AB_2535804
Mouse anti-AID	ThermoFisher Scientific	Cat# 1AID-2E11; RRID:AB_2633326
Mouse anti-CD38	ThermoFisher Scientific	Cat# MA5-14413; RRID:AB_10986743
Rabbit anti-NCOR2	ThermoFisher Scientific	Cat# PA1-843; RRID:AB_2149135
Armenian hamster anti-mouse CD40L (clone MR-1)	BioXCell	Cat# BE0017; RRID:AB_1107601
Polyclonal Armenian hamster IgG	BioXCell	Cat# BE0091; RRID:AB_1107773
Mouse anti-IL9 (clone 9C1)	BioXCell	Cat# BE0181; RRID:AB_10950648
Mouse IgG2a isotype control	BioXCell	Cat# BE0085; RRID:AB_1107771
Rabbit Anti-Mouse IgG H&L	Abcam	Cat# ab46540; RRID:AB_2614925
Rabbit anti-CD3	Abcam	Cat# ab16669; RRID:AB_443425
Rabbit anti-KI67	Cell Signaling Technology	Cat# 12202; RRID:AB_2620142
Rabbit anti-BCL6	Santa Cruz Biotechnology	Cat# sc-858; RRID:AB_2063450
Mouse anti-BCL6	Santa Cruz Biotechnology	Cat# sc-7388; RRID:AB_2063455
Rabbit anti-HDAC3	Santa Cruz Biotechnology	Cat# sc-11417; RRID:AB_2118706
Rabbit anti-HDAC3	Santa Cruz Biotechnology	Cat# sc-376957; RRID:AB_2715509
Mouse anti-β-Actin	Santa Cruz Biotechnology	Cat# sc-47778; RRID:AB_2714189
Rabbit anti-NCOR2	Sigma-Aldrich	Cat# 06-891; RRID:AB_310286
Rabbit anti-BACH2	Aviva Systems Biology	Cat# ARP39513_P050; RRID:AB_2045059
Mouse anti-TBL1XR1	Abnova	Cat# H00079718-M01; RRID:AB_490081
Chicken anti-BirA	BioFront Technologies	Cat# BID-CP-100
Biotinylated goat anti-rat secondary antibody	Jackson ImmunoResearch Lab.	Cat# 112-065-167; RRID:AB_2338179
Peroxidase IgG Fraction Monoclonal Mouse Anti-Rabbit IgG, light chain specific	Jackson ImmunoResearch Lab.	Cat# 211-032-171; RRID:AB_2339149
Peroxidase AffiniPure Goat Anti-Mouse IgG, light chain specific	Jackson ImmunoResearch Lab.	Cat# 115-035-174; RRID:AB_2338512
Anti-Human CD10-156Gd	Fluidigm	Clone HI10a; RRID:AB_2802107
Anti-Human CD27-167Er	Fluidigm	Clone L128; RRID:AB_2811093
Anti-Human CD38-172Yb	Fluidigm	Clone HIT2
Anti-Human CD44-171Yb	Fluidigm	Clone IM7
Bacterial and Virus Strains		
TOP10 Chemically Competent *E. coli*	ThermoFisher Scientific	Cat# C404010
Stbl3 Chemically Competent *E. coli*	ThermoFisher Scientific	Cat# C737303
DH5α Competent Cells	ThermoFisher Scientific	Cat# 18265017
Biological Samples		
Sheep red blood cells	Cocalico Biologicals	Cat# 20-1334A
Tissue microarrays of 341 primary diagnosed DLBCL	Ennishi et al., 2017; Scott et al., 2015	N/A

(*Continued on next page*)

Continued

REAGENT or RESOURCE	SOURCE	IDENTIFIER
Chemicals, Peptides, and Recombinant Proteins		
PE-Cy7 streptavidin	eBioscience ThermoFisher Scientific	Cat# 25-4317
APC streptavidin	BioLegend	Cat# 405207
APC-Cy7 streptavidin	BioLegend	Cat# 405208
NIP-haptenated FITC	Anderson et al., 2007	N/A
PE NP	Biosearch Technologies	Cat# N-5070
NP-OVAL	Biosearch Technologies	Cat# N-5051
NP-CGG	Biosearch Technologies	Cat# N-5055C
NP-KLH	Biosearch Technologies	Cat# N-5060
Alum adjuvant	ThermoFisher Scientific	Cat# 77161
Protein A Dynabeads	ThermoFisher Scientific	Cat# 10001D
V5-Tag magnetic beads	MBL International Corporation	Cat# M16711
Ovalbumin	Sigma-Aldrich	Cat# A5503
Recombinant mouse IL-9	Peprotech	Cat# 219-19
Recombinant mouse IL-4	R&D Systems	Cat# 404-ML
Recombinant mouse IL-21	R&D Systems	Cat# 594-ML
Ghost Dye Violet 510	Tonbo Biosciences	Cat# 13-0870
DAPI	ThermoFisher Scientific	Cat# D1306
NP-BSA, ratio 1-4	Biosearch Technologies	Cat# N-5050XL
NP-BSA, ratio > 20	Biosearch Technologies	Cat# N-5050H
Mitomycin C	Sigma-Aldrich	Cat# MO503
Alt-R® S.p. Cas9 Nuclease V3	Integrated DNA Technologies	Cat# 1081058
Alt-R® CRISPR-Cas9 tracrRNA	Integrated DNA Technologies	Cat# 1075927
Biotin	Sigma-Aldrich	Cat# B4501
Benzonase nuclease	Sigma-Aldrich	Cat# E1014-5KU
Sepharose beads	GE Healthcare Life Sciences	Cat# GE17-5113-01
TPCK trypsin	Promega	Cat# V5111
Biotinylated Peanut Agglutinin (PNA)	Vector Laboratories	Cat# B1075
EdU (5-ethynyl-2′-deoxyuridine)	ThermoFisher Scientific	Cat# E10187
Critical Commercial Assays		
Click-iT Plus AF488 Flow Cytometry Assay Kit	ThermoFisher Scientific	Cat# C10633
Cell Proliferation Dye eFluor 670	eBioscience ThermoFisher Scientific	Cat# 65-0840-85
CellTrace CFSE Cell Proliferation Kit	ThermoFisher Scientific	Cat# C34554
Foxp3/Transcription Factor Staining Buffer Set	ThermoFisher Scientific	Cat# 00-5523-00
AnnexinV binding buffer	BD Biosciences	Cat# 556454
PE-conjugated AnnexinV	BD Biosciences	Cat# 556421
Cell Proliferation Dye eFluor 670	ThermoFisher Scientific	Cat# 65-0840-85
EasySep Mouse B Cell Isolation Kit	StemCell Technologies	Cat# 9854
CD43 (Ly-48) MicroBeads	Miltenyi Biotec	Cat# 130-049-801
CD45R (B220) MicroBeads	Miltenyi Biotec	Cat# 130-049-501
SBA Clonotyping System	Southern Biotechnology	Cat# 5300-05
Nuclear Complex Co-IP Kit	Active Motif	Cat# 54001
QuickExtract DNA Extraction Solution	Epicenter	Cat# QE09050
Puregene Gentra cell kit	QIAGEN	Cat# 158388
DirectPCR Lysis Reagent	Viagen Biotech	Cat# 101-T
Red blood cell lysis solution	QIAGEN	Cat# 158904

(*Continued on next page*)

Continued

REAGENT or RESOURCE	SOURCE	IDENTIFIER
QuikChange II XL Site-directed mutagenesis kit	Agilent Technologies	Cat# 200521
Gateway LR Clonase II Enzyme mix	ThermoFisher Scientific	Cat# 11791020
PEG-it	System Biosciences	Cat# LV810A-1
TOPO TA Cloning Kit for Sequencing	ThermoFisher Scientific	Cat# K457501
Zero Blunt TOPO PCR Cloning Kit	ThermoFisher Scientific	Cat# K280002
SF Cell Line 4D-Nucleofector X Kit	Lonza	Cat# PBC2-22500
Sepharose beads	GE Healthcare Life Sciences	Cat# GE17-5113-01
Illumina TruSeq stranded-mRNA Library Prep	Illumina	Cat# 20020594
Quant-iT dsDNA HS Assay	ThermoFisher Scientific	Cat# Q33120
SYBR Safe DNA stain	ThermoFisher Scientific	Cat# S33102
Verso cDNA Synthesis kit	ThermoFisher Scientific	Cat# AB1453B
Fast SYBR Green Master Mix	ThermoFisher Scientific	Cat# 4385614
Vector® Blue Alkaline Phosphatase (Blue AP) Substrate Kit	Vector Laboratories	Cat# SK-5300
DAB Peroxidase (HRP) Substrate Kit	Vector Laboratories	Cat# SK-4100
Deposited Data		
DLBCL cases	Arthur et al., 2018; Ma et al., 2019; Reddy et al., 2017; Schmitz et al., 2018	N/A
FL cases	Krysiak et al., 2017; Ma et al., 2019; Ortega-Molina et al., 2015	N/A
Raw sequencing data	This manuscript	GEO: GSE139059
Mass spectrometry data	This manuscript	MassIVE: MSV000085310
Experimental Models: Cell Lines		
Human: OCI-Ly1 cells	Ontario Cancer Institute (OCI)	CVCL_1879
Human: U2932 cells	DSMZ-German Collection of Microorganisms and Cell Cultures	RRID:CVCL_1896
Human: HEK293T cells	American Type Culture Collection (ATCC)	RRID:CVCL_0063
Mouse: 40LB	Nojima et al., 2011	N/A
Experimental Models: Organisms/Strains		
Mouse: C57BL/6J	The Jackson Laboratory	Stock# 000664
Mouse: *Cγ1-Cre* (B6.129P2(Cg)-Ighg1tm1$^{(cre)Cgn}$/J)	The Jackson Laboratory	Stock# 010611
Mouse *CD19-Cre* (B6.129P2(C)-Cd19$^{tm1(cre)Cgn}$/J)	The Jackson Laboratory	Stock# 006785
Mouse: μMT (B6.129S2-Ighm^{tm1Cgn}/J)	The Jackson Laboratory	Stock# 002288
Mouse: CD45.1 (B6.SJL-Ptprc^{a}Pepc^{b}/Boy)	The Jackson Laboratory	Stock# 002014
Mouse: Rosa26-lox-stop-lox-YFP (B6.129X1-Gt(ROSA)26Sor$^{tm1(EYFP)Cos}$/J)	The Jackson Laboratory	Stock# 006148
Mouse: OT-II (B6.Cg-Tg(TcraTcrb) 425Cbn/J)	The Jackson Laboratory	Stock# 004194
Mouse: R26:FLPe (129S4/SvJaeSor-Gt(ROSA)26Sor$^{tm1(FLP1)Dym}$/J)	The Jackson Laboratory	Stock# 003946
Mouse: B1-8hi (B6.129P2-Ptrpc^{a} Igh^{tm1Mnz}/J)	The Jackson Laboratory	Stock# 007594
Mouse: *R26-Fucci2aR*	(Mort et al., 2014)	N/A
Mouse: *IμBCL6*	(Cattoretti et al., 2005)	N/A
Mouse: *VavP-Bcl2*	(Ogilvy et al., 1999)	N/A
Mouse: *Aicda*-KO	(Muramatsu et al., 2000)	N/A

(*Continued on next page*)

Continued

REAGENT or RESOURCE	SOURCE	IDENTIFIER
Mouse: *Tbl1xr1-D370Y*	This manuscript	N/A
Mouse: *Tbl1xr1-KO*	This manuscript	N/A
Oligonucleotides		
*TBL1XR1*_1 crRNA (Hs.Cas9.TBL1XR1.1.AG): 5′-GAUAUGGCUUUCUAUAC CAAGUUUUAGAGCUAUGCU-3′	Integrated DNA Technologies	N/A
*TBL1XR1*_2 crRNA ((Hs.Cas9.TBL1XR1.1.AA): 5′-UAUUGGUCGACCAUCAAACAG UUUUAGAGCUAUGCU-3′	Integrated DNA Technologies	N/A
Tbl1xr1-D370Y genotyping Fwd: 5′-AACGAGAAGCCAAGGTTCCAGTTC-3′	This manuscript	N/A
Tbl1xr1-D370Y genotyping Rev: 5′-GATGCAAAGGTGTTGTTGCTCTGC-3′	This manuscript	N/A
Tbl1xr1-KO genotyping Fwd: 5′-TATCCTCAGCGGTGGGTTAC-3′	This manuscript	N/A
Tbl1xr1-KO genotyping Rev: 5′-GCCAGTAGGGGTTGCTGATA-3′	This manuscript	N/A
PIM1 sequencing Fwd: 5′-TTCGGCTCGGTCTACTCTG-3′	Liu et al., 2008	N/A
PIM1 sequencing Rev: 5′-GGAGGGAAAAGTGGGTCATAC-3′	Liu et al., 2008	N/A
Mouse V_H sequencing Fwd: 5′-GGAATTCGCCTGACATCTGA GGACTCTGC-3′	Jolly et al., 1997	N/A
Mouse V_H sequencing Rev: 5′-GACTAGTCCTCTCCAGTT TCGGCTGAATCC-3′	Jolly et al., 1997	N/A
Primers used for RT-qPCR, see Table S6	This manuscript	N/A
Recombinant DNA		
Plasmid: pSBtet-GP	Kowarz et al., 2015	Addgene plasmid #60495
Plasmid: pCMV(CAT)T7-SB100	Mátés et al., 2009	Addgene plasmid #34879
Plasmid: pLIX_403	David Root Lab (Broad Institute, Cambridge, MA, USA); unpublished.	Addgene plasmid #41395
Plasmid: pCMV-VSV-G	Stewart et al., 2003	Addgene plasmid #8454
Plasmid: pCMV-dR8.91	Life Science Market	Cat# PVT2323
Software and Algorithms		
FlowJo	Becton Dickinson	Version 10.5.3
GraphPad Prism	GraphPad Software	Version 6.00
Aperio eSlide Manager	Leica Biosystems	https://www.leicabiosystems.com/aperio-eslide-manager/
GSEA v2.0.13	Broad Institute	https://software.broadinstitute.org/cancer/software/gsea
CASAVA	Ilumina	Version 1.8.2
Fiji (ImageJ)	Schindelin et al., 2012; Schneider et al., 2012	https://imagej.net/Fiji
EdgeR	Robinson et al., 2010	https://bioconductor.org/packages/release/bioc/html/edgeR.html
Proteowizard	Craig and Beavis, 2004	http://proteowizard.sourceforge.net/
X!Tandem	Kessner et al., 2008	https://www.thegpm.org/TANDEM/

(*Continued on next page*)

Continued

REAGENT or RESOURCE	SOURCE	IDENTIFIER
ProHits	Liu et al., 2010	http://prohitsms.com/Prohits_download/list.php
SAINT Express	Choi et al., 2011	http://saint-apms.sourceforge.net
CRAPome Database	Mellacheruvu et al., 2013	v1.1 for Jurkart cells
STAR transcriptome aligner v2.5.1b	Dobin et al., 2013	https://code.google.com/archive/p/rna-star
Biopython	Cock et al., 2009	https://github.com/biopython
sangerseqR	Hill et al., 2014	Version 1.22.0
PAGE algorithm	Goodarzi et al., 2009	https://github.com/goodarzilab/PAGE
VarScan	Koboldt et al., 2012	Version 2.3.6
Strelka	Saunders et al., 2012	Version 1.0.13
MuTect	Cibulskis et al., 2013	Version 1.1.4
SnpEff	Cingolani et al., 2012	Version 4.2
Biostrings	Pagès et al., 2019	Version 2.54.0
Other		
Graphical Abstract Cartoons	SERVIER Medical Art Repository	https://smart.servier.com

RESOURCE AVAILABILITY

Lead Contact

Further information and requests for resources and reagents should be directed to and will be fulfilled by the Lead Contact, Ari M. Melnick (amm2014@med.cornell.edu).

Materials Availability

Unique reagents generated in this study are available from the Lead Contact with a completed Materials Transfer Agreement.

Data and Code Availability

The accession number for all RNA sequencing data reported in this paper is Gene Expression Omnibus (GEO): GSE139059. The accession number for all raw mass spectrometry data reported in this paper is MassIVE archive (https://massive.ucsd.edu/ProteoSAFe/static/massive.jsp): MSV000085310. Code used for analysis is available upon request.

EXPERIMENTAL MODEL AND SUBJECT DETAILS

Mouse models

Animal care was in strict compliance with institutional guidelines established by the Weill Cornell Medical College, the Guide for the Care and Use of Laboratory Animals (National Research Council US Institute for Laboratory Animal Research, 1996), and the Association for Assessment and Accreditation of Laboratory Animal Care International. The Research Animal Resource Center of the Weill Cornell Medical College of Medicine approved all mouse procedures.

The following strains were obtained from The Jackson Laboratory (Ben Harbor, ME, USA): C57BL/6J (CD45.2, stock 000664), Cγ1-Cre (stock 010611), CD19-Cre (stock 006785), μMT (stock 002288), B6.SJL-PtprcaPepcb/Boy (CD45.1, stock 002014), Rosa26-lox-stop-lox-YFP (stock 006148), OT-II (stock 004194; (Barnden et al., 1998)), R26:FLPe knock in strain (stock 003946) and B1-8hi (stock 007594). The R26-Fucci2aR model (Mort et al., 2014) was developed by I.J. Jackson (University of Edinburgh, Scotland). *IμBcl6* mice (Cattoretti et al., 2005) were obtained from R. Dalla-Favera (Columbia University, NY, USA). The *VavP-Bcl2* (Ogilvy et al., 1999) model was developed by J.M. Adams (Walter and Eliza Hall Institute of Medical Research, Australia). The *Aicda*-KO mouse model (Muramatsu et al., 2000) was a generous gift from T. Honjo (Kyoto University Graduate School of Medicine, Kyoto, Japan).

Conditional *Tbl1xr1*-D370Y mice were generated by inGenious Targeting Laboratory Inc. (Ronkonkoma, NY, USA), using an inversion and deletion approach (Figure S1A). To achieve the conditional activation of the D370Y mutation, WT LoxP and mutant Lox66/Lox71 (RE/LE mutants) sites were used. In brief, the genomic sequence from *Tbl1xr1* exon 11 to exon 12, and their flanking sequences, were duplicated and flanked by Lox66 and Lox71 sites. The specific point mutation GAC > TAC (D > Y) was introduced into the duplicated exon 12. Then, the Lox66/71 flanked sequence was inserted into intron 12, in the reverse direction. A 5′ WT LoxP site was inserted upstream of exon 11. An FRT-flanked Neomycin selection cassette was inserted immediately upstream of the Lox66/71 flanked inversion sequence. Embryonic stem (ES) cells were electroporated with this homologous targeting construct,

and stable G418 clones were derived. Targeted iTL IC1 (C57BL/6) ES cells were microinjected into BALB/c blastocysts. Resulting chimeras with a high percentage of black coat were further screened by PCR, and mated to C57BL/6J R26:FLPe mice, to remove the Neomycin cassette. Founder mice were further backcrossed for at least 10 generations into the C57BL/6J background.

Conditional *Tbl1xr1*-KO mice were obtained by microinjection of targeted JMB8A3.N1 *Tbl1xr1*$^{tm1a(EUCOMM)Hmgu}$ ES cells (clone HEPD0744_3_E01; EUCOMM program) into C57BL/6-albino blastocytes, and implantation into pseudo-pregnant foster C57BL/6-albino recipients (stock 000058; The Jackson Laboratory). Procedures were carried out by the Mouse Genetic - Transgenic Core Facility at Memorial Sloan Kettering Cancer Center (MSKCC, New York, NY, USA). Resulting chimeras with a high percentage of black coat were further screened by PCR, and mated to C57BL/6J R26:FLPe mice, to remove the FRT-flanked lacZ-Neomycin^{resistance} cassette. Founder mice were further backcrossed for at least 10 generations into the C57BL/6J background.

All mouse experiments were conducted using aged and sex-matched specimens. Experiments were designed to include male and female specimens in all groups, and no sex-based influence/bias was detected in the observations made in this work. Unless stated otherwise in the text, all animals were 8 to 12 weeks of age at the time of experimentation.

Cell lines

The DLBCL cell line OCI-Ly1 (CVCL_1879; male origin) was grown in Iscove Modified Dulbecco Media (12440061; ThermoFisher Scientific), supplemented with 10% FBS and penicillin G/streptomycin; U2932 (CVCL_1896; female origin) cells were grown in Roswell Park Memorial Institute medium (10-040-CV; Corning; Corning, NY, USA), supplemented with 10% FBS, penicillin G/streptomycin, L-glutamine, and HEPES; HEK293T cells (CVCL_0063; female origin) were maintained in Dulbecco's Modified Eagle Medium (11965-092; ThermoFisher Scientific), supplemented with 10% FBS and penicillin G/streptomycin. Murine 40LB cells (Nojima et al., 2011) (male origin) were grown in DMEM media with 10% FBS. All cells were grown in incubators at 37C, in a 5% CO_2 atmosphere. Cell line authentication testing was performed at IDEXX BioResearch (https://www.idexxbioresearch.com/cellcheck), using methods recommended by the American National Standards Institute (ANSI ASN-0002-2011). The cell lines were confirmed to be of human origin and tested for evidence of cross-species contamination (mouse, rat, Chinese hamster and African Green monkey). Short tandem repeat (STR) testing was performed and the genetic profile obtained was compared to the established cell line profile to confirm the cell lines are consistent with the established profile. These cell lines were also routinely tested for Mycoplasma contamination in the laboratory.

Bacteria strains

TOP10, Stbl3 and DH5α *E. Coli* cells (ThermoFisher Scientific) were cultured in autoclave-sterilized Luria Bertani broth (BP1426-2; Fisher Scientific), in a MaxQ 8000 orbital shaker (ThermoFisher Scientific) set at 200rpm and 37°C.

Human subjects

Information on *TBL1XR1* mutation status in human lymphoma specimens was retrieved from publicly available datasets. DLBCL cases (Arthur et al., 2018; Ma et al., 2019; Reddy et al., 2017; Schmitz et al., 2018); FL cases: (Krysiak et al., 2017; Ma et al., 2019; Ortega-Molina et al., 2015). Clinic-pathological characteristics of these cases are detailed in the original publications. Further information on *TBL1XR1* mutation status is summarized in Table S1.

All DLBCL human samples used for immunoprofiling studies were obtained with informed consent, and according to protocols approved by the BCCA Research Ethics Board. CD38 IHC on human specimens was performed on formalin-fixed paraffin-embedded tissue (FFPE) biopsies of 341 DLBCL (Arthur et al., 2018). Clinic-pathological characteristics of these cases are detailed in the original publication. For CyTOF immunoprofiling, diagnostic pre-treatment LN biopsies from patients with DLBCL, or non-malignant "reactive" LN (rLN) were acquired from the lymphoma tumor bank at the BC Cancer Agency (as described in Nissen et al., 2019), and were selected based on sufficient numbers of viable cells for CyTOF analysis (2 million per sample). Clinic-pathological characteristics of these cases are detailed in the original publication. Further details on somatic mutations in these cases are summarized in Table S5.

METHOD DETAILS

Germinal center assessment in mice

To induce GC formation, age- and sex-matched mice were immunized intraperitoneally at 8 to 12 weeks of age with either 0.5ml of a 2% sheep SRBC suspension in PBS (Cocalico Biologicals; Reamstown, PA, USA), or 100 μg of the highly substituted hapten NP (NP_{16} to NP_{32}) conjugated to the carrier protein ovalbumin (OVA), or CGG (Chicken Gamma Globulin), or KLH (Keyhole Limpet Hemocyanin; all from Biosearch Technologies; Novato, CA, USA) absorbed to Imject Alum Adjuvant (77161; ThermoFisher Scientific; Waltham, MA, USA) at a 1:1 ratio. In the experiments where T_{FH} interactions were blocked *in vivo*, mice received and i.v. injection of 100μg anti-CD40L antibody (clone MR-1, BE0017; BioXCell; West Lebanon, NH, USA) or control IgG antibody (BE0091; BioXCell) 4 days after SRBC immunization, and a second dose of antibody 2 days later. In the experiments where IL-9 was blocked *in vivo*, mice received a single i.v. injection of 200μg anti-IL-9 antibody (clone 9C1, BE0181; BioXCell) or control IgG2a antibody (BE0085;

BioXCell) 7 days after SRBC immunization. In these experiments, littermates of the same sex were randomly assigned to experimental groups. In experiments where GC cell cycle distribution was assessed, animals received an i.v. injection of 1mg EdU (E10187; ThermoFisher Scientific), 1h before euthanasia.

BM transplantations and lymphomagenesis studies

Bone marrow cells were harvested from the tibia and femur of 8-12 weeks old donor mice. After treatment with red blood cell lysis solution (158904; QIAGEN; Germantown, MD, USA), cells were mixed at the indicated ratios, and 1-2 million cells were injected into the tail vein of lethally irradiated C57BL/6J host mice (2 doses of 450rad, on a Rad Source Technologies RS 2000 Biological Research X-ray Irradiator). Transplanted mice were used for experiments 6-8 weeks after transplant, to allow for full engraftment. With the exception of mice euthanized at specific time points, all mice involved in lymphomagenesis studies were monitored until any one of several criteria for euthanizing were met, including severe lethargy, more than 10% body weight loss, and palpable splenomegaly that extended across the midline, in accordance with our Weill Cornell Medicine Institutional Animal Care and Use Committee–approved animal protocol (protocol #2011-0031).

NB and MB adoptive transfers

For NB cell adoptive transfers, total splenocytes were harvested from 8-12 weeks old B1-8hi donor mice (*Cd45.1* or Cd45*.1/2*), and mature B cells were isolated using negative selection with CD43 magnetic beads (130-049-801; Miltenyi Biotec; Somerville, MA, USA). The percentage of NP-binding cells in this population was determined by FC (see below), and a number of mature B cells corresponding to 2-3x10^5 NP-binding B cells was injected i.v. into C57BL/6J recipient mice (*Cd45.2*). Recipient animals were immunized with an NP-conjugate 16h after cell transfer, and euthanized for analysis at the stated time points.

Antigen-specific MB cells for transfer experiments were generated following the protocol above, and splenic NP-binding MB cells were FACS-sorted three months, or more, after immunization of recipient mice with NP-CGG or NP-KLH. Splenic memory T cells (MT; CD3+CD4+CD44+CD62L-) were FACS-sorted from OT-II mice, 10 days after immunization with 100μg OVA peptide (#A5503, Sigma-Aldrich; San Luis, MO, USA). For re-call experiments, 8x10^3 MB and 4x10^4 MT cells were injected i.v. into μMT recipient mice (*Cd45.2*). Recipient animals were immunized with NP-OVA 16h after transfer, and euthanized for analysis 3.5 days after immunization.

Flow cytometry analysis and cell sorting

Single-cell suspensions from mouse spleens or bone marrow were stained using the following fluorescent-labeled anti-mouse antibodies: from eBioscience ThermoFisher Scientific: APC anti-CD38 (17-0381, dilution 1:500), PE anti-CXCR4 (12-9991, dilution 1:400), PerCP-Cy5.5 anti-CD45.1 (45-0453, dilution 1:500), FITC anti-PD-1 (11-9985, dilution 1:200), PE-Cy7 streptavidin (25-4317, dilution 1:1000); from BD Biosciences (San Jose, CA, USA): PE-Cy7 anti-CD44 (560569, dilution 1:500), APC, PE-Cy7 and BV786 anti-B220 (553087, 552772 and 563894, dilution 1:500), PE-Cy7 anti-FAS (557653, dilution 1:500), BV395 anti-CD38 (740245, dilution 1:500), PE-Cy7 and BV421 anti-CD86 (560582 and 564198, dilution 1:300), biotin anti-CXCR4 (551968, dilution 1:200), biotin anti-CXCR5 (551960, dilution 1:200), BV421 and BV510 anti-IgD (744291 and 563110, dilution 1:500), PE and BV421 anti-IgG1 (550083 and 562580, dilution 1:500), BUV737 anti-CD138 (564430, dilution 1:500), FITC and BV711 anti-IgM (553437 and 743327, dilution 1:500), BV421 anti-CCR6 (564736, dilution 1:500), APC anti-CD117 (561074, dilution 1:500), FITC anti-CD19 (553785, dilution 1:500), PE-Cy7 anti-CD25 (561780, dilution 1:500), FITC and AF647 anti-GL7 (553666 and 561529, dilution 1:500); from BioLegend (San Diego, CA, USA): BV510 anti-CD62L (104441, dilution 1:500), PE anti-PCNA (307908, dilution 1:50), APC-Cy7 anti-CD4 (100414, dilution 1:500), PE anti-PD-L2 (107206, dilution 1:300), PerCP-Cy5.5 anti-CD45.2 (109828, dilution 1:500) BV421 anti-CD80 (104725, dilution 1:200) APC anti-CD3 (100235, dilution 1:500), PE anti-BCL6 (648304, dilution 1:500), AF647 anti-BLIMP1 (150004, dilution 1:300), BV421, APC-Cy7 and PE anti-B220 (103240, 103224 and 103208, dilution 1:500), APC-Cy7 anti-CD38 (102728, dilution 1:500), PerCP-Cy5.5 anti-GL7 (144610, dilution 1:500), PerCP-Cy5.5 anti-FAS (152610, dilution 1:500), PE-Cy7 and BV421 anti-CD138 (142514 and 142508, dilution 1:500), APC streptavidin (405207, dilution 1:1000), APC-Cy7 streptavidin (405208, dilution 1:1000); from R&D Systems (Minneapolis, MN, USA): biotin anti-EFNB1 (BAF473, dilution 1:60) and anti-mS1P1 (MAB7089, dilution 1:50); from Biosearch Technologies: PE NP (N-5070-1, dilution 1:500); from Life Technologies: anti-AID (1AID-2E11; dilution 1:100). NIP-haptenated FITC was obtained from M.J. Shlomchik (University of Pittsburg, PA, USA) (Anderson et al., 2007). For S1PR1 staining, a biotinylated goat anti-rat secondary antibody was used (112-065-167; dilution 1:1000, Jackson Immunoresearch; West Grove, PA, USA). For AID staining, a goat anti-mouse IgG cross-adsorbed secondary antibody conjugated to Alexa Fluor 647, was used (A21235, dilution 1:300; Thermo Scientific). To detect surface IL-9R expression, cells were incubated with 8 ng/μl recombinant IL-9 (219-19; Peprotech, Rocky Hill, NJ) on ice for 60min, washed and fixed in 1% paraformaldehyde for 30min, and then stained with APC anti-IL-9 (RM9A4, dilution 1:250; BioLegend) on ice. As the negative control, incubation with IL-9 was omitted. Ghost Dye Violet 510 (13-0870; Tonbo Biosciences; San Diego, CA, USA) or DAPI (D1306; ThermoFisher Scientific) were used for the exclusion of dead cells. For intracellular markers, cells were fixed and permeabilized with the eBioscience Foxp3/Transcription Factor Staining Buffer Set (00-5523-00; ThermoFisher Scientific). PE-conjugated AnnexinV (556421, dilution 1:100; BD Biosciences) in AnnexinV binding buffer (BD Biosciences) was used to identify apoptotic cells. For cell cycle assessment, EdU incorporation was detected using the Click-iT Plus AF488 Flow Cytometry Assay Kit (C10633; ThermoFisher Scientific). Proliferation rates were assessed in cell lines using the CellTrace CFSE Cell Proliferation Kit (C34554; ThermoFisher Scientific), and in primary cultures

using the eBioscience Cell Proliferation Dye eFluor 670 (65-0840-85; ThermoFisher Scientific), according to the vendor's protocol. Data were acquired on BD FACS Canto II or BD Fortessa flow cytometer analyzers, and analyzed using FlowJo software package (TreeStar).

When B cell populations were sorted, single-cell suspensions of splenocytes were pre-enriched in B cells using positive selection with anti-B220 magnetic microbeads (130-049-501; Miltenyi Biotec), or negative selection with the EasySep Mouse B Cell Isolation Kit (19854; StemCell Technologies,). The stated populations were then isolated using a BD FACSAria II or a BD Influx sorter (BD Biosciences).

ELISA

For analysis of T cell dependent antibody production, mice were immunized intraperitoneally with 100 μg NP-CGG or NP-OVA or NP-KLH, ratio 16-32, in alum (1:1). Serum from each animal was collected before immunization, and on the stated days after immunization. Titers of low and high-affinity isotype-specific antibodies to NP were measured in plates coated with NP_{28}-BSA or NP_8-BSA, respectively, using the SBA Clonotyping System (5300-05; Southern Biotechnology; Birmingham, AL, USA), according to the manufacturer's protocol. Results were assessed by spectrophotometric measurement of absorbance at 405nm using a Biotek Synergy Neo Alpha Plate Reader (BioTek; Winooski, VT, USA). Background readings of absorbance in negative control wells were $A_{450} < 0.050$.

Histology and immunohistochemistry

Mice organs were fixed in 4% formaldehyde and embedded in paraffin. Tissue processing and staining were done by the Laboratory of Comparative Pathology (MSKCC). Briefly, five micron-sections were deparaffinized and heat antigen-retrieved in citrate buffer pH = 6.4, and endogenous peroxidase (HRP) activity was blocked by treating the sections with 3% hydrogen peroxide in methanol. Indirect immunohistochemistry was performed with anti-species-specific biotinylated secondary antibodies followed by avidin–horseradish peroxidase or avidin-AP, and developed by Vector Blue or DAB color substrates (Vector Laboratories; Burlingame, CA USA). Sections were counterstained with hematoxylin. The following primary antibodies were used: biotin-conjugated anti-B220 (550286; BD Biosciences), anti-CD3 (ab16669; Abcam; Cambridge, UK), anti-PNA (B1075; Vector Laboratories), anti-CD138 (553712; BD Biosciences), and anti-KI67 (12202; Cell Signaling Technology; Danvers, MA, USA). TUNEL staining was carried out as previously described (Gavrieli et al., 1992). IHC on human specimens was performed on formalin-fixed paraffin-embedded tissue (FFPET) biopsies of 341 DLBCL cases within the cohort as described previously (Ennishi et al., 2017; Scott et al., 2015). Briefly, IHC staining on 4 μm slides of TMAs was performed for CD38 (SPC32; MA5-14413; ThermoFisher Scientific) on the Benchmark XT platform (Ventana, AZ, USA), according to the previously described method (Ennishi et al., 2017; Scott et al., 2015). Slides were scanned using a Zeiss Mirax Slide Scanner and photomicrographs were examined using Aperio eSlide Manager (Leica Biosystems; Wetzlar, Germany). Fiji software (Schindelin et al., 2012; Schneider et al., 2012) was used to quantify GC and $TUNEL^+$ cell/areas. CD38 staining was semiquantitatively assessed on tumor cells using HistoScore (HS = IxP): intensity (I = [1-3]) and percentage of positive cells (p = [0-100]). Specimens with HS > 50 were defined as CD38 positive.

3D B cell follicular organoid

Experiments using the organoid culture system were performed as previously described (Béguelin et al., 2017). In brief, splenic B cells were obtained from naive animals through negative selection, using the EasySep Mouse B Cell Isolation Kit in accordance with manufacturer's protocol. Feeder 40LB cells (Nojima et al., 2011) were grown in DMEM media with 10% FBS and, at the time of experiment, were mitotically inhibited through incubation in cell culture complete medium containing 0.01 mg/ml Mitomycin C (MO503, Sigma-Aldrich,) at 37 °C for 55 min before the encapsulation. For organoid fabrication, gelatin stock solution was freshly prepared by mixing gelatin powder (Sigma-Aldrich) in RPMI-1640 medium followed by sterilization using syringe filter. Cells were mixed with warmed 5% gelatin stock solution and diluted accordingly using cell culture medium. Silicate nanoparticles (SiNP) with 25–30 nm in diameter and 1 nm in thickness were obtained from Southern Clay Products Inc. (Gonzales, TX, USA). A 3% hydrogel SiNP suspension was freshly prepared before the encapsulation procedure by mixing SiNP powder with deionized water and vortexing the resulting solution, followed by filtration through 0.22μm syringe filters immediately before use. Organoids were fabricated in 96-well plates by first adding 10 μl of 3% hydrogel SiNP followed by injecting 10 μl cell-containing gelatin solution into the initial SiNP droplet, and then mixing the entire hydrogel through repeated pipetting. Each organoid contained 50,000 B cells and 80,000 40LB cells. Organoids were cured for ~10 min before the addition of RPMI media with 10% FBS and penicillin G/streptomycin, containing 50 ng/ml murine recombinant IL-4 (404-ML; R&D Systems) and 25ng/ml murine recombinant IL-21 (594-ML; R&D Systems) and were incubated at 37 °C with 5% CO2. Cell culture medium was renewed every 3 days.

Generation of TBL1XR1-KO cell lines

To generate *TBL1XR1*-KO clones using CRISPR, cell lines were electroporated using an Amaxa Nucleofector Unit and the SF Cell Line 4D-Nucleofector X Kit (PBC2-22500; Lonza; Basel, Switzerland), to incorporate a recombinant Cas9 nuclease (Alt-R® S.p. Cas9 Nuclease V3, 1081058), a *TBL1XR1*-targeting Alt-R® CRISPR-Cas9 crRNA (*TBL1XR1*_1 crRNA: 5′-GAU AUG GCU UUC UAU ACC AAG UUU UAG AGC UAU GCU-3′; *TBL1XR1*_2 crRNA: 5′-UAU UGG UCG ACC AUC AAA CAG UUU UAG AGC UAU GCU-3′), and an Alt-R® CRISPR-Cas9 tracrRNA (1075927; all from Integrated DNA Technologies; Coralville, IA, USA), following

vendor's recommendations. Forty-eight hours after electroporation, cells were single-cell plated into 96 well plates, and allowed to grow for at least 2 weeks. Resulting clones were screened by WB, and positive clones were further verified by Sanger sequencing of genomic DNA. Clones expressing parental-like levels of TBL1XR1, and WT DNA sequences, were used as congenic controls for experiments.

Generation of TBL1XR1 mutant cell lines

TBL1XR1 open reading frame (ORF) was amplified from HEK293T cells, and a Linker-His_Tag-V5_Tag sequence was added downstream by PCR (5′- GGCAGCAGCGGCCATCATCACCATCACCACGGTAAGCCTATCCCTAACCCTCTCCTCGGTCTCGATTCTACG -3′). The TBL1XR1-V5 insert was cloned into the pSBtet-GP backbone (#60495; Addgene; Watertown, MA, USA; (Kowarz et al., 2015) using the SfiI restriction enzyme (New England Biolabs; Ipswich, MA, USA). *TBL1XR1* point mutations (D370Y, Y395H and Y446S) were introduced using the QuikChange II XL Site-directed mutagenesis kit (200521; Agilent Technologies; Santa Clara, CA, USA), and verified by Sanger sequencing. OCI-Ly1 cells were nucleofected to incorporate the different pSBtet-GP-TBL1XR1-V5 plasmids, along with a construct coding for the SB100X transposase [pCMV(CAT)T7-SB110; #34879, Addgene] (Mátés et al., 2009). Cells were selected with Puromycin for 7 days, and incorporation of the construct was validated by FC for GFP. To induce TBL1XR1-V5 expression, cells were stimulated with Doxycycline (DOX) 1μg/ml for 48h in complete growth media.

Generation of cell lines for BioID experiments

TBL1XR1 or eGFP ORF were cloned into the pLIX_403 backbone (#41395; Addgene; David Root (Broad Institute, Cambridge, MA, USA), downstream of FLAG-BirA(R118G) ORF (#36047; Addgene) (Roux et al., 2012), using the Gateway LR Clonase II Enzyme mix (11791020; ThermoFisher Scientific). *TBL1XR1*-Y446S mutation was introduced using the QuikChange II Site-directed mutagenesis kit, and verified by Sanger sequencing. Lentivirus were produced in HEK293T cells co-transfected with pCMV-VSV-G and pCMV-dR8.91 plasmids, and then concentrated using PEG-it (LV810A-1; System Biosciences; Palo Alto, CA, USA). OCI-Ly1 and U2932 cells were infected and cultured for 48h, and then selected with Puromycin for 7 days. To induce expression of the FLAG-BirA-fusion proteins, cells were stimulated with DOX 1μg/ml for 24h. Incorporation of the construct was validated by WB for BirA (Figure S5C), or FC for eGFP.

BioID experiments

Expression of FLAG-BirA-fusion proteins in OCI-Ly1 and U2932 cells was induced by treatment with Doxycycline 1μg/ml for 24h, after which biotin 50μM (B4501; Sigma-Aldrich) was added to the media for additional 24h. Cell pellets were washed twice with PBS, and lysed in modified RIPA lysis buffer (50mM Tris-HCl pH = 7.5, 150mM NaCl, 1mM EDTA, 1mM EGTA, 1% Triton X-100, 0.1% SDS, 1:500 protease inhibitor cocktail (11873580001; Sigma-Aldrich), 1:100 Benzonase nuclease (E1014-5KU; Sigma-Aldrich), at 4°C for 1h, and sonicated for 30 s at 35% power to disrupt visible aggregates. Lysates were then centrifuged at 16,000rpm for 30min, and clarified supernatants were incubated with 30μL packed pre-equilibrated streptavidin-Sepharose beads (GE17-5113-01; GE Healthcare Life Sciences; Chicago, IL, USA) at 4°C for 3h. Beads were collected by centrifugation, washed six times with 50mM ammonium bicarbonate pH = 8.3, and treated with TPCK trypsin (V5111; Promega Corporation; Madison, WI, USA). The supernatant, containing tryptic peptides, was collected and lyophilized. Peptides were resuspended in 0.1% formic acid.

LC-MS/MS was conducted using a 120min reversed-phase buffer gradient running at 150nL/min (column heated to 40°C) on a Proxeon EASY-nLC pump in-line with a hybrid LTQ-Orbitrap Velos mass spectrometer (ThermoFisher Scientific). A parent ion scan was performed in the Orbitrap, using a resolving power of 60000. Simultaneously, up to twenty of the most intense peaks were selected for MS/MS (minimum ion count of 1000 for activation) using standard CID fragmentation. Fragment ions were detected in the LTQ. Dynamic exclusion was activated such that MS/MS of the same m/z (within a 10ppm window, exclusion list size 500) detected three times within 45 s were excluded from analysis for 30 s. For protein identification, Proteowizard was used to convertraw files to .mzXML, and searched using X!Tandem (Craig and Beavis, 2004; Kessner et al., 2008) against Human RefSeq Version 45. Search parameters specified a parent MS tolerance of 15ppm and an MS/MS fragment ion tolerance of 0.4Da, with up to two missed cleavages allowed for trypsin. Oxidation of methionine and ubiquitylation of lysine residues were allowed as variable modifications. Data were analyzed using a trans-proteomic pipeline via the ProHits software suite (Liu et al., 2010). Proteins identified with a ProteinProphet cut-off value 0.80 (corresponding to FDR < 1%) were analyzed with SAINT Express (Choi et al., 2011). Four control runs of Flag-BirA-eGFP were used for comparative purposes. The control runs were collapsed to the two highest spectral counts for each hit. Prey identified with $\geq$ 2 spectral counts in each of the two replicates with a SAINT $\geq$ 75% were considered significant. Known common contaminants (CRAPome Database v1.1 for Jurkart cells) (Mellacheruvu et al., 2013) were removed from the final protein lists. All raw mass spectrometry files have been deposited at the MassIVE archive (https://massive.ucsd.edu/ProteoSAFe/static/massive.jsp).

Cell lysis, immunoblotting and immunoprecipitation

Whole cell protein lysates from cell lines or GCB were obtained using a buffer containing Tris-HCl 50mM (pH = 7.4), NaCl 150mM, EDTA 1mM, EGTA 1mM, NP-40 1%, SDS 0.1%, glycerol 10%, and complete protease inhibitor cocktail. Protein extracts for IP experiments were obtained using the Nuclear Complex Co-IP Kit (54001; Active Motif; Carlsbad, CA, USA). For IP experiments, 500-1000ug of nuclear protein extracts were incubated ON with V5-Tag magnetic beads (M16711; MBL International Corporation;

Woburn, MA, USA), or with the indicated primary antibodies [BCL6 (sc-858) and HDAC3 (sc-11417) from Santa Cruz Biotechnology (Dallas, TX, USA); NCOR2 (06-891) from Sigma Aldrich; BACH2 (ARP39513_P050) from Aviva Systems Biology (San Diego, CA, USA); Rabbit anti-mouse control IgG (ab46540) from Abcam], followed by a 2h incubation with Protein A Dynabeads (10001D; ThermoFisher Scientific). Whole cell lysates or IP products were resolved by SDS-PAGE, transferred to PVDF membrane (1620177; Bio-Rad Laboratories; Hercules, CA, USA), and probed with the indicated primary antibodies [BCL6 (sc-7388), HDAC3 (sc-376957) and β-ACTIN (sc-47778) from Santa Cruz Biotechnology; NCOR2 (PA1-843) from ThermoFisher Scientific; BACH2 (ARP39513_P050); TBL1XR1 (H00079710-M01) from Abnova (Taipei City, Taiwan); BirA (BID-CP-100) from BioFront Technologies (Tallahassee, FL, USA)]. Membranes were then incubated with a corresponding peroxidase-conjugated secondary antibody (Jackson Immunoresearch). Protein signals were detected using enhanced chemiluminescence (RPN2232; GE Healthcare Life Sciences).

Rapid immunoprecipitation mass spectrometry of endogenous proteins

RIME experiments (Mohammed et al., 2016) in OCI-Ly1 cells were performed by Active Motif, using an anti-BCL6 antibody (sc-858), or an isotype-matched IgG control (ab46540). Biological duplicates were prepared for each immunoprecipitation. Known common contaminants (CRAPome Database v1.1 for Jurkart cells) were removed from the final protein list.

RNA and genomic DNA and extraction

Genomic DNA was extracted using: a) the QuickExtract DNA Extraction Solution (QE09050; Epicenter; Madison, WI, USA), for human cell lines; b) the Puregene Gentra cell kit (158388; QIAGEN), for mouse cell suspensions; c) the DirectPCR Lysis Reagent (101-T; Viagen Biotech; Los Angeles, CA, USA), for mouse tails. Total RNA was extracted from cell suspensions using Trizol LS (10296010; ThermoFisher Scientific) and RNeasy Mini Kit (74106; QIAGEN), with DNase treatment. RNA concentration was determined using Qubit Fluorometric Quantification (ThermoFisher Scientific) and integrity was verified using Agilent 2100 Bioanalyzer (Agilent Technologies).

Genotyping PCR

PCR-based genotyping of the *Tbl1xr1*-D370Y allele was done on genomic DNA extracted from mouse tail tissues, using the GoTaq® DNA Polymerase (M3001; Promega Corporation). Primers were designed to flank the distal LoxP site located between *Tbl1xr1* exons 10 and 11, in the targeted allele (Figures S1A and S1B) (Forward: 5′-AAC GAG AAG CCA AGG TTC CAG TTC-3′; Reverse: 5′-GAT GCA AAG GTG TTG TTG CTC TGC-3′). PCR program: [2′: 95C] x1, [30’’: 95C, 30’’: @55C, 45’’: 72C] x35, [5′: 72C] x1. PCR-based validation of exon 5 excision in *Tbl1xr1*$^{KO/KO}$ mice was done on genomic DNA from sorted GCB. Primers were designed to target *Tbl1xr1* exon 5 (Figure S1G) (Forward: 5′-TAT CCT CAG CGG TGG GTT AC-3′; Reverse: 5′-GCC AGT AGG GGT TGC TGA TA-3′). PCR program: [2′: 95C] x1, [1’: 95C, 1’: @52C, 2′: 72C] x35, [5′: 72C] x1. PCR products were resolved by agarose gel electrophoresis, and visualized using SYBR Safe DNA stain (S33102; ThermoFisher Scientific).

Quantitative real-time PCR

cDNA synthesis from total RNA extracts was performed using the Verso cDNA Synthesis kit (AB1453B; ThermoFisher Scientific). Expression of the genes of interest was detected using the Fast SYBR Green Master Mix (4385614; ThermoFisher Scientific) on a QuantStudio6 Flex Real-Time PCR System (ThermoFisher Scientific). Gene expression was normalized to Actin or GAPDH levels, using the ΔΔC(t) method, and results were represented as mRNA expression. See Table S6 for primer sequences.

Sanger sequencing

cDNA from FACS-sorted *Tbl1xr1*$^{WT/WT}$ or *Tbl1xr1*$^{D370Y/WT}$ GCB, or from the indicated cells, was generated as described above. Sanger sequencing was performed by GENEWIZ (South Plainfield, NJ, USA).

Assessment of Pim1 somatic mutations

Pim1 locus was amplified from genomic DNA using the primers from Liu et al. (2008): Fwd: 5′-TTC GGC TCG GTC TAC TCT G-3′; Rev: 5′-GGA GGG AAA AGT GGG TCA TAC-3′. PCR program: [2′: 95C] x1, [1’: 95C, 1’: @65C, 1’: 72C] x25, [15’: 72C] x1. PCR products were resolved by agarose gel electrophoresis, and extracted using the QIAquick Gel Extraction Kit (28704; QIAGEN). Purified products were then cloned using the TOPO TA cloning kit for sequencing (K457501; ThermoFisher Scientific), following manufacturer instructions. Plates were grown ON at 37C, and bacteria colony sequencing was performed by GENEWIZ, using the T7 universal sequencing primer (5′-TAA TAC GAC TCA CTA TAG GG-3′). Only good-quality sequence was considered, as determined by inspection of the chromatograms. Mutation mismatch counts were calculated from Sanger sequencing using the sangerseqR (Hill et al., 2014) and Biostrings (R package version 2.54.0) packages. As a negative control for SHM, genomic DNA extracted from sorted *Aicda*$^{KO/KO}$ GCB was used as PCR template.

J_H4 intron sequencing

Sorted GCB or tumor cells were collected by centrifugation and resuspended in 500μL DNA cell lysis buffer (100mM Tris pH 8.8, 200mM NaCl, 5mM EDTA, 0.2% SDS) containing 0.2mg/mL proteinase K and incubated at 56°C overnight. 500μL isopropanol and 40μg glycogen was added to precipitate DNA. The mixture was incubated at 4°C for 20 minutes followed by centrifugation

for 20 minutes at 20,000 x g and 4°C. The pellet was washed with 1mL 70% ethanol and centrifuged for 10 minutes at 20,000xg and 4°C. The pellet was resuspended with 20μL DEPC-H2O and incubated at 37°C for 40 minutes. JH4 intron sequences were amplified from germinal center B cell genomic DNA by PCR using J_H4 forward primer (5′-GGA ATT CGC CTG ACA TCT GAG GAC TCT GC-3′), JH4 reverse primer (5′-GAC TAG TCC TCT CCA GTT TCG GCT GAA TCC-3′) (Jolly et al., 1997), and Phusion High-Fidelity DNA Polymerase (M0530L: New England BioLabs). PCR program: [3′: 98C] x1, [30”: 98C, 1’: 72C] x39, [10’: 72C] x1. PCR products were resolved by agarose gel electrophoresis, and the 1.2kb band extracted using the QIAquick Gel Extraction Kit. The amplicon was ligated into the pCR-Blunt II-TOPO vector and transformed into One Shot TOP10 chemically competent *E. coli* (K280002; ThermoFisher Scientific) according to the manufacturer's protocol. Clones were sequenced using the bacterial colony Sanger sequencing service provided by Eton Bioscience (Union, NJ, USA) and JH4 sequencing primer (5′-CCA TAC ACA TAC TTC TGT GTT CC-3′). As a negative control for SHM, genomic DNA extracted from sorted *Acida*$^{KO/KO}$ GCB was used as PCR template. Sequences were aligned using MUSCLE (EMBL-EBI) included in Biopython package (Cock et al., 2009) and analyzed for mutations using Python 3 script.

RNA sequencing and analysis

Library preparation, sequencing and post-processing of the raw data was performed at the Epigenomics Core at Weill Cornell Medicine. Samples that passed the quality control (RNA Integrity Number $\geq$ 8) were subjected to library preparation using the Illumina TruSeq stranded-mRNA sample kits (Illumina; San Diego, CA, USA), according to the manufacturer. Briefly, poly A+ RNA was purified from 100 ng of total RNA with oligo-dT beads. Purified mRNA was fragmented with divalent cations at elevated temperature, to ~200 bp. Following dscDNA synthesis, the double stranded products are end repaired, followed by addition of a single 'A' base and then ligation of the Illumina TruSeq adaptors. The resulting product was amplified with 15 cycles of PCR. Libraries were validated using the Agilent Technologies 2100 Bioanalyzer and Quant-iT dsDNA HS Assay (Q33120; ThermoFisher Scientific). Each library was made with a unique Index sequence and libraries were pooled for sequencing. The pool was clustered at 6.5pM on a single end read flow cell and sequenced for 50 cycles on an Illumina HiSeq 2500 to obtain ~50 M reads per sample. Single-end sequencing (SE50), for the *Tbl1xr1*$^{D370Y/WT}$ GCB profiling, or paired end-sequencing (PE50x2) for the *IμBcl6-Tbl1xr1*$^{D370Y/WT}$ and *Tbl1xr1*$^{KO/KO}$ GCB profiling, were performed on an Illumina HiSeq2500 sequencer. Primary processing of sequencing images was done using Illumina's Real Time Analysis software (RTA) as suggested by Illumina. CASAVA 1.8.2 software was used to perform image capture, base calling, demultiplexing samples and generation of raw reads and respective quality scores. Sequencing results were aligned to mm10 using STAR (Dobin et al., 2013) and annotated to RefSeq using the R subread package (Liao et al., 2014). Differentially expressed genes were identified using the EdgeR package GLM (Robinson et al., 2010) with thresholds of fold-change > 1.5 and $p < 0.05$, adjusted for multiple testing using Benjamini-Hochberg correction. Hierarchical clustering was performed using Euclidean distance of log FPKM values of genes within the top 5th percentile of standard deviation across replicates and Ward's minimum variance. Gene set enrichment analysis was performed using the GSEA algorithm, as described in (Subramanian et al., 2005). Pathway analysis was performed using PAGE algorithm (Goodarzi et al., 2009).

CyTOF immunophenotyping of DLBCL specimens

Diagnostic pre-treatment LN biopsies from patients with DLBCL, or non-malignant "reactive" LN (rLN) were acquired from the lymphoma tumor bank at the BC Cancer Agency. All samples were obtained with informed consent and according to protocols approved by the BCCA Research Ethics Board, and were selected based on sufficient numbers of viable cells for CyTOF analysis (2 million per sample).

Vials of frozen cells were rapidly thawed from liquid nitrogen to 37°C using a water bath, and cell suspensions were washed with RPMI supplemented with 10% fetal bovine serum. Cells were used immediately after thawing and were incubated in cisplatin for 15 minutes to label dead cells, then washed thoroughly in PBS+2%FCS. Cell pellets were then incubated with Fc Receptor Blocking Solution (422302; BioLegends) for 10 minutes to inhibit non-specific binding of antibodies, before the addition of a master mix of metal-conjugated antibodies at optimal concentrations for 30 minutes. The relevant antibodies used for the current analysis are; CD10-156Nd (HI10a; Fluidigm, South San Francisco, CA, USA), CD27-167Er (L128; Fluidigm), CD38-172Yb (HIT2; Fluidigm) and CD44-171Yb (IM7; Fluidigm).

Samples were bar-coded with the Cell-ID 20-plex Pd kit (#201060; Fluidigm) as per manufacturer's instructions before being pooled together for analysis to ensure consistent acquisition. Batch effects were accounted for using a spike-in staining control of rLN cells. Pooled suspensions were then spiked with DVS normalization beads to account for technical drift during acquisition, and acquired on a Fluidigm CyTOF 2 instrument. After acquisition, samples were normalized based on bead signal intensity and de-multiplexed to distinguish individual samples using published tools (https://github.com/nolanlab/bead-normalization, https://github.com/nolanlab/single-cell-debarcoder).

Viable cells were gated in FlowJo based on negative staining for cisplatin, and all subsequent analysis was performed using R. Malignant tumor cells were identified as previously described (Nissen et al., 2019). Isolated malignant cells and manually-defined germinal center B cells and memory B cells were then pooled together for principal component analysis.

Exome sequencing on samples (Table S6) was carried out using genomic DNA extracted from DLBCL samples using QIAGEN reagents. Exome libraries were created using IDT exome capture kits, and samples were sequenced using an Illumina HiSeq 2500 (PE_2x125). Somatic SNV/indel variants were identified using the intersection of calls predicted by VarScan (version 2.3.6) (Koboldt et al., 2012), Strelka (version 1.0.13) (Saunders et al., 2012) and MuTect (version 1.1.4) (Cibulskis et al., 2013). All variants were

annotated using SnpEff (version 4.2) (Cingolani et al., 2012) and filtered for effects predicted to have an impact at the protein level (nonsynonymous, stop-gained, splice site, UTR). Variants were further filtered to remove potential germline SNPs if the variant: (i) had a GMAF score > 1% or (ii) was present in dbSNP (version 137) (Sherry et al., 2001) and not COSMIC (version 68) (Tate et al., 2019). All tumors were paired against a pooled control that was constructed from 10 normal samples, to account for sequencing noise.

Graphical abstract

Cartoons used in the graphical abstract were adapted from images in the SERVIER MEDICAL ART repository (https://smart.servier.com/). Use of these images falls within the terms of the Creative Commons Attribution 3.0 Unported License (https://creativecommons.org/licenses/by/3.0/).

QUANTIFICATION AND STATISTICAL ANALYSIS

Statistical parameters including the exact value and definition of n, precision measures (mean ± SEM or SD), and statistical significance are reported in the Figures and Figure Legends. Statistical analysis was conducted using GraphPad Prism 6.00 (GraphPad Software, San Diego, CA, USA), or R statistical language scripts and packages specified under Method Details. Data was judged to be statistically significant when $p < 0.05$. Asterisks in figures denote statistical significance (*, $p < 0.05$; **, $p < 0.01$; ***, $p < 0.001$). Statistical analysis of Sequencing data is described under Method Details section and in Figure Legends.

Supplemental Figures

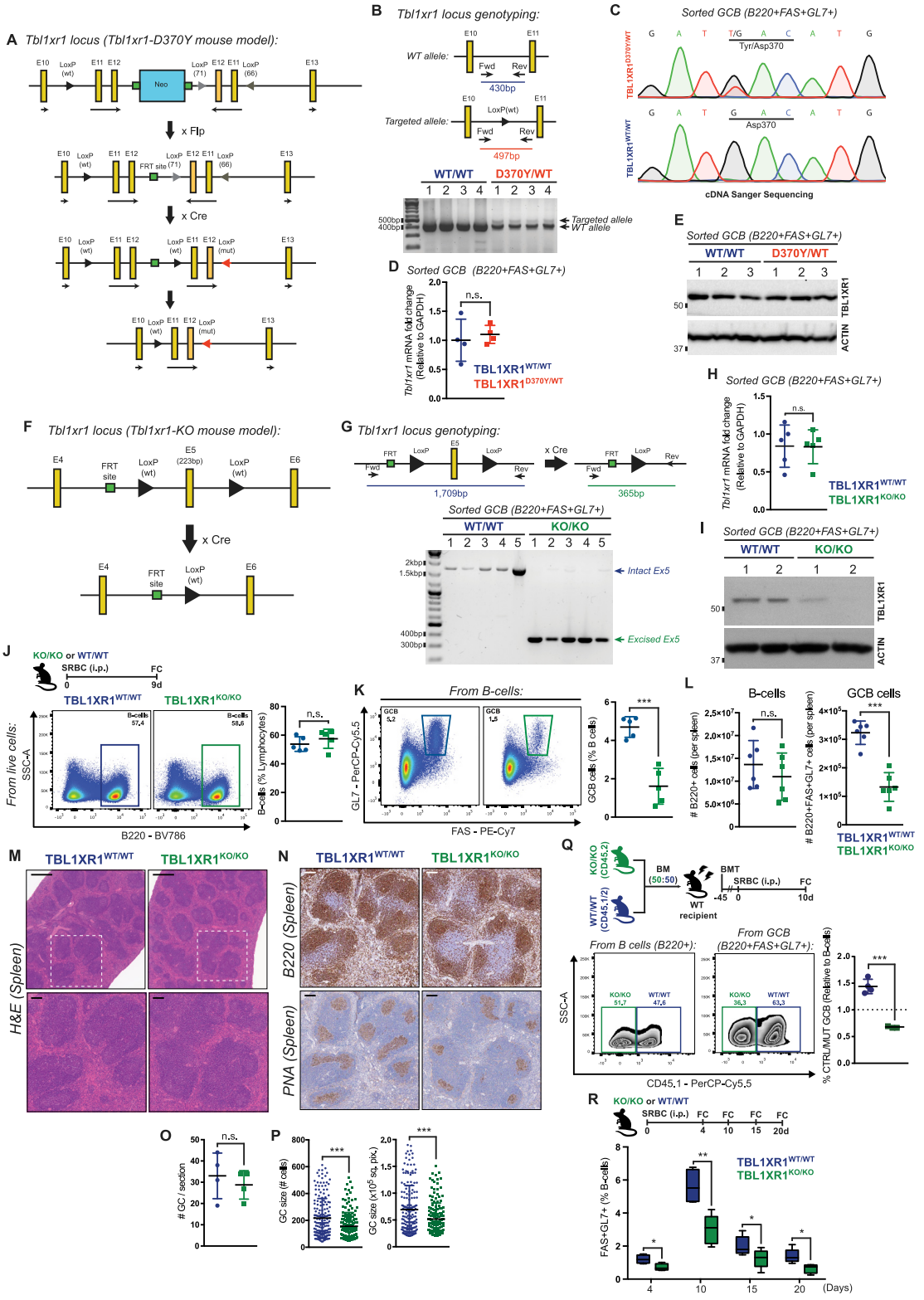

(legend on next page)

Figure S1. *Tbl1xr1*-D370Y and *Tbl1xr1*-KO Mouse Models, Related to Figure 1

A, Schematic depiction of the targeted allele in the *Tbl1xr1*-D370Y mouse model, and the effects of Cre-induced recombination. "E" = Exon; "Neo" = Neomycin resistance cassette. Thin black arrows depict exon orientation.

B, (Top) Scheme depicting the PCR-based strategy used for genotyping the targeted allele in the *Tbl1xr1*-D370Y mouse model. Black arrows represent primers. (Bottom) Representative PCR-based genotyping results on genomic DNA extracted from tail tissue from *Tbl1xr1*$^{WT/WT}$ or *Tbl1xr1*$^{D370Y/WT}$ animals. Numbers designate different animals.

C, Sanger sequencing analysis of *Tbl1xr1* cDNA in sorted splenic GCB from *Tbl1xr1*$^{D370Y/WT}$ or *Tbl1xr1*$^{WT/WT}$ mice, 8 days after SRBC immunization. Data shown for one animal per genotype, representative of a total of three.

D, Quantitative Real Time-PCR analysis of *Tbl1xr1* mRNA expression levels in *Tbl1xr1*$^{D370Y/WT}$ and *Tbl1xr1*$^{WT/WT}$ sorted GCB, 8 days after SRBC immunization. Primers were designed to target *Tbl1xr1* exons 11-13. Results are expressed as fold change, relative to *Tbl1xr1*$^{WT/WT}$, and normalized to GAPDH expression levels.

E, WB analysis of TBL1XR1 expression levels in sorted GCB from three representative *Tbl1xr1*$^{D370Y/WT}$ and *Tbl1xr1*$^{WT/WT}$ animals, obtained as in (C). ACTIN protein expression levels were used as a loading control.

F, Schematic depiction of the targeted allele in the *Tbl1xr1*-KO mouse model, and the effects of Cre-induced recombination.

(G), (Top) Scheme depicting the PCR-based strategy used for verifying Cre-induced *Tbl1xr1* exon 5 excision in the *Tbl1xr1*-KO model. Thin black arrows represent primers. (Bottom) Representative PCR results on genomic DNA from sorted GCB, from *Tbl1xr1*$^{WT/WT}$ or *Tbl1xr1*$^{KO/KO}$ animals, 8 days after SRBC immunization. Numbers designate different animals.

H, Quantitative Real Time-PCR analysis of *Tbl1xr1* mRNA expression levels in GCB obtained as in (G). Primers were designed to target *Tbl1xr1* exons 11-13. Results are expressed as fold change, relative to *Tbl1xr1*$^{WT/WT}$ GCB, and normalized to GAPDH expression levels.

I, WB analysis of TBL1XR1 expression levels in sorted GCB from two representative *Tbl1xr1*$^{KO/KO}$ and *Tbl1xr1*$^{WT/WT}$ animals, obtained as in (G). ACTIN protein expression levels were used as a loading control.

J-K, Representative FC plots (left) and quantification (right) of (J) total splenic B cells or (K) GCB in Cγ1Cre-*Tbl1xr1*$^{KO/KO}$ (*Tbl1xr1*$^{KO/KO}$) or *Tbl1xr1*$^{WT/WT}$ mice. See also Data S1N.

L, Absolute FC-based quantification of (left) total splenic B cells or (right) GCB from *Tbl1xr1*$^{KO/KO}$ or *Tbl1xr1*$^{WT/WT}$ mice, 9 days after SRBC immunization.

M, Representative H&E images of splenic sections taken from animals treated as in (J). Insets (bottom) show zoom of outlined areas. Scale bars = 500μm (top) or 100μm (bottom).

N, Representative images of (top) B220 or (bottom) PNA IHC staining in consecutive splenic sections from specimens in (M). Scale bars = 100μm.

O-P, Graphs show quantification of (O) the number of GC per spleen section, or (P) GC size as number of cells (left) or surface area (right), based on PNA staining. Dots in (A) represent different animals. Dots in (P) represent individual GC. Shown are pooled results for 4 animals per genotype.

(Q), Representative FC plots (left) and quantification (right) of the relative contribution of *Tbl1xr1*$^{KO/KO}$ and *Tbl1xr1*$^{WT/WT}$ cells to the total B cell and GCB compartments, based on CD45 allelic frequencies.

R, FC analysis of splenic GCB frequency. Left to right: n = 3, 4, 5, 5 (*Tbl1xr1*$^{WT/WT}$) or 3, 4, 5, 5 mice (*Tbl1xr1*$^{KO/KO}$).

Values represent mean ± SEM. All data were reproducible with at least two repeats. NS, not significant; *$p < 0.05$; **$p < 0.01$; ***$p < 0.001$, using unpaired (D,H,J-L,R) or paired (Q) two-tailed Student's t test, or Mann-Whitney U-test (O-P).

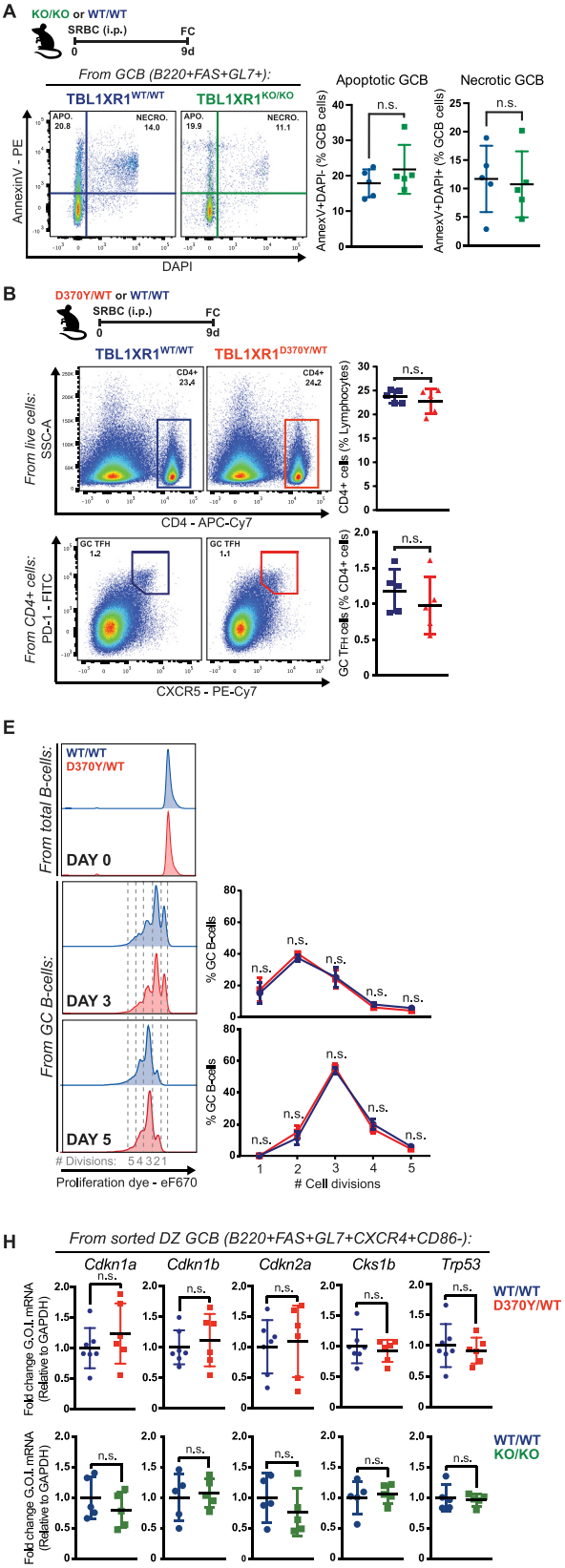

(legend on next page)

Figure S2. *Tbl1xr1*-D370Y and *Tbl1xr1*-KO GCB Proliferation and Cell Death, Related to Figure 2

A, Representative FC plots (left) and quantification (right) of AnnexinV/DAPI staining in splenic GCB.

B, Representative FC plots and quantification of (top) total $CD4^+$ or (bottom) GC T follicular helper ($CD4^+CXCR5^{hi}PD\text{-}1^{hi}$) splenic populations.

C, Experimental scheme for experiment in D-E.

D, Representative FC plots of (left) GCB formation and (right) the relative contribution of *Tbl1xr1*$^{D370Y/WT}$ and *Tbl1xr1*$^{WT/WT}$ cells to this population, at the indicated time-points.

E, Representative FC plots (left) and quantification (right) of GCB proliferation, based on progressive dilution of a cell proliferation dye. Results are expressed as the frequency of GCB that have undergone a certain number of cell divisions, for three biological replicates, with 3 technical replicates each. Representative plots of stain intensity at Day 0 are included, as a control for initial dye loading levels.

F, Representative FC plots (left) and quantification (right) of EdU incorporation by GCB.

G, FC analysis of cell cycle distribution of splenic GCB for animals in (F), based on EdU/DAPI staining.

H, RT-qPCR-based quantification of cell cycle checkpoint genes performed on DZ GCB sorted 9 days after SRBC immunization. Results are expressed as fold change of gene-of-interest (G.O.I.), relative to the corresponding *Tbl1xr1*$^{WT/WT}$ controls, and normalized to GAPDH expression levels

Values represent mean ± SEM. All the data were reproducible with at least two repeats. NS, not significant; *$p < 0.05$; **$p < 0.01$; ***$p < 0.001$, using unpaired (A,B,H) or paired (F-G) two-tailed Student's t test, or two-way ANOVA (E).

CellPress

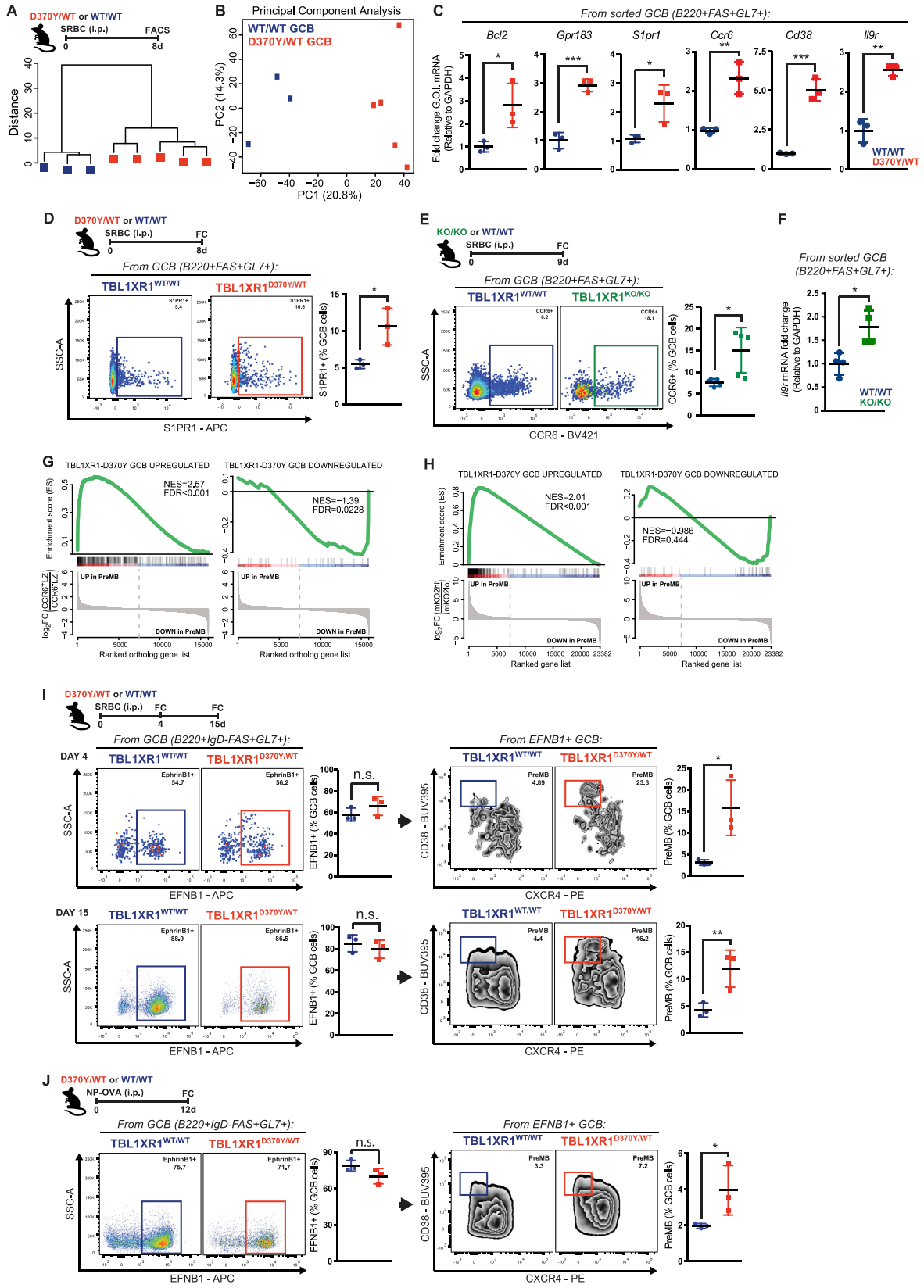

(legend on next page)

Figure S3. PreMB Population in *Tbl1xr1*-D370Y Mice, Related to Figure 3

A, Hierarchical clustering dendrogram, based on Euclidean distance, using log FPKM values of variable genes (top 5th percentile) and Ward's method, for experiment in Figure 3A. Squares represent individual animals

B, PCA plot for *Tbl1xr1*$^{D370Y/WT}$ and *Tbl1xr1*$^{WT/WT}$ GCB RNA-Seq samples from Figure 3A.

C, Quantitative Real Time-PCR (RT-qPCR) validation of selected differentially expressed genes from Figure 3A, performed on an independent set of GCB, sorted 8 days after SRBC immunization. Results are expressed as fold change of gene-of-interest (G.O.I.), relative to *Tbl1xr1*$^{WT/WT}$, and normalized to GAPDH expression levels.

D, Representative FC plots (left) and quantification (right) of S1PR1^{+} splenic GCB.

E, Representative FC plots (left) and quantification (right) of CCR6^{+} splenic GCB.

F, RT-qPCR analysis of *Il9r* mRNA expression levels in *Tbl1xr1*$^{KO/KO}$ and *Tbl1xr1*$^{WT/WT}$ sorted GCB, 8 days after SRBC immunization. Results are expressed as fold change, relative to *Tbl1xr1*$^{WT/WT}$, and normalized to GAPDH expression levels.

G-H, GSEA of gene signatures (left) upregulated or (right) downregulated in *Tbl1xr1*$^{D370Y/WT}$ versus *Tbl1xr1*$^{WT/WT}$ GCB, ranked against: (G) the preMB (CCR6^{+}LZ) GCB signature from (Suan et al., 2017); (H) an alternative PreMB (mKO2^{hi}) GCB signature from GSE85018.

I, FC analysis of (left) EFNB1^{+} or (right) preMB populations in splenic GCB, at (top) 4 days or (bottom) 15 days post SRBC immunization.

J, FC analysis of (left) EFNB1^{+} or (right) preMB populations in splenic GCB from mice immunized with an hapten conjugate.

Values represent mean ± SEM. All data were reproducible with at least two repeats. NS, not significant; *$p < 0.05$; **$p < 0.01$; ***$p < 0.001$, using unpaired two-tailed Student's t test (C)-(F),(I)-(K).

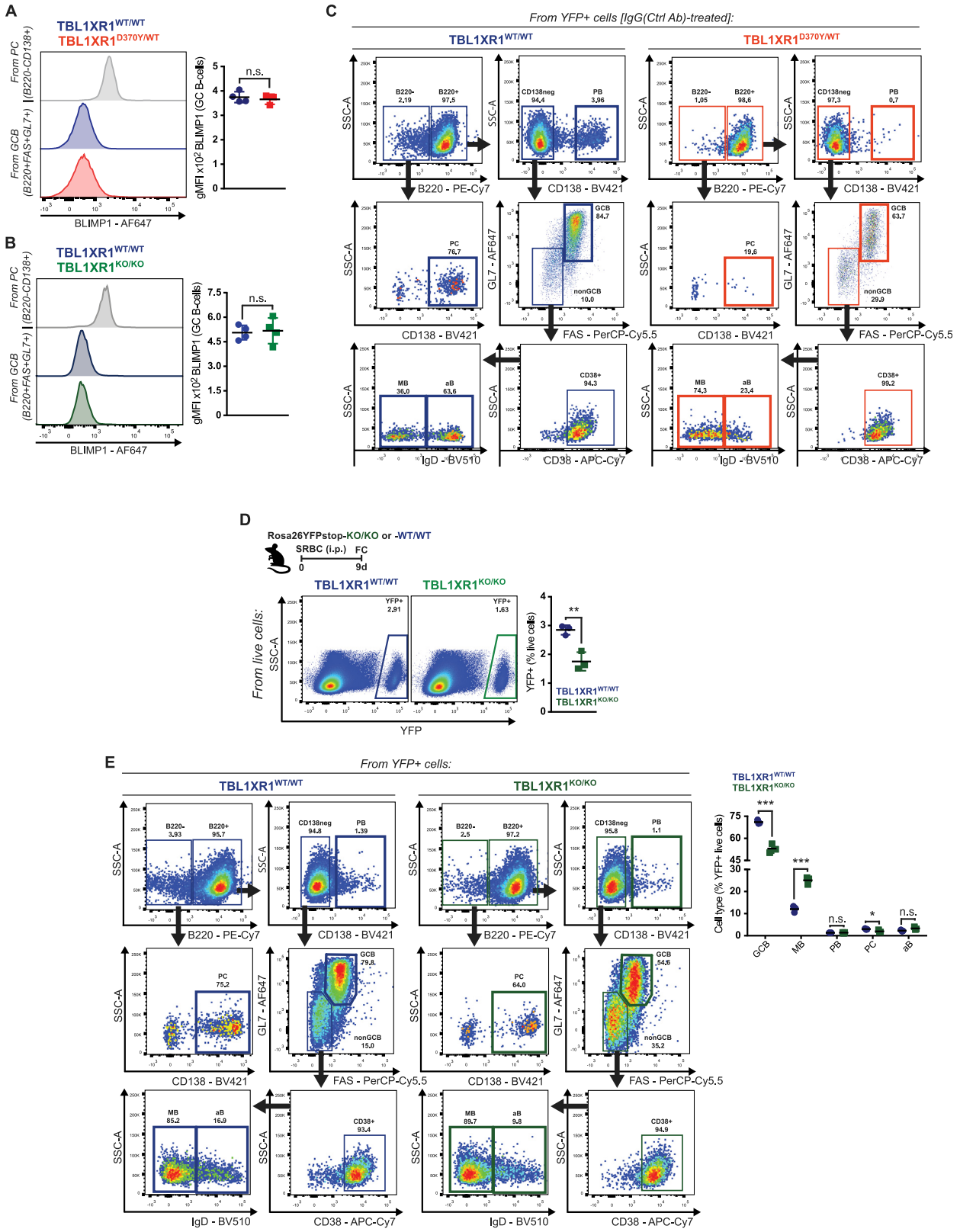

(legend on next page)

Figure S4. Cell Fate Bias in *Tbl1xr1*-D370Y and *Tbl1xr1*-KO Mice, Related to Figure 4

A-B, Representative histograms (left) and quantification (right) of BLIMP1 expression levels, based on FC data, in (A) splenic GCB from *Tbl1xr1*$^{WT/WT}$ or *Tbl1xr1*$^{D370Y/WT}$ mice, 10 days after SRBC immunization, or (B) splenic GCB from *Tbl1xr1*$^{WT/WT}$ or *Tbl1xr1*$^{KO/KO}$ mice, 9 days after SRBC immunization. BLIMP1 expression in PC from a representative *Tbl1xr1*$^{WT/WT}$ animal is included on each histogram plot, as a positive control.

C, Representative FC plots for YFP^{+} cells in IgG1(Ctrl Ab)-treated animals in Figure 4E.

D-E, Representative FC plots and quantification of (D) total YFP^{+} splenocytes and (E) the relative cell type composition of this population. aB = Activated B cells. Values represent mean ± SEM. All data were reproducible with at least two repeats. NS, not significant; *$p < 0.05$; **$p < 0.01$; ***$p < 0.001$, using unpaired two-tailed Student's t test.

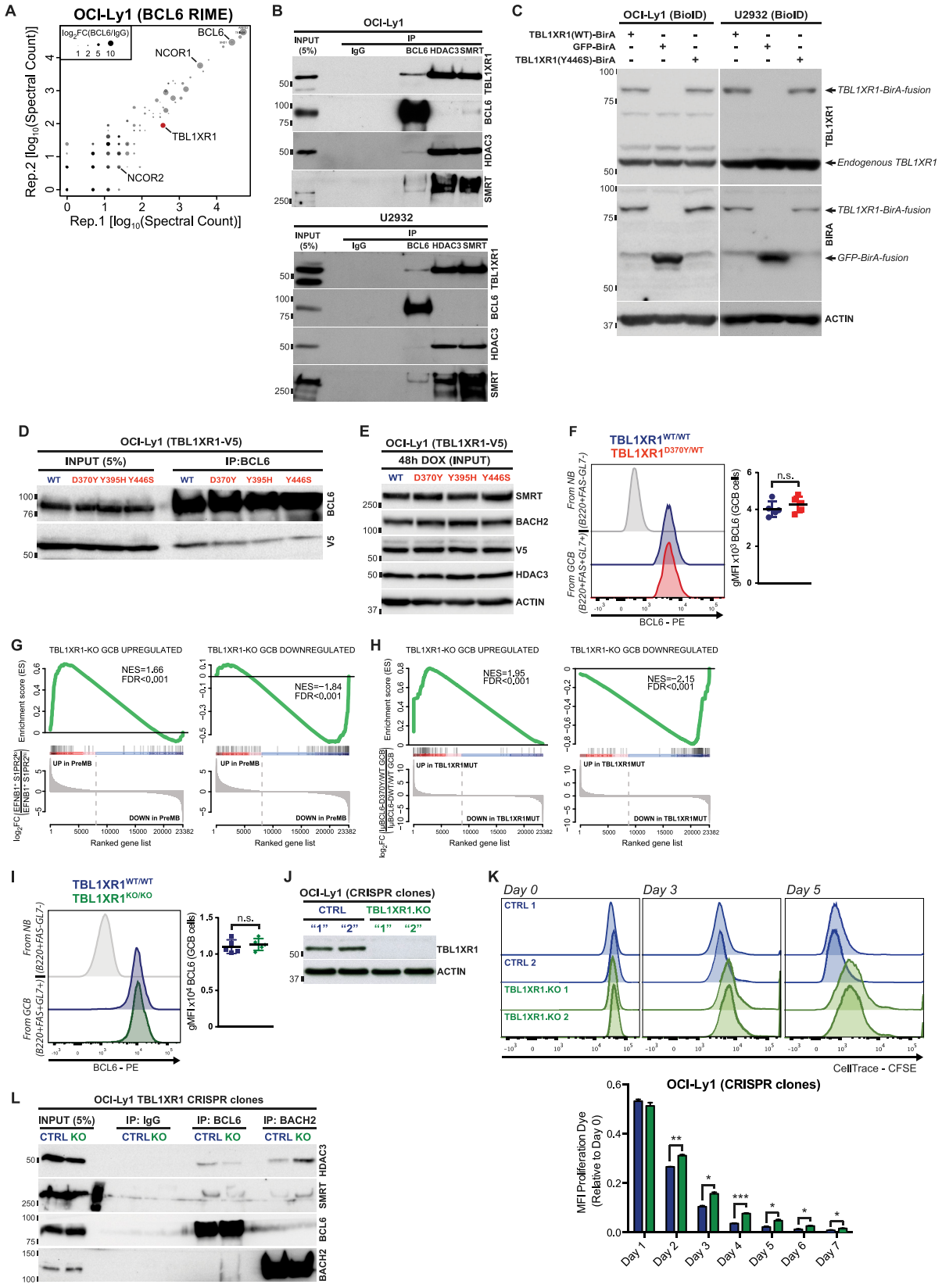

(legend on next page)

Figure S5. TF Switch Triggered by *TBL1XR1 M*utation or Loss, Related to Figure 5

A, RIME analysis of BCL6 interacting partners in OCI-Ly1 cells. A species-matched IgG antibody was used as negative control. Shown is the correlation for two biological replicates for BCL6 immunoprecipitations. Circle sizes are proportional to the fold induction over the IgG control.

B, Co-IP of endogenous TBL1XR1 with BCL6, HDAC3 or SMRT in nuclear extracts obtained from the stated cell lines. A species-matched IgG antibody was included as negative control.

C, WB results showing expression of TBL1XR1 and BirA, in cell lines used for BioID experiments, 48h after Doxycycline induction. ACTIN expression levels were used as a loading control.

D, Co-IP of endogenous BCL6 with TBL1XR1-V5 (WT, D370Y, Y395H, Y446S), in OCI-Ly1 engineered cells from Figure 5D. BCL6 immunoprecipitation was conducted on nuclear extracts obtained 48h after Doxycycline induction.

E, WB results showing expression of the stated proteins in nuclear protein extracts from cells transduced to inducibly express WT or mutant (D370Y, Y395H, Y446S) TBL1XR1-V5 fusion proteins. Results shown correspond to extracts obtained 48h after Doxycycline induction. ACTIN expression levels were used as a loading control.

F, Representative histograms (left) and quantification (right) of BCL6 expression levels, based on FC data, in splenic GCB from *Tbl1xr1*$^{WT/WT}$ or *Tbl1xr1*$^{D370Y/WT}$ mice, 8 days after SRBC immunization. BCL6 expression in NB from a representative Tbl1x1$^{WT/WT}$ animal is included on the histogram plot, as a negative control.

G-H, GSEA of gene signatures upregulated and downregulated in *Tbl1x1*$^{KO/KO}$ versus *Tbl1xr1*$^{WT/WT}$ GCB, ranked against: (G) the preMB (EFNB1^{+}S1PR2^{lo}) GCB signature from GSE89897 or (H) the *IμBcl6-Tbl1xr1*$^{D370Y/WT}$ GCB signature from Figure 5H.

I, Representative histograms (left) and quantification (right) of BCL6 expression levels, based on FC data, in splenic GCB from *Tbl1xr1*$^{WT/WT}$ or *Tbl1xr1*$^{KO/KO}$ mice, 8 days after SRBC immunization. BCL6 expression in NB from a representative Tbl1x1$^{WT/WT}$ animal is included on the histogram plot, as a negative control.

J, WB analysis of TBL1XR1 protein expression in representative single-cell-derived CRISPR.KO or Control clones, obtained with 2 different anti-*TBL1XR1* guide RNAs ("1" or "2").

K, Flow cytometry analysis of cell proliferation by progressive dilution of CellTrace Dye, in CRISPR.KO or Control clones in (J). Shown are representative histograms (left) and quantification (right). Bar plot presents data as proliferation dye MFI, relative to that on Day 0. Results for two clones per genotype were averaged, considering five technical replicates for each.

L, Co-IP of endogenous SMRT and HDAC3, by BACH2 or BCL6 immunoprecipitation, in nuclear extracts obtained from the stated cell lines. A species-matched IgG antibody was included as negative control.

Values represent mean ± SEM. All data were reproducible with at least two repeats. NS, not significant; *$p < 0.05$; **$p < 0.01$; ***$p < 0.001$, using unpaired two-tailed Student's t test (F,I); or two-way (K) ANOVA with Tukey's post-test.

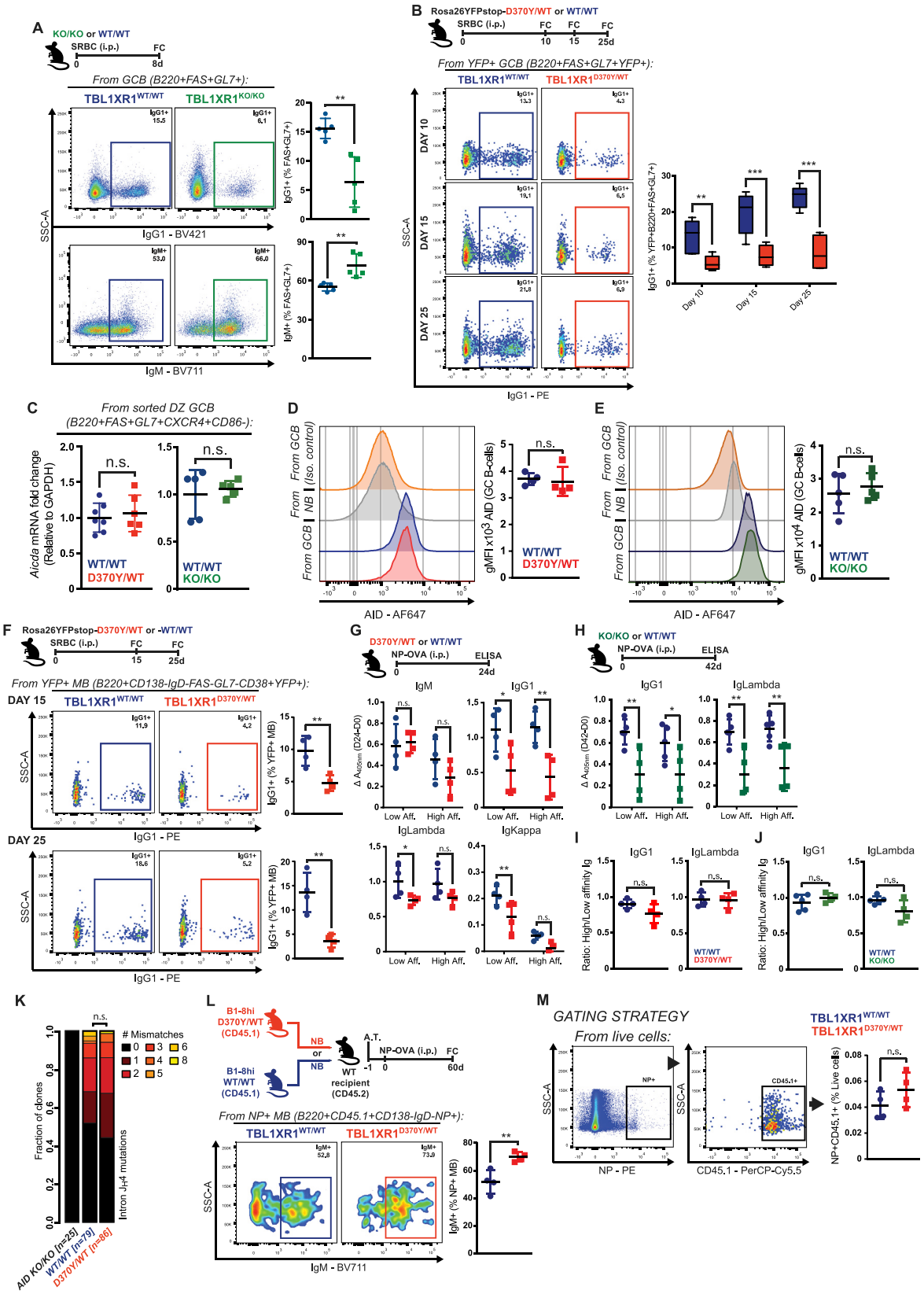

(legend on next page)

Figure S6. AID Function in *Tbl1xr1*-D370Y and *Tbl1xr1*-KO B-Cells, Related to Figure 6

A, Representative FC plots (left) and quantification (right) of (top) IgG1$^+$ or (bottom) IgM$^+$ (bottom) splenic GCB.

B, Representative FC plots and quantification of IgG1$^+$ GCB at (top) 10 days, (center) 15 days, or (bottom) 25 days post SRBC immunization.

C, RT-qPCR-based assessment of *Aicda* mRNA expression in DZ GCB, sorted 9 days after SRBC immunization. Results are expressed as fold change, relative to *Tbl1xr1*$^{WT/WT}$, and normalized to GAPDH expression levels.

D-E, Representative histograms (left) and quantification (right) of AID expression levels, based on FC data, in (D) splenic GCB (B220$^+$FAS$^+$GL7$^+$) from *Tbl1xr1*$^{WT/WT}$ or *Tbl1xr1*$^{D370Y/WT}$ mice, 8 days after SRBC immunization, or (E) GCB from *Tbl1xr1*$^{WT/WT}$ or *Tbl1xr1*$^{KO/KO}$ mice, 10 days after SRBC immunization. AID expression in NB (B220$^+$FAS$^-$GL7$^-$IgD$^+$) from a representative *Tbl1xr1*$^{WT/WT}$ animal (gray), and isotype control staining on GCB (orange) are included on each histogram plot, as a negative controls.

F, Representative FC plots (left) and quantification (right) of IgG1$^+$ MB cells at (top) 15 days or (bottom) 25 days post SRBC immunization.

G, ELISA-based assessment of NP-specific serum antibodies in *Tbl1xr1*$^{D370Y/WT}$ versus *Tbl1xr1*$^{WT/WT}$ mice, represented as the difference in signal between days 0 and 24 post immunization.

H, ELISA-based assessment of NP-specific serum antibodies in *Tbl1xr1*$^{KO/KO}$ versus *Tbl1xr1*$^{WT/WT}$ mice, represented as the difference in signal between days 0 and 42 post immunization.

I, Relative levels of affinity maturation in *Tbl1xr1*$^{D370Y/WT}$ versus *Tbl1xr1*$^{WT/WT}$ mice, represented as the ratio between high-affinity and low-affinity NP-specific serum immunoglobulin signal, determined as in (G).

J, Relative levels of affinity maturation in *Tbl1xr1*$^{KO/KO}$ versus *Tbl1xr1*$^{WT/WT}$ mice, represented as the ratio between high-affinity and low-affinity NP-specific serum immunoglobulin signal, determined as in (H).

K, Bar plot showing SHM burden at the immunoglobulin intron J_H4 loci (as in Jolly et al., 1997) in GC B cells from *Rosa26YFP;Tbl1xr1*$^{D370Y/WT}$ or *Rosa26YFP;Tbl1xr1*$^{WT/WT}$ mice, sorted 9d after SRBC immunization. Genomic DNA extracted from sorted GC B cells from an *Aicda*$^{KO/KO}$ mouse model (AID KO/KO) was used as negative control for the experiment. Shown are pooled results for 3 [D370Y/WT], 3 [WT/WT] and 1 [AID KO/KO] animals. Numbers in square brackets represent the total numbers of sequenced clones.

L, Representative FC plots (left) and quantification (right) of IgM$^+$ splenic antigen-specific donor-derived MB cells.

M, Gating strategy and quantification of total antigen-specific donor-derived cells detected in the spleens of recipient mice, 3.5d after immunization, from experiment in Figure 6F.

Values represent mean ± SEM. All the data were reproducible with at least two repeats. NS, not significant; *$p < 0.05$; **$p < 0.01$; ***$p < 0.001$, using unpaired two-tailed Student's t test, or Wilcoxon rank sum test (K).

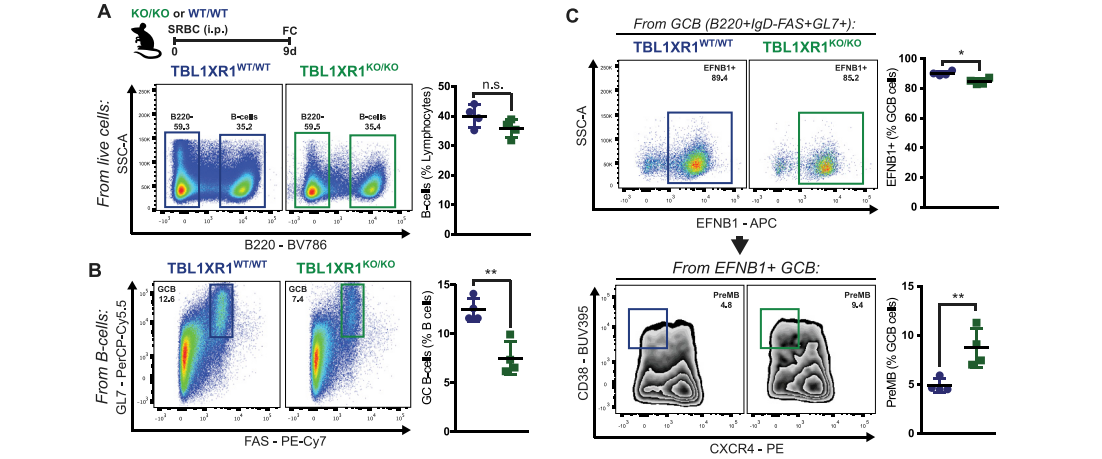

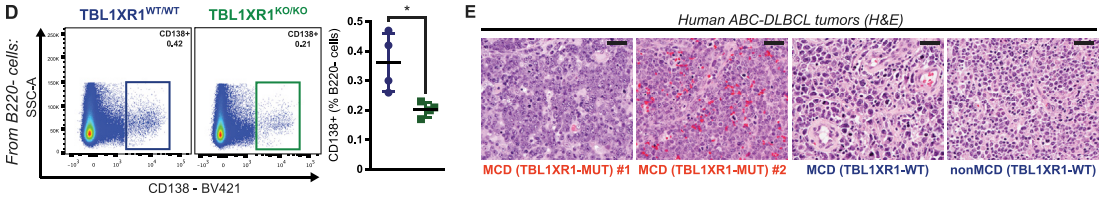

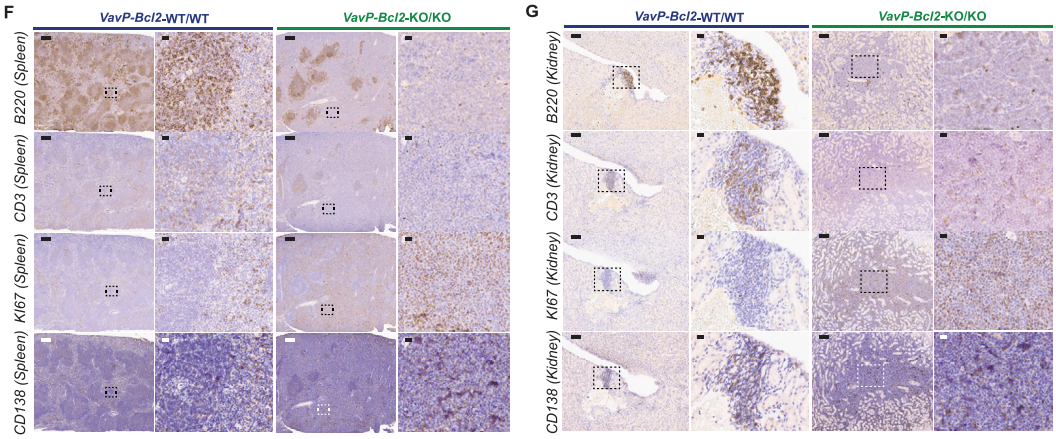

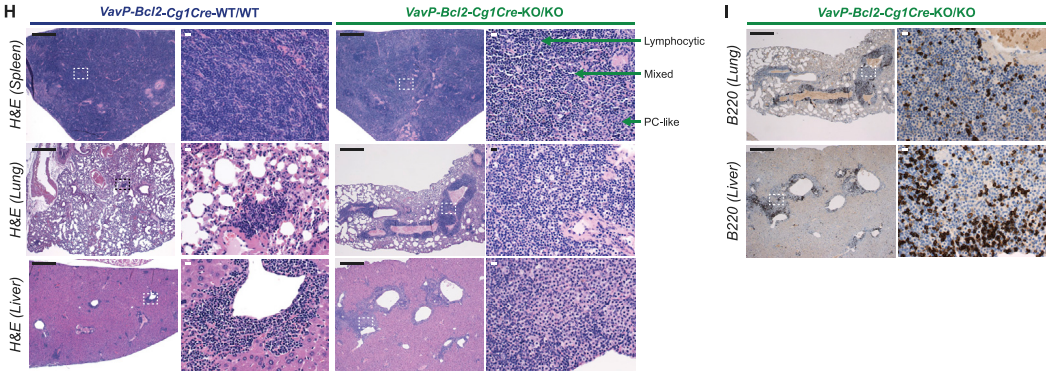

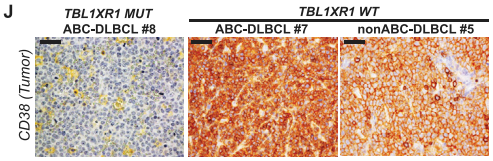

	TBL1XR1, n (%)		Chi-square
	WT	MUT	p value
CD38_HS50			
Positive	126 (42.3)	2 (13.3)	0.03
Negative	172 (57.7)	13 (86.7)	

(legend on next page)

Figure S7. Lymphomagenic Effects of *Tbl1xr1* Genetic Lesions, Related to Figure 7

A-B, Representative FC plots (left) and quantification (right) of (A) total splenic B cells or (B) GCB in *CD19Cre-Tbl1xr1*$^{KO/KO}$ (KO/KO) or *CD19Cre-Tbl1xr1*$^{WT/WT}$ (WT/WT) mice.

C, Representative FC plots and quantification of (top) EFNB1+ or (bottom) preMB populations in splenic GCB for experiment in (A).

D, Representative FC plots (left) and quantification (right) of splenic PC for experiment in (A).

(E), Representative H&E images of ABC-DLBCL tumors from 4 independent patients, from Scott & Morin cohort (Arthur et al., 2018). Scale bars = 20μm.

F-G, Representative images of B220, CD3, CD138 and KI67 IHC staining in (F) spleen or (G) kidney sections from animals in Figure 7A. Scale bars = 500μm (left) or 15μm (insets).

H-I, *VavP-Bcl2;Cγ1Cre;Tbl1xr1*$^{KO/KO}$ and *VavP-Bcl2;Cγ1Cre;Tbl1xr1*$^{WT/WT}$ mice [n = 10 per genotype] received monthly SRBC immunizations, to induce GC formation, from 2 m of age until time of sacrifice. Mice were euthanized at 11 m of age, and soft organs were collected for pathology studies. (H) Representative H&E images of spleen, lung and liver sections. (I) Representative images of B220 IHC staining in consecutive sections from specimens in (H). Insets (right) show zoom of outlined areas. Scale bars = 500μm (left) or 20μm (insets).

J, Representative images (left) and relative quantification (right) of CD38 IHC staining for *TBL1XR1* mutant or WT DLBCL human specimens, from the Scott & Morin cohort (Arthur et al., 2018). Scale bars = 20μm.

Values represent mean ± SEM. All the data were reproducible with at least two repeats. NS, not significant; *$p < 0.05$; **$p < 0.01$; ***$p < 0.001$, using unpaired two-tailed Student's t test.